SCISPACE
formerly Typeset

Open access • Posted Content • DOI:10.1101/2021.01.14.426579

High-throughput phenotypic screen for genetic modifiers in patient-derived OPA1 mutant fibroblasts identifies PGS1 as a functional suppressor of mitochondrial fragmentation — Source link

E. Cretin, P. Thomas, Elodie Vimont, Takashi Tatsuta ...+6 more authors

Institutions: Pasteur Institute, Max Planck Society, University of Cologne, University of Angers ...+1 more institutions

Published on: 15 Jan 2021 - bioRxiv (Cold Spring Harbor Laboratory)

Topics: mitochondrial fusion, Mitochondrial fission, Optic Atrophy 1, Mitochondrial disease and DNM1L

Related papers:

- OPA1-Exon4b Binds to mtDNA D-Loop for Transcriptional and Metabolic Modulation, Independent of Mitochondrial Fusion.
- Deciphering OPA1 mutations pathogenicity by combined analysis of human, mouse and yeast cell models
- Techniques for investigating mitochondrial gene expression.
- Mitochondrial Genes and their Expression in Higher Plants
- A yeast-based screening assay identifies repurposed drugs that suppress mitochondrial fusion and mtDNA maintenance defects

Share this paper:

View more about this paper here: https://typeset.io/papers/high-throughput-phenotypic-screen-for-genetic-modifiers-in-881i27vjke

bioRxiv preprint doi: https://doi.org/10.1101/2021.01.14.426579; this version posted January 15, 2021. The copyright holder for this preprint (which was not certified by peer review) is the author/funder. All rights reserved. No reuse allowed without permission.

High-throughput phenotypic screen for genetic modifiers in patient-derived *OPA1* mutant fibroblasts identifies *PGS1* as a functional suppressor of mitochondrial fragmentation

Emma CRETIN[1,2] Priscilla LOPES[1], Elodie VIMONT[1], Takashi TATSUTA[3], Thomas LANGER[3,4], Patrick YU-WAI-MAN[5-8], Pascal REYNIER[9,10], Timothy WAI[1,2]*

1-Mitochondrial Biology Group, Institut Pasteur, CNRS UMR 3691, Paris, France

2-Université de Paris, Paris, France

3-Max-Planck-Institute for Biology of Ageing, Cologne, Germany

4-Cologne Excellence Cluster on Cellular Stress Responses in Aging-Associated Diseases (CECAD), University of Cologne, Cologne, Germany.

5-Cambridge Centre for Brain Repair and MRC Mitochondrial Biology Unit, Department of Clinical Neurosciences, University of Cambridge, Cambridge, UK.

6-Cambridge Eye Unit, Addenbrooke's Hospital, Cambridge University Hospitals, Cambridge, UK.

7-Moorfields Eye Hospital, London, UK.

8-UCL Institute of Ophthalmology, University College London, London, UK.

9-Laboratoire de Biochimie et biologie moléculaire, Centre Hospitalier Universitaire, Angers, France

10-Unité Mixte de Recherche MITOVASC, CNRS 6015, INSERM U1083, Université d'Angers, Angers, France

*Correspondence: timothy.wai@pasteur.fr

bioRxiv preprint doi: https://doi.org/10.1101/2021.01.14.426579; this version posted January 15, 2021. The copyright holder for this preprint (which was not certified by peer review) is the author/funder. All rights reserved. No reuse allowed without permission.

Abstract

Mutations affecting the mitochondrial fusion protein Optic Atrophy 1 (OPA1) cause autosomal dominant optic atrophy (DOA) – one of the most common form of mitochondrial disease. The majority of patients develop isolated optic atrophy, but about 20% of *OPA1* mutation carriers manifest more severe neurological deficits as part of a "DOA+" phenotype. OPA1 deficiency causes mitochondrial fragmentation and also disrupts cristae organization, oxidative phosphorylation, mitochondrial DNA (mtDNA) maintenance, and cell viability. It has not yet been established whether phenotypic severity can be modulated by genetic modifiers of OPA1. To better understand the genetic regulation of mitochondrial dynamics, we established a high-throughput imaging pipeline using supervised machine learning (ML) to perform unbiased, quantitative mitochondrial morphology analysis that was coupled with a bespoke siRNA library targeting the entire known mitochondrial proteome (1531 genes), providing a detailed phenotypic screening of human fibroblasts. In control fibroblasts, we identified known and novel genes whose depletion promoted elongation or fragmentation of the mitochondrial network. In DOA+ patient fibroblasts, we identified 91 candidate genes whose depletion prevents mitochondrial fragmentation, including the mitochondrial fission genes *DNM1L*, *MIEF1*, and *SLC25A46*, but also genes not previously linked to mitochondrial dynamics such as Phosphatidyl Glycerophosphate Synthase (*PGS1*), which belongs to the cardiolipin (CL) synthesis pathway. PGS1 depletion reduces CL content in mitochondria and rebalances mitochondrial dynamics in OPA1-deficient fibroblasts by inhibiting mitochondrial fission, which improves defective respiration, but does not rescue mtDNA depletion, cristae dysmorphology or apoptotic sensitivity. Our data reveal that the multifaceted roles of OPA1 in mitochondria can be functionally uncoupled by modulating mitochondrial lipid metabolism, providing novel insights into the cellular relevance of mitochondrial fragmentation. This study illustrates the power of a first-in-kind objective automated imaging approach to uncover genetic modifiers of mitochondrial disease through high-throughput phenotypic screening of patient fibroblasts.

bioRxiv preprint doi: https://doi.org/10.1101/2021.01.14.426579; this version posted January 15, 2021. The copyright holder for this preprint (which was not certified by peer review) is the author/funder. All rights reserved. No reuse allowed without permission.

Introduction

The morphology that mitochondria adopt within a cell is shaped by opposing events of membrane fusion and fission executed by dynamin-like GTPases[1]. Fission is performed upon recruitment of dynamin related protein 1 (DRP1, encoded by *DNM1L*) to the outer membrane (OMM) via its receptors mitochondrial fission factor (MFF) and mitochondrial division (MiD) 49 and 51, which coalesce at sites of contact with the endoplasmic reticulum (ER)[2] in a manner that depends on the lipid composition of the OMM[3,4]. Mitochondrial fusion is controlled by Mitofusins (MFN) 1 and 2 at the outer membrane and optic atrophy protein 1 (OPA1) in the inner membrane (IMM)[5–7]. Post-translational modifications (PTM) of these proteins can regulate mitochondrial dynamics: Drp1 phosphorylation can alter the recruitment to future sites of mitochondrial division on OMM while at the IMM, proteolytic cleavage of OPA1 from L-OPA1 to S-OPA1 by the mitochondrial proteases OMA1 and the *i*-AAA protease YME1L balances the rates of fusion and fission in response to stress conditions and metabolic stimulation[8]. Mitochondrial shape can shift in response to cellular and extracellular cues both in vitro and in vivo[3,9–12]. Mitochondrial fusion has been proposed to preserve cellular integrity, increase ATP production, and maintain mitochondrial DNA levels (mtDNA)[13,14]. Stress-induced mitochondrial hyperfusion (SiMH), is a cytoprotective response that occurs in response to exogeneous cellular insults including protein synthesis inhibition and nutrient and oxygen deprivation[3,12,15,16] characterized by an elongation of the mitochondrial network resulting from unopposed fusion that requires Opa1 and Mfn1 (but not Mfn2) and the IMM proteolytic scaffold protein stomatin-like protein 2 (Slp2)[15,17]. Slp2 is a cardiolipin (CL) binding protein that defines CL-rich membrane domains of the IMM. CL is a mitochondrial-specific non-bilayer-forming phospholipid that is implicated in a wide array of mitochondrial processes including apoptosis, respiratory chain assembly, protein import, inflammation, and mitochondrial dynamics[18]. The association between mitochondrial dynamics and lipids in mitochondrial and cellular homeostasis is well established, although the nature of this interdependence is less clear.

bioRxiv preprint doi: https://doi.org/10.1101/2021.01.14.426579; this version posted January 15, 2021. The copyright holder for this preprint (which was not certified by peer review) is the author/funder. All rights reserved. No reuse allowed without permission.

Unopposed fission causes mitochondrial fragmentation, which is associated with cellular dysfunction, has been observed in a variety of acquired and inborn disorders, in particular mitochondrial genetic diseases (MD)[1]. Mutations in *OPA1*, which encodes for a dynamin-like GTPase protein, cause autosomal dominant optic atrophy (DOA). The majority of patients manifest isolated optic atrophy (DOA, MIM#165500), but a subgroup develop a more severe disseminated neurological phenotype as part of a DOA "plus" phenotype (DOA+, MIM#125250), including an early-onset Behr-like syndrome (MIM#210000) or encephalomyopathy (MIM# 616896) in a few reported patients with recessive *OPA1* mutations[19,20]. OPA1-deficient cells exhibit a fragmented mitochondrial network due to unopposed fission[6,7]. Beyond mitochondrial fusion, OPA1 plays essential roles in the maintenance of cristae shape, mtDNA levels, OXPHOS complex assembly, cellular proliferation, and apoptotic sensitivity[1]. Over-expression of OPA1 can confer protection against apoptotic cell death[21] without necessarily altering mitochondrial morphology[22], leading to the notion that non-fusion roles of *OPA1* (e.g. cristae maintenance) are functionally separable from IMM fusion but this hypothesis has never been put to the test in OPA1 deficiency[23]. Indeed, how OPA1 is capable of regulating different processes within mitochondria is unclear as is the cellular relevance of mitochondrial fragmentation in OPA1-deficient cells.

Mitochondrial morphology exists on a dynamic spectrum, with *fragmented* and *hypertubular* (or *hyperfused*) referring to the characteristic network morphologies adopted by mitochondria in cells when fusion and fission are inhibited, respectively[1]. Quantification of mitochondrial morphology performed by subjective, user-defined manual classification cells with aberrant mitochondrial networks caused by inhibited fusion[24] or fission[25] as well as enhanced fusion[15,17] or fission[26] has been successfully applied for the over two decades. More recently, the use of computer-assisted segmentation measurement of mitochondrial features[27], such as the length, width, or aspect ratio of mitochondria has gained traction[28]. However, major drawbacks to these approaches remain the manual collection of images, the possibility of user

bioRxiv preprint doi: https://doi.org/10.1101/2021.01.14.426579; this version posted January 15, 2021. The copyright holder for this preprint (which was not certified by peer review) is the author/funder. All rights reserved. No reuse allowed without permission.

bias and the laborious segmentation of mitochondria needed to ascribe morphological traits. The latter also requires spatial resolution at the physical limits of light microscopy in order to accurately and unequivocally separate one mitochondrion from the next. While recent advances in super-resolution nanoscopy of mitochondria may soon render this concern moot[29], only a handful of laboratories have successfully applied this technology for high resolution mitochondrial imaging and its application to high throughput imaging has yet to be established.

In this study, we developed a first-in-kind, high-throughput imaging screening pipeline and identified known and novel mitochondrial genes that can modulate mitochondrial morphology in healthy human fibroblasts and prevent mitochondrial fragmentation in *OPA1* patient fibroblasts, most of which have never previously been linked to mitochondrial dynamics. Among the 91 candidate genes found to supress mitochondrial fragmentation, we discovered that depletion of Pgs1, the mitochondrial phosphatidyl glycerophosphate synthase, lowers cardiolipin levels, inhibits mitochondrial fission and rescues mitochondrial fragmentation and respiration in Opa1-deficient mouse embryonic fibroblasts. Our data unravel an unexpected role of Pgs1 in the regulation of mitochondrial form and function.

bioRxiv preprint doi: https://doi.org/10.1101/2021.01.14.426579; this version posted January 15, 2021. The copyright holder for this preprint (which was not certified by peer review) is the author/funder. All rights reserved. No reuse allowed without permission.

Results

Inhibiting fission rescues mitochondrial fragmentation in OPA1 patient fibroblasts

To overcome limitations of conventional approaches for imaging and quantification of mitochondria in cells, we developed a high content imaging pipeline using confocal spinning disc fluorescence microscopy compatible with multi-well, high throughput automated imaging of live or fixed cells (figure EV1). We adopted an image analysis pipeline (Table S1) that automatically executes cell segmentation enabling the single-cell classification of mitochondrial morphology using supervised machine learning (ML) algorithms trained on defined classes of mitochondrial morphologies, which do not rely on measuring the absolute length or width of a mitochondrion. Instead, training sets (ground truths) were empirically generated by knocking down genes whose depletion is known to provoke either increased or decreased mitochondrial network lengths. To promote mitochondrial fragmentation, we depleted control fibroblasts of *OPA1* and to define hypertubular mitochondria, we inhibited mitochondrial fission by downregulation of *DNM1L*. To define normal, tubular mitochondrial morphology, we treated control cells with non-targeting (NT) siRNAs. Confocal images of hundreds of cells (315-586 cells/training condition) acquired from these training sets were used as ground truths to train the supervised ML algorithm to classify cells as either fragmented, normal, or hypertubular (Figure 1A) during each imaging experiment. This approach proved tremendously robust: siRNA-mediated induction of fragmentation of either *YME1L* or *MFN1/2* was accurately recognized as such by supervised ML training of mitochondrial fragmentation using *OPA1* siRNAs (figure EV1B) and chemical induction of fission with the protonophore carbonyl cyanide m-chlorophenyl hydrazone (CCCP) or hyperfusion with the cytosolic protein synthesis inhibitor cycloheximide (CHX) could be used to accurately quantify mitochondrial fragmentation in Opa1-depleted fibroblasts (figure EV1C). Together, these data validate the supervised ML approach to mitochondrial morphology quantification as a rapid, robust, and unbiased approach for the

bioRxiv preprint doi: https://doi.org/10.1101/2021.01.14.426579; this version posted January 15, 2021. The copyright holder for this preprint (which was not certified by peer review) is the author/funder. All rights reserved. No reuse allowed without permission.

quantitative assessment of mitochondrial shape in fibroblasts using a variety of genetic or chemical training sets as ground truths.

Genetic knockouts, siRNA depletion and chemical modulation experiments induce drastic alterations in mitochondrial shape that are easily recognizable but do not necessarily reflect the phenotypic severity observed in patient cells or disease models, which are often hypomorphic, yielding more subtle biochemical and cell biological alterations. To determine whether our supervised ML approach to mitochondrial morphology quantification was compatible with the high throughput interrogation of patient cells, we imaged and analyzed control and DOA+ patient-derived skin fibroblasts carrying pathogenic, mono-allelic mutations in *OPA1* known to cause mitochondrial fragmentation (R445H, S545R)[30,31] and mutations whose effects on mitochondrial morphology have not yet been reported[30] (I432X, c.2356-G>T, and Q297X) (Figure 1B and Table 1). Our analyses revealed both $OPA1^{S545R}$ and, to a lesser extent, $OPA1^{R445H}$ patient fibroblasts exhibited significant increases in the proportion of cells with a fragmented mitochondrial phenotype: 45.2 $\pm$ 5.3 % of $OPA1^{S545R}$ fibroblasts (2282 cells analyzed) and : 16.8 $\pm$ 9.2 % of $OPA1^{R445H}$ fibroblasts (2683 cells analyzed) were fragmented compared to 4.5 to 11.1 % of control fibroblasts from three healthy, unrelated individuals (CTL-1; 11.1 $\pm$ 7.1 %, CTL-2; 6.1 $\pm$ 3.2 %, CTL-3; 4.5 $\pm$ 5.2 %, 879-3823 cells analyzed) (Figure 1B, C). These data are in accordance with previous measurements made in these cells using manual, lower-throughput imaging and quantification methods[27,31]. Curiously, we did not detect significant mitochondrial morphology defects in $OPA1^{I432V}$, $OPA1^{c.2356\text{-}1G>T}$ nor $OPA1^{Q297X}$ patient fibroblasts even though they were derived from patients also suffering from the same pathology: DOA+. Western blot analyses revealed a reduction of OPA1 protein of 21.5% ± 3.2 in $OPA1^{S545R}$ lysates and 58.2% ± 9.2 in $OPA1^{Q297X}$ lysates (figure EV1D). Aberrant mitochondrial morphology measured in patient-derived fibroblasts did not correlate with the steady state levels of OPA1 nor with the reported clinical symptoms (Table 1), suggesting that additional factors

bioRxiv preprint doi: https://doi.org/10.1101/2021.01.14.426579; this version posted January 15, 2021. The copyright holder for this preprint (which was not certified by peer review) is the author/funder. All rights reserved. No reuse allowed without permission.

beyond pathogenic mutations in *OPA1* may be capable of modulating mitochondrial morphology.

In animal models of MD, mitochondrial fragmentation can be rebalanced by additional inhibition of mitochondrial fission[32–34], but this approach has not been tested in humans. To test whether decreasing mitochondrial fission is capable of rebalancing mitochondrial morphology in *OPA1* mutant patient fibroblasts, we knocked down *DNM1L* by siRNA (Figure 1D). DRP1 depletion in in *OPA1*^{S545R} fibroblasts led to an increased proportion of cells with normal and hypertubular mitochondria while reducing those with fragmented mitochondria (Figure 1E), reaching proportions similar to those observed in control fibroblasts (13.4% ± 11.0 in CTL-1 vs. 18.5%±13.9 in *OPA1*^{S545R}). These data indicate that inhibiting fission can restore mitochondrial morphology in OPA1 mutant fibroblasts exhibiting mitochondrial fragmentation. In addition, depletion of *OPA1* by siRNA treatment in *OPA1*^{S545R} patient fibroblasts further increased mitochondrial fragmentation by 34.5% (1.34-fold change), implying partial functionality of OPA1 protein present in *OPA1*^{S545R} patient fibroblasts. Indeed, treatment of *OPA1*^{S545R} patient fibroblasts with CHX led to an elongation of the mitochondrial network (Figure 1F) characterized by reduced mitochondrial fragmentation (Figure 1G), indicating that *OPA1*^{S545R} cells are capable of performing SiMH and therefore retain some functional OPA1[15]. These data lend experimental support to a previously proposed genetic haploinsufficiency in DOA[35] caused by monoallelic pathogenic mutations. Taken together, these data outline a straightforward and unbiased manner to identify and correct mitochondrial fragmentation in patient-derived fibroblasts.

High-throughput screening identifies known and novel modifiers of mitochondrial morphology in control fibroblasts

In an effort to identify mitochondrial proteins that regulate OPA1 dynamics, we established an imaging-based screening pipeline to quantitatively assess the impact of all mitochondrial genes

bioRxiv preprint doi: https://doi.org/10.1101/2021.01.14.426579; this version posted January 15, 2021. The copyright holder for this preprint (which was not certified by peer review) is the author/funder. All rights reserved. No reuse allowed without permission.

on mitochondrial morphology. To do this we coupled automated imaging and supervised ML mitochondrial morphology quantification workflow (Figure 1A) with a bespoke siRNA library targeting 1531 known and putative nuclear-encoded mitochondrial genes (henceforth termed the *Mitome* siRNA library) generated based on publicly accessible databases of mitochondrial genes[36,37] (see Table S2 for gene list and plate distribution). This list is more extensive than MitoCarta 3.0 and also includes targets gene products whose function and localization have not yet been experimentally defined. *SmartPool* siRNAs (4 siRNAs per gene per pool) were spotted individually across six 384 well plates, which also contained siRNAs for *DNM1L*, *OPA1*, *YME1L*, and *MFN1/2* that could serve as read-outs for downregulation efficiency within and between plates as well as ground truths for supervised ML (figure EV2A-C, (Z-score = 0.72875 $\pm$ 0.1106). We began by *Mitome* screening in healthy control fibroblasts (CTL-1 and CTL-2) and identified 22 genes whose downregulation led to the fragmentation of the mitochondrial network and 145 genes that lead to hypertubulation above thresholds that were defined post-hoc using a univariate 3-component statistical model we developed in R (Table S3). Among the genes whose ablation induced mitochondrial fragmentation, we identified established components required for the maintenance of tubular mitochondria including *YME1L*, *OPA1*, and *MFN1* (Figure 2B, Table S3). We also identified factors already described to modify mitochondrial morphology including *AMBRA1*, *GOLPH3*, and *PPTC7*. AMBRA1, which stands for activating molecule in Beclin-1-regulated autophagy, is an autophagy adapter protein regulated by mTORC1 that has been linked to mitophagy and programmed cell death, all of which are associated with fragmentation of the mitochondrial network. Golgi phosphoprotein 3 (GOLPH3) regulates Golgi morphology and mitochondrial mass and cardiolipin content through undefined mechanisms[38]. PPTC7 encodes a mitochondrial phosphatase shown to be essential for post-natal viability in mice. EM analyses in heart and liver sections of *Pptc7*$^{-/-}$ mice revealed smaller, fragmented mitochondria[39], consistent with our findings in human fibroblasts (figure EV2D).

bioRxiv preprint doi: https://doi.org/10.1101/2021.01.14.426579; this version posted January 15, 2021. The copyright holder for this preprint (which was not certified by peer review) is the author/funder. All rights reserved. No reuse allowed without permission.

Among the genes whose ablation induced mitochondrial hypertubulation (Figure 2C), we identified *DNM1L*, its receptors *MIEF1* and *MFF*, as well as *USP30* and *SLC25A46*. USP30 encodes a deubiquitinase that is anchored to the OMM where it contributes to mitochondrial fission in a Drp1-dependent fashion[40]. Depletion of USP30 has been shown promote mitochondrial elongation and mitophagy[41]. SLC25A46, which encodes for an outer membrane protein with sequence homology to the yeast mitochondrial dynamics regulator Ugo1, is required for mitochondrial fission. In human fibroblasts, depletion by siRNA or pathogenic loss-of-function mutations lead to hypertubulation of the mitochondrial network[42,43]. Similarly, depletion of MFF and/or MiD51 in fibroblasts inhibits DRP1-dependent mitochondrial fission and results in mitochondrial hypertubulation[25]. Pathogenic mutations in *MFF* cause optic and peripheral neuropathy and fibroblasts from these patients exhibit mitochondrial elongation[44]. In addition to known regulators of mitochondria morphology, we also discovered a number of known mitochondrial genes whose functions have not previously associated with mitochondrial dynamics, including *LIPT1, LIPT2*, and *BCKDHA*. *LIPT1* and *LIPT2* encode mitochondrial lipoyltransferases, which are involved in the activation of TCA cycle enzyme complexes and branched-chain ketoacid dehydrogenase (BCKD) complex. *BCKDHA* the E1-alpha subunit of the BCKD that is involved in the catabolism of amino acids isoleucine, leucine, and valine. Mutations in either *LIPT1*[46], *LIPT2*[47], or *BCKDHA*[48] causes inborn errors of metabolism, although the effects on mitochondrial morphology have never been investigated. Finally, we also discovered a cluster of genes (figure EV2D) encoding proteins required for ribosome assembly and cytosolic translation (*RPL10, RPL10A, RPL8, RPL36AL, RPS18*). To our knowledge, depletion of cytosolic ribosomal genes has never been associated with mitochondrial hyperfusion, although chemical inhibition of proteins synthesis is the most commonly used triggers for SiMH[49]. These data are consistent with the mitochondrial elongation induced by treatment of control fibroblasts (Figure 1G, H) with CHX, which inhibits cytosolic translation. Altogether, our data demonstrate the robustness of our imaging-based

bioRxiv preprint doi: https://doi.org/10.1101/2021.01.14.426579; this version posted January 15, 2021. The copyright holder for this preprint (which was not certified by peer review) is the author/funder. All rights reserved. No reuse allowed without permission.

248 phenotypic screening and mitochondrial morphology quantification approach for the
249 identification of both known and novel genes controlling mitochondrial morphology and provide
250 a valuable resource for the investigation of mitochondrial dynamics.
251
252 **High-throughput screening in patient-derived *OPA1* mutant fibroblasts identifies**
253 **suppressors of mitochondrial fragmentation**
254 We sought to apply the *Mitome* screening approach to identify novel regulators of OPA1 acting
255 as genetic suppressors of mitochondrial fragmentation in *OPA1*^{S545R} fibroblasts. After 72 hours
256 of siRNA treatment, we acquired images of hundreds of cells per well (257 to 1606) and then
257 classified mitochondrial morphology by applying a training sets comprised of *OPA1*^{S545R}
258 fibroblasts transfected with NT siRNAs (fragmented), *OPA1* siRNAs (hyperfragmented) or
259 *DNM1L* siRNAs (rescued). Application of our imaging and quantification pipeline identified 91
260 candidate genes whose downregulation rescued mitochondrial fragmentation (Figure 2D, figure
261 EV2C, Table S4) as well as 27 genes that further fragmented the mitochondrial network (figure
262 EV2D, Table S4) such as *OPA1*, *YME1L*, and *SURF1*. As expected, among the 91 candidates,
263 39 of these genes were also discovered to hypertubulate mitochondria in control fibroblasts
264 upon downregulation (Figure 2C, F), including regulators of mitochondrial fission such as
265 *SLC25A46*[42], *MFF*[50], *MIEF1*[25], and *DNM1L*[51]. We also discovered factors interacting with the
266 MICOS complex (DNAJC4, DNAJC11), which was unexpected given that disruption of the
267 MICOS and respiratory chain complexes is usually associated with fragmentation rather than
268 elongation of the mitochondrial network[52]. Like in control fibroblasts, our data revealed a cluster
269 of ribosomal genes previously linked to mitochondria (*RPL15, RPS15A, RPLP2, RPL36AL,*
270 *RPL5*, and *RPS18*) essential for cytosolic translation, implying that inhibition of protein synthesis
271 can suppress mitochondrial fragmentation in *OPA1*^{S545R} patient fibroblasts. These data are
272 concordant with the discovery that *OPA1*^{S545R} patient fibroblasts can perform SiMH in the
273 presence of the cytosolic protein inhibitor CHX (Figure 1F, G). The *Mitome* siRNA screen of

bioRxiv preprint doi: https://doi.org/10.1101/2021.01.14.426579; this version posted January 15, 2021. The copyright holder for this preprint (which was not certified by peer review) is the author/funder. All rights reserved. No reuse allowed without permission.

OPA1^{S545R} fibroblasts identified a wide array of well-characterized genes not previously linked to mitochondrial dynamics including some required for mitochondrial gene expression and maintenance (*TFB1M, MTERF4, MRPL53, GFM2, MRPS18A*), oxidative phosphorylation (*NDUFAF1, COX6A2, ETHE1, COX20, ETFDH*), amino acid metabolism (*BCKDHA, GLUD2, DAOA, MCCC1, GLYAT*), one-carbon and serine metabolism (*MMAA, SHMT2, MTHFD1L, MTHFD2L*), and lipid biosynthesis (*PGS1, PISD, BZRAP1*) as well as orphan genes (*C15orf62, C15orf61, C3orf33*) (Figure 2E, Table S4). In conclusion, we successfully applied an unbiased, high throughput imaging approach and identified a large number of candidate suppressors of mitochondrial dysfunction in MD patient-derived fibroblasts, none of which are known to be implicated in the modulation of clinical or biochemical severity caused by OPA1 mutations. .

PGS1 depletion rescues mitochondrial fragmentation in OPA1-deficient fibroblasts

One of the top hits from the *Mitome* siRNA screen able to rescue aberrant mitochondrial morphology in *OPA1*^{S545R} patient fibroblasts or promote mitochondrial hypertubulation in control fibroblasts, *PGS1*, encodes a CDP-diacylglycerol-glycerol-3-phosphate 3-phosphatidyltransferase[53] that catalyzes the synthesis of phosphatidylglycerol phosphate (PGP), the rate limiting step in the synthesis of cardiolipin (CL) (Figure 5A)[54]. CL is a mitochondria-specific phospholipid synthesized and primarily located in the IMM and is important for various mitochondrial functions including protein and metabolite import, cristae maintenance, programmed cell death regulation, and oxidative phosphorylation[55]. Recent work from the Ishihara lab reported CL to be important for membrane fusion by OPA1, implying that CL deficiency would impair mitochondrial fusion and drive fragmentation[56].

We sought to confirm that *PGS1* depletion indeed inhibits mitochondrial fragmentation by treating *OPA1*^{S545R} fibroblasts with siRNAs directed against it. PGS1 depletion significantly reduced the proportion of cells with fragmented mitochondria and we discovered it could only do so if OPA1 was not totally depleted (Figure 3A, B). *OPA1*^{S545R} patient fibroblasts and *OPA1*

bioRxiv preprint doi: https://doi.org/10.1101/2021.01.14.426579; this version posted January 15, 2021. The copyright holder for this preprint (which was not certified by peer review) is the author/funder. All rights reserved. No reuse allowed without permission.

siRNA-treated CTL-1 fibroblasts were resistant to mitochondrial elongation by *PGS1* depletion, although *DNM1L* ablation could still rescue mitochondrial fragmentation in these cells. These data argue that *PGS1* depletion is effective in rebalancing mitochondrial dynamics in the context of a hypomorphic OPA1 mutations[57] and not when OPA1 is completely absent.

Functional exploration of mitochondrial biology in primary human fibroblasts is challenging due to the slow proliferation rates, low metabolic activity, poor transfection efficiency, genetic heterogeneity, and cellular senescence. To circumvent these limitations, we pursued further studies in mouse embryonic fibroblasts (MEFs) in which we partially ($Opa1^{Crispr}$) or completely ($Opa1^{KO}$) ablated Opa1 (figure EV3A,B). To generate hypomorphic *Opa1* mutant MEFs ($Opa1^{Crispr}$), we employed Crispr/Cas9 to initiate a targeted disruption of Exon 4, which is in the most highly expressed functional splice isoforms of the 8 isoforms of *Opa1* in mice[58,59] (figure EV3A). We sorted individual $Opa1^{Crispr}$ MEF clones by flow cytometry and screened for positive clones using mitochondrial fragmentation as an initial readout. DNA sequencing of *Opa1* in positive clones was performed by Illumina HighSeq Deep Sequencing of PCR amplicons covering the targeted region. $Opa1^{Crispr}$ MEFs harbored a c.5013delA mutation, predicted to prematurely truncate Opa1 at position 178, and a 107 bp deletion at c.503 extending through the end of Exon 4 and into Intron 4, predicted to prematurely truncate Opa1 at position 182 in Exon 5. These deletions yielded frame shift and missense mutations causing a ~80% reduction in steady-state protein levels in $Opa1^{Crispr}$ MEFs (Figure 3G, H) and a ~50% reduction in *Opa1* mRNA levels (figure EV3C). $Opa1^{Crispr}$ MEFs exhibited mitochondrial fragmentation (Figure 3C, D) that could be rescued by stable re-expression of Opa1-isoform 1 with (figure EV3D-F) or without a C-terminal 9xMyc tag construct[60] (Figure 3E, F), validating the targeted disruption of *Opa1*. Similarly, to hypomorphic $OPA1^{S545R}$ patient-derived fibroblasts, $Opa1^{Crispr}$ MEFs exhibited hypomorphy, as evidenced by the ability of *Opa1* siRNA treatment to further increased mitochondrial fragmentation (figure EV3H, I) to levels observed in $Opa1^{KO}$ MEFs (figure EV3L,

bioRxiv preprint doi: https://doi.org/10.1101/2021.01.14.426579; this version posted January 15, 2021. The copyright holder for this preprint (which was not certified by peer review) is the author/funder. All rights reserved. No reuse allowed without permission.

M) and the ability of *Opa1*^{Crispr} MEFs to undergo SiMH (figure EV3J, K), which was not possible in *Opa1*^{KO} MEFs (figure EV3L, M).

Next, we tested whether Pgs1 depletion could rescue mitochondrial fragmentation in *Opa1*^{Crispr} MEFs. Pgs1 ablation, either by siRNA (Figure 3C, D) or Crispr/Cas9-mediated NHEJ (Figure 3E, F) prevented mitochondrial fragmentation, leading to the re-establishment of wild type mitochondrial network morphology. qRT-PCR measurement of *Pgs1* mRNA levels showed a 25 ± 8.3% reduction in Pgs1 mRNA in *Opa1*^{Crispr}*Pgs1*^{Crispr} MEFs (figure EV3C) and a 71.9 ± 8.4% percent reduction in *Pgs1* siRNA-treated *Opa1*^{Crispr} MEFs (Figure 5D). To confirm that mitochondrial morphology rescue in *Opa1*^{Crispr}*Pgs1*^{Crispr} MEFs did not arise from unlikely and unintended reversions of mutant *Opa1*, we performed DNA sequence analyses by Illumina HighSeq Deep Sequencing of *Opa1*^{Crispr}*Pgs1*^{Crispr} MEF PCR amplicons from the targeted locus. *Opa1*^{Crispr}*Pgs1*^{Crispr} MEFs carried the same *Opa1* loss of function mutations as the parental *Opa1*^{Crispr} MEFs as well as an additional mutation in *Pgs1* (c.218delGTGTA), predicted to result in a frameshift at Gly73. Stable re-expression of Pgs1 restored *Pgs1* mRNA levels in *Pgs1*^{Crispr} MEFs (figure EV3c) and resulted in fragmentation of the (rescued) mitochondrial network in *Opa1*^{Crispr}*Pgs1*^{Crispr} MEFs (Figure 3E, F) back to WT levels. To exclude the possibility that Pgs1 depletion rescues mitochondrial morphology of *Opa1*^{Crisprr} MEFs by indirectly elevating Opa1 expression, we assessed Opa1 protein levels by Western blot. *Opa1*^{Crispr}*Pgs1*^{Crispr} MEFs exhibited levels of total Opa1 levels and L-Opa11/S-Opa1 ratios (Figure 3G, H) similar to the parental *Opa1*^{Crispr} cells, indicating that restored mitochondrial morphology in *Opa1*^{Crispr}*Pgs1*^{Crispr} MEFs is not the result of rescued Opa1 expression. Taken together, our results demonstrate that Pgs1 depletion can rescue mitochondrial fragmentation caused by Opa1 deficiency in both mouse and human fibroblasts.

PGS1 depletion rescues mitochondrial fragmentation by inhibiting mitochondrial fission.

bioRxiv preprint doi: https://doi.org/10.1101/2021.01.14.426579; this version posted January 15, 2021. The copyright holder for this preprint (which was not certified by peer review) is the author/funder. All rights reserved. No reuse allowed without permission.

We sought to understand whether Pgs1 depletion restores normal mitochondrial morphology by increasing mitochondrial fusion or reducing mitochondrial fission. We examined the levels of proteins involved in mitochondrial dynamics by Western blot (figure EV4A, B) and we observed no significant alterations in the steady state levels of known fusion (Mfn1, Mfn2) and fission (Mff, MiD49, MiD51, Fis1) regulators in *Opa1*^{Crispr}*Pgs1*^{Crispr} MEFs, yet we did observe elevated Drp1 levels in *Opa1*^{Crispr} MEFs, which returned to WT levels in *Opa1*^{Crispr}*Pgs1*^{Crispr} MEFs. To test whether increased levels of Drp1 promoted its recruitment to mitochondria, we stably expressed mitoTag constructs (OMP25-EGFP-HA or OMP25-EGFP-Myc) in MEFs to in order to perform affinity purification and partitioning of mitochondria from cytosolic contents[61]. Immunoblot analyses demonstrated an increase in total Drp1 levels in *Opa1*$^{Crispr\ mitoTag}$ MEFs compared to other genotypes but did not show an increase in the partitioning of mitochondrial and non-mitochondrial (cytosolic) Drp1 at steady state (Figure 4A). We further corroborated these findings by examining the subcellular distribution of Drp1 by indirect immunochemistry studies, which also revealed no differences in Drp1 colocalization *Opa1*^{Crispr}, *Opa1*^{Crispr}*Pgs1*^{Crispr} and *Pgs1*^{Crispr} MEFs relative to WT (Figure 4B). MEFs deleted of all three essential Drp1 receptors, Mid51/Mid49/Mff, exhibited markedly less Drp1 recruitment as previously demonstrated, and were used as a negative control[25].

To assess mitochondrial division in living *Opa1*^{Crispr}*Pgs1*^{Crispr} MEFs, we performed quantitative kinetic measurements of mitochondrial morphology in the presence of established pharmacological inducers of mitochondrial fragmentation: CCCP and the Ca^{2+} ionophore 4Br-A23187. Both chemicals cause Drp1-dependent mitochondrial fragmentation but CCCP triggers Oma1-dependent Opa1 processing[8] that both accelerates fission and inhibits fusion while 4Br-A23187 treatment induces Ca^{2+}-dependent fragmentation without stress-induced Opa1 processing[62] (figure EV4C). Treatment of *Opa1*^{Crispr}*Pgs1*^{Crispr} MEFs with CCCP (Figure 4C) or 4Br-A23187 (figure EV4D) induced a progressive fragmentation of the mitochondrial network over several hours with kinetics similar to that of WT MEFs, implying that rescued mitochondrial

bioRxiv preprint doi: https://doi.org/10.1101/2021.01.14.426579; this version posted January 15, 2021. The copyright holder for this preprint (which was not certified by peer review) is the author/funder. All rights reserved. No reuse allowed without permission.

morphology conferred to *Opa1*^{Crispr} MEFs depleted (Figure 3C) or deleted (Figure 3E) was not caused by an inhibition of Drp1. We discovered Pgs1-depleted MEFs to be largely resistant to CCCP-induced fragmentation for the duration of the experiment: incubation with 5μM CCCP for 10h led to a 1.70 rate of fragmentation in WT MEFs and only 0.06 rate of fragmentation in *Pgs1*^{Crispr} MEFs (Figure 4C,D). Similarly, induction of mitochondrial fission with 4Br-A23187 did not promote mitochondrial fragmentation rates observed in WT MEFs (figure EV4D,E). Given the resistance to uncoupler-induced mitochondrial fragmentation, we determined the mitochondrial membrane potential of *Pgs1*^{Crispr} MEFs by labeling MEFs with the potentiometric membrane marker TMRE, which we normalized to genetically encoded mitoYFP. We observed a significant increase in membrane potential in *Pgs1*^{Crispr} MEFs (figure EV4F), which was reduced upon stable re-expression of Pgs1, which also re-sensitized cells to CCCP (Figure 4C,D) and 4Br-A23187 -induced fragmentation (figure EV4H, I). Despite the increase in basal membrane potential, we observed no difference in the proclivity of *Pgs1*^{Crispr} MEFs to undergo proteolytic cleavage of Opa1 in response to CCCP-induced Oma1 activation (figure EV4G), indicating that the proteolytic activity of Oma1 is functional in Pgs1-depleted cells. Taken together, we conclude that Pgs1 depletion can inhibit mitochondrial fragmentation by slowing mitochondrial fission in a manner that is independent of Opa1 processing by Oma1.

Pgs1 depletion improves SiMH without restoring basal fusion to Opa1-deficient cells

To test whether Pgs1 depletion also affected mitochondrial fusion in *Opa1*^{Crispr} MEFs we assessed inner membrane fusion kinetics using a fluorescence recovery after photobleaching (FRAP) assay[63]. Genetically encoded matrix-localized YFP (mitoYFP) was photobleached in a subsection of mitochondria and imaged 200 ms intervals (Figure 4F). In WT MEFs, mitoYFP single increased ~2.5-fold in the photobleached region of the network within a few seconds, demonstrating active mitochondrial fusion in these cells. As expected, FRAP experiments performed under the same conditions in *Opa1*^{Crispr} MEFs revealed no significant

bioRxiv preprint doi: https://doi.org/10.1101/2021.01.14.426579; this version posted January 15, 2021. The copyright holder for this preprint (which was not certified by peer review) is the author/funder. All rights reserved. No reuse allowed without permission.

recovery of mitoYFP signal, indicating a block in mitochondrial fusion, which was not improved upon additional deletion of *Pgs1* (in *Opa1*^{Crispr}*Pgs1*^{Crispr} MEFs) despite the appearance of a normal, tubular network in these cells (Movies 1-3). These results indicate Pgs1 depletion does not restore basal mitochondrial fusion function to *Opa1*^{Crispr} MEFs.

Next, we sought to determine *Opa1*^{Crispr}*Pgs1*^{Crispr} cells could undergo mitochondrial elongation induced by SiMH, despite an inhibition of IMM fusion. Live imaging of cells stimulated with CHX (Figure 4F, G) or the transcriptional inhibitor Actinomycin D (ActD) (figure EV4H, I) induced progressive mitochondrial hypertubulation in both WT and *Opa1*^{Crispr}*Pgs1*^{Crispr} MEFs, implying normal hyperfusion capacity. These responses could be blunted in *Opa1*^{Crispr}*Pgs1*^{Crispr} MEFs by re-expression of Pgs1 (Figure 4F,G, EV4H, I), indicating that Pgs1 activity inhibits SiMH in Opa1-deficient cells. In *Pgs1*^{Crispr} cells, we observed a more rapid hypertubulation in response to SiMH than in WT MEFs (figure EV4H, I). In hypomorphic *Opa1*^{Crispr} MEFs, we also observed a very modest but significant SiMH response, characterized by mitochondrial aggregation in *Opa1*^{Crispr} MEFs in the presence of CHX (Figure 4F, G) or ActD (figure EV4H, I) and stable re-expression of Opa1 fully rescued mitochondrial morphology and SiMH response. MEFs devoid of any detectable Opa1 protein were unable to perform SiMH (figure EV3L, M) consistent with previous reports[15]. Notably, Pgs1-depletion also failed to restore normal mitochondrial morphology in *Opa1*^{KO} MEFs (figure EV5A, B), implying that the functional suppression of mitochondrial fragmentation by Pgs1 depletion depends on the severity of Opa1 deficiency. Thus, we conclude that Pgs1 depletion can re-establish SiMH response to *Opa1*^{Crispr} MEFs without improving mitochondrial fusion under basal condition. Altogether, our data demonstrate that Pgs1 depletion inhibits mitochondrial fragmentation in hypomorphic Opa1 mutant fibroblasts by inhibiting mitochondrial fission and not be increasing mitochondrial fusion.

Downregulation of cardiolipin synthesis pathway enzymes can prevent mitochondrial fragmentation in Opa1-deficient cells

bioRxiv preprint doi: https://doi.org/10.1101/2021.01.14.426579; this version posted January 15, 2021. The copyright holder for this preprint (which was not certified by peer review) is the author/funder. All rights reserved. No reuse allowed without permission.

PGS1 synthetizes phosphatidyl glycerophosphate (PGP) from CDP-diacylglycerol (CDP-DAG) and glycerol 3-phosphate (G3P)[53] (Figure 5A). PGP is dephosphorylated to phosphatidylglycerol (PG) by PTPMT1[64], which is either degraded to DAG or reacts with CDP-DAG to form CL in a reaction catalyzed by cardiolipin synthase, encoded by *Cls1*[65]. Export of mature CL to the OMM is subsequently converted by mitoPLD to phosphatidic acid (PA), which inhibits fission by reducing Drp1 recruitment. PA can also be converted to DAG by Lipin1b to promote Drp1 recruitment and mitochondrial fragmentation[4,62,66,67]. Since we observed no alterations in Drp1 recruitment in Pgs1-depleted cells (Figure 4A, B) and Pgs1 itself is an IMM enzyme, we decided to test whether interfering with CL biosynthesis enzymes localized in the IMM (Figure 5A) could reverse mitochondrial fragmentation of Opa1-deficient fibroblasts. We performed a series of knockdown experiments in WT and *Opa1*^{Crispr} MEFs using siRNAs targeting genes encoding enzymes both upstream (*Prelid1*, *Tamm41*) and downstream (*Ptpmt1*, *Cls1*) of *Pgs1* and analyzed mitochondrial morphology after 72h (Figure 5B). Like the downregulation of *Pgs1*, we discovered that acute, single depletion of *Tamm41*, *Ptpmt1*, or *Cls1* could prevent mitochondrial fragmentation in *Opa1*^{Crispr} MEFs (Figure 5B, C). *Opa1*^{KO} MEFs did not respond to *Pgs1* or *Tamm41* depletion: mitochondrial morphology still remains fragmented upon siRNA treatment (figure EV5A, B). *Preldi1* depletion lead to increased mitochondrial fragmentation in both *Opa1*^{Crispr} and WT MEFs, confirming previous observations in HeLa cells[68]. qRT-PCR analyses revealed significant transcriptional remodeling of CL enzymes in *Opa1*^{Crispr} and WT MEFs (Figure 5D). *Opa1*^{Crispr} MEFs showed an upregulation of *Prelid1*, *Tamm41*, *Pgs1*, *Ptpmt1*, and, to a greater extent, *Cls1*. *Prelid1* depletion led to an upregulation of *Tamm41*, *Ptpmt1*, and *Cls1* concomitant with a reduction in *Pgs1* mRNA levels in both *Opa1*^{Crispr} and WT MEFs. *Tamm41* depletion had more modest effects on the upregulation of *Prelid1* and *Ptpmt1*. Of note, *Pgs1* depletion led to 3 to 5-fold increases in the levels of *Tamm41*, *Ptpmt1,* and *Cls1* in WT MEFs but not in *Opa1*^{Crispr} MEFs. Similarly, *Cls1* depletion led to similarly large increases the levels of *Prelid1*, *Tamm41*, and *Ptpmt1* mRNA in WT MEFs

bioRxiv preprint doi: https://doi.org/10.1101/2021.01.14.426579; this version posted January 15, 2021. The copyright holder for this preprint (which was not certified by peer review) is the author/funder. All rights reserved. No reuse allowed without permission.

but not in *Opa1*^{Crispr} MEFs (Figure 5D), suggesting that there may be underlying defects in CL responses in *Opa1*^{Crispr} MEFs.

Depletion of either Opa1 or Pgs1 reduces cardiolipin levels

We sought to determine the impact of Opa1 and Pgs1 depletion on the levels of CL. Quantitative phospholipidomic analyses of *Opa1*^{Crispr} MEFS revealed a reduction in CL content to 70.1 $\pm$ 11.0% of WT levels (Figure 5E). In addition, CL acyl chain composition analyses showed an increase in double bonds (figure EV5C) and altered acyl chain lengths (figure EV5D). Depletion of Pgs1 via siRNA treatment of WT MEFs for *Pgs1* or, to a lesser degree, *Tamm41* (Figure 5E) reduced the steady state levels of CL to levels similar to those of *Opa1*^{Crispr} MEFs. Depletion of either Pgs1 or Tamm41 in *Opa1*^{Crispr} MEFs lead to a further depletion of CL levels but not further alteration in acyl chain composition of CL. Overall, we found no correlation between the levels or saturation state of CL and mitochondrial morphology, prompting us to consider the possibility that suppression of Pgs1 or Tamm41 in *Opa1*^{Crispr} MEFs restores mitochondrial morphology not via a reduction in CL production but rather through the accumulation of its precursor(s). The CL precursor common to cells depleted of Tamm41, Pgs1, and Cls1 is PA, which is first synthesized in the ER and shuttled from the OMM to the IMM by the lipid transfer protein Prelid1[68]. Suppression of PA delivery to the IMM via Prelid1 ablation causes mitochondrial fragmentation. PA accumulation in the IMM affects mitochondrial structure in yeast[69], but its role in mammalian mitochondria has not been defined. To test whether local accumulation of PA in the IMM is responsible for the anti-fragmentation effect of Pgs1 depletion on mitochondrial morphology, we pursued a genetic approach since lipid analyses of whole mitochondria cannot be used to define the submitochondrial localization of PA. We depleted *Prelid1* in WT and *Pgs1*^{Crispr} MEFs and assessed mitochondrial morphology after 72 hours (Figure 5G). *Preldi1* depletion was able to fragment mitochondria in Pgs1-deficienct cells, arguing that the IMM accumulation of PA resulting from a block in the

bioRxiv preprint doi: https://doi.org/10.1101/2021.01.14.426579; this version posted January 15, 2021. The copyright holder for this preprint (which was not certified by peer review) is the author/funder. All rights reserved. No reuse allowed without permission.

biosynthesis of CL (via Pgs1 depletion) impedes mitochondrial fission. Prelid1 depletion did not fragment mitochondria in Drp1-deficient (*Dnm1l*^{Crispr}) MEFs, demonstrating that PA depletion at the IMM promotes mitochondrial fragmentation in a Drp1-dependent fashion, perhaps by increasing the accumulation of PA at the OMM[62]. Taken together, these data argue that IMM accumulation of the CL precursor PA but not CL itself is responsible for the inhibition of mitochondrial fragmentation in a Drp1-dependent manner.

Pgs1 depletion does not alter apoptotic sensitivity nor cristae dysmorphology caused by Opa1 depletion.

Opa1 regulates cristae morphology and apoptosis in cultured cells[1]. To test whether restoration of mitochondrial morphology in *Opa1*^{Crispr} *Pgs1*^{Crispr} MEFs affects programmed cell death, we stimulated MEFs with apoptosis-inducing compounds and followed the evolution of cell death by live-cell imaging (Figure 6A, B, EV6A-D). We kinetically imaged thousands of cells (2000-12000) every hour over 24 hours and tracked NucBlue and propidium iodide (PI) as markers of total and dead cells, respectively. In the presence of ABT-737 and Actinomycin D (ActD) cell death was triggered more rapidly in *Opa1*^{Crispr} cells compared to WT, which could be inhibited by the pan-caspase inhibitor qVD. *Opa1*^{Crispr} *Pgs1*^{Crispr} MEFs exhibited cell death profiles indistinguishable from *Opa1*^{Crispr} MFEs, indicating that rescued mitochondrial morphology does not protect against apoptotic sensitivity caused by Opa1 depletion. In the presence of staurosporine (figure EV6A, B) or etoposide (figure EV6C, D), *Opa1*^{Crispr} *Pgs1*^{Crispr} cell death sensitivity also did not return to WT levels. *Opa1*^{Crispr} cells exhibited reduced caspase-dependent cell death in the presence of staurosporine or etoposide, confirming previous observations of the stimuli-dependent apoptotic outcomes of haplo-insufficient Opa1-deficient MEFs[70]. Notably, *Pgs1*^{Crispr} cells exhibited increased apoptotic resistance relative to WT cells when challenged with staurosporine, etoposide, or ABT-737 and ActD.

bioRxiv preprint doi: https://doi.org/10.1101/2021.01.14.426579; this version posted January 15, 2021. The copyright holder for this preprint (which was not certified by peer review) is the author/funder. All rights reserved. No reuse allowed without permission.

To assess the impacts on mitochondrial ultrastructure, we performed transmission electron microscopy on WT, *Opa1*^{Crispr} *Pgs1*^{Crispr}, *Opa1*^{Crispr} and *Pgs1*^{Crispr} MEFs. WT cells exhibited inner membranes organized as lamellar cristae, which were disrupted as expected in *Opa1*^{Crispr} cells, which also had more rounded mitochondria consistent with the fragmented network morphology previously described (Figure 6C, D). However, inner membrane structure in *Opa1*^{Crispr} *Pgs1*^{Crispr} was not restored to WT morphology, indicating that mitochondrial morphology and cristae organization are uncoupled in these cells. We did not detect cristae defects in *Pgs1*^{Crispr} cells, implying that CL reduction per se (Figure 5E) does cause defective mitochondrial ultrastructure in mammalian cells. Taken together, our data demonstrate that the role of Opa1 in balancing mitochondrial dynamics can be uncoupled from its role as an organizer of inner membrane structure and programmed cell death.

Rebalancing mitochondrial dynamics Opa1-deficient fibroblasts through Pgs1 improves bioenergetics but not mtDNA depletion.

In order to analyze the functional impact of re-establishing a tubular network on respiration and the oxidative phosphorylation (OXPHOS) system, we measured oxygen consumption rates using Seahorse FluxAnalyzer oxygraphy in intact MEFs depleted of Opa1 and/or Pgs1 (Figure 7A). *Opa1*^{Crispr} MEFs exhibited a modest reduction in basal (Figure 7B) and maximal oxygen consumption rates (Figure 7C) which could be improved upon deletion of Pgs1 in *Opa1*^{Crispr}*Pgs1*^{Crispr} MEFs, implying that rebalancing mitochondrial dynamics positively impacts mitochondrial respiration. Oxygen consumption rate (OCR) measurements performed using Seahorse FluxAnalyzer requires that plated adherent cells be submitted to a brief period of nutrient (glucose, CO_2) deprivation, which has previously been shown to induce mitochondrial hyperfusion[3,12]. To exclude the possibility that nutrient starvation might confound bioenergetic measurements, we performed high resolution respirometry (O2K, Oroboros) on intact, nutrient-replete MEFs in suspension (figure EV7A). *Opa1*^{Crispr} MEFs exhibited reduced oxygen

bioRxiv preprint doi: https://doi.org/10.1101/2021.01.14.426579; this version posted January 15, 2021. The copyright holder for this preprint (which was not certified by peer review) is the author/funder. All rights reserved. No reuse allowed without permission.

532 consumption, which was rescued either by functional complementation with untagged Opa1 or
533 depletion of Pgs1. Interestingly, functional complementation of oxygen consumption and
534 membrane potential defects present in *Opa1*^{Crispr} MEFs was possible only with untagged Opa1
535 and not Opa1-Myc (figure 7EVB, C, EV3D-G) even though both tagged and untagged Opa1
536 constructs were able to restore mitochondrial morphology (figure EV3D, 3E, F). These data
537 further demonstrate that Opa1-dependent bioenergetic functions can be uncoupled from
538 mitochondrial dynamics, in this case using a disruptive C-terminal epitope by the GED domain
539 of the protein[60].
540 Importantly, *Opa1*^{Crispr}*Pgs1*^{Crispr} MEFs exhibited increased basal and maximal oxygen
541 consumption rates relative to the parental *Opa1*^{Crispr} MEFs, which could be lowered back to
542 levels similar to *Opa1*^{Crispr} MEFs by stable re-expression of Pgs1 in *Opa1*^{Crispr}*Pgs1*^{Crispr} MEFs.
543 Pgs1-deficient cells exhibited increased respiration using both Seahorse and Oroboros oxygen
544 consumption assays and was reduced upon re-expression of Pgs1 (Figure 6A-C, figure EV6C).
545 Next, we sought to determine the effects of restored mitochondrial morphology in
546 *Opa1*^{Crispr}*Pgs1*^{Crispr} MEFs on mitochondrial membrane potential. Cells were incubated with the
547 potentiometric dye tetramethylrhodamine ethyl ester (TMRE) to label actively respiring
548 mitochondria. TMRE signal intensity normalized to mitochondrial content (mitoYFP) and was
549 recorded at the single-cell level using confocal fluorescence microscopy (Figure 7D). We
550 observed a reduction in membrane potential in *Opa1*^{Crispr} MEFs that was rescued upon stable
551 re-expression of untagged Opa1 (Figure 7D). *Opa1*^{Crispr}*Pgs1*^{Crispr} MEFs exhibited a higher
552 media membrane potential than *Opa1*^{Crispr} MEFs but lower than that of WT cells measured by
553 microscopy (Figure 7D). Thus, rescuing mitochondrial morphology of *Opa1*^{Crispr} MEFs via Pgs1
554 depletion improves mitochondrial respiration and membrane potential.
555 qPCR measurement of mitochondrial DNA (mtDNA) content using primer pairs targeting
556 different regions of mtDNA revealed a depletion of mtDNA in *Opa1*^{Crispr} MEFs, which was not
557 rescued by Pgs1 depletion by Crispr/Cas9-mediated ablation (*Opa1*^{Crispr}*Pgs1*^{Crispr} MEFs) or

bioRxiv preprint doi: https://doi.org/10.1101/2021.01.14.426579; this version posted January 15, 2021. The copyright holder for this preprint (which was not certified by peer review) is the author/funder. All rights reserved. No reuse allowed without permission.

siRNA depletion (Figure 7E, F). These data demonstrate that mitochondrial fragmentation and mtDNA maintenance defects in Opa1-deficient cells can be uncoupled.

To assess the impact of rebalancing mitochondrial dynamics on the oxidative phosphorylation (OXPHOS) complexes, we measured the levels of structural subunits by Western blot analyses (Figure 7G). *Opa1*^{Crispr} MEFs showed reduced levels of Ndufa9 (Complex I), Sdha (Complex II), Uqcrc2 (Complex III), Cox2 (Complex IV) and Atp5b (Complex V). Additional depletion of *Pgs1* in *Opa1*^{Crispr} *Pgs1*^{Crispr} MEFs could rescue the levels of Sdha, Uqcrc2, and Atp5B, but not of Ndufa9 nor Cox2, which belong to the two respiratory complexes that derive the most structural subunits from mtDNA (Figure 7H). Consistent with elevated membrane potential measured (figure EV4F) and mtDNA content (Figure 7E) in *Pgs1*^{Crispr} cells, we observed an increase in oxygen consumption rates relative to WT MEFs, which could be lowered by functional complementation with re-expression of Pgs1. Altogether, our data demonstrate functional amelioration of OXPHOS and bioenergetic defects in Opa1-deficient cells by depleting Pgs1.

Discussion

In this study, we present a new imaging approach using supervised machine learning to classify mitochondrial morphology of human and mouse fibroblasts according to pre-defined categories representing unopposed fusion and fission. This classification strategy is robust and can reproducibly recognize mitochondrial fragmentation induced either by accelerated fission or blocked fusion resulting from genetic or chemical manipulation without introducing user bias (figure EV1A-C). Importantly, this workflow is highly scalable and robust at all levels, as evidenced by its application to automated, high-throughput phenotypic screens performed in human fibroblasts using the *Mitome* siRNA library(Figure 2A, D). This classification approach is relative and based on ground truths for mitochondrial morphologies generated by siRNA-mediated depletion of known fission or fusion genes, which are measured and applied at each image acquisition experiment. This compensates for the variability in mitochondrial

bioRxiv preprint doi: https://doi.org/10.1101/2021.01.14.426579; this version posted January 15, 2021. The copyright holder for this preprint (which was not certified by peer review) is the author/funder. All rights reserved. No reuse allowed without permission.

584 morphologies generated due to experimental reasons (e.g., cell culture conditions, cell density,
585 gas levels) and intrinsic population heterogeneity. We applied this unbiased strategy to classify
586 mitochondrial morphology in an array of skin fibroblasts derived from patients suffering from
587 Dominant Optic Atrophy plus (DOA+) and discovered that not all pathogenic mutations in *OPA1*
588 trigger mitochondrial fragmentation, despite patients belonging to the same clinical grouping
589 (Table 1). Neither the steady state levels of OPA1 protein in fibroblasts (figure EV2D) nor the
590 clinical manifestation could predict the S545R and R445H GTPase domain mutations to be
591 most phenotypically severe with respect to mitochondrial morphology (Figure 1B, C). While the
592 molecular explanation for this discordance remains unexplained, we posit that additional factors
593 may modulate mitochondrial morphology in patient fibroblasts. Yet to our knowledge no known
594 genetic modifiers of disease genes involved in mitochondrial dynamics, including *OPA1*-related
595 diseases have yet been identified. Within *OPA1*, genotype-phenotype relationships can be
596 loosely established but it is not possible to fully predict clinical outcome for DOA and DOA+
597 patients solely based on the location and nature of pathogenic, mono-allelic variants in *OPA1*.
598 Recently, intra-allelic variants of OPA1 have been documented to modify clinical and
599 biochemical phenotypes in DOA+[71], indicating that genetic modulation of OPA1 and its
600 function(s) is formally possible. Moreover, chemically induced mitochondrial dysfunction in
601 epithelial cells can be buffered by loss of function of other metabolic genes[72], arguing for the
602 existence of genetic modifiers of MD beyond OPA1. To seek out genetic modifiers of
603 mitochondrial morphology, we coupled our mitochondrial morphology imaging and quantification
604 workflow to a bespoke siRNA library targeting the entire mitochondrial proteome (*Mitome*) and
605 identified known and novel genes whose depletion promoted mitochondrial fragmentation
606 (Figure 2B) or hypertubulation (Figure 2C) in control fibroblasts as well as 91 genes whose
607 depletion could rescue mitochondrial fragmentation in *OPA1* mutant patient-derived fibroblasts.
608 As such, these data provide a valuable resource for further investigation of the genetic
609 regulation of mitochondrial dynamics. We discovered that several of the genes capable of

bioRxiv preprint doi: https://doi.org/10.1101/2021.01.14.426579; this version posted January 15, 2021. The copyright holder for this preprint (which was not certified by peer review) is the author/funder. All rights reserved. No reuse allowed without permission.

610 reversing mitochondrial fragmentation in *OPA1* mutant cells with the most severely fragmented
611 mitochondrial network (Figure 2D) also led to hypertubulation in control fibroblasts (Figure 2F),
612 including known components of the mitochondrial fission apparatus (*DNM1L*, *MIEF1*, *MFF*,
613 *SLC25A46*), which demonstrates in patient fibroblasts that imbalanced mitochondrial dynamics
614 can be genetically re-equilibrated, as previously documented in animal models of MD[32–34].
615 *Mitome* screening also identified a cluster of ribosomal genes, whose individual depletion would
616 be predicted to impair protein synthesis. Indeed, we can show that treating human *OPA1*^{S545R}
617 or mouse *Opa1*^{Crispr} fibroblasts with CHX can promote stress-induced mitochondrial hyperfusion
618 (SiMH). SiMH can be promoted by inhibition of transcription (figure EV4H), translation (Figure
619 4F), as well as the induction of ER stress[15,73,74]. We discovered *CALR*, which encodes a highly
620 conserved chaperone protein that resides primarily in the ER involved in ER stress responses to
621 be a suppressor of mitochondrial fragmentation (Table S4, Figure 2F). Finally, we also
622 discovered an array of nuclear-encoded mitochondrial genes that rescued mitochondrial
623 fragmentation but have not previously associated with mitochondrial dynamics. These genes
624 cover various classes of mitochondrial functions including mitochondrial gene expression,
625 oxidative phosphorylation, and amino acid metabolism yet how these genes (Table S4) or
626 processes (figure EV2H, I) influence mitochondrial dynamics is unclear and warrants further
627 investigation. Intriguingly, a substantial proportion of these genes are found to be mutated in
628 inborn errors of metabolism (Table S4), yet the effects on mitochondrial morphology have not
629 yet been explored. Altogether, our results demonstrate that it is possible to apply an unbiased,
630 high throughput imaging approach to identify candidate suppressors of mitochondrial
631 dysfunction in MD patient fibroblasts.

632 We discovered PGS1 depletion could restore mitochondrial morphology to hypomorphic
633 *OPA1* patient-derived fibroblasts and mouse embryonic fibroblasts (MEFs) mutated for *Opa1*.
634 This occurred via a reduction in mitochondrial fission that was independent of both the
635 recruitment of Drp1 to mitochondria (Figure 4A, B) and Oma1-dependent proteolytic processing

bioRxiv preprint doi: https://doi.org/10.1101/2021.01.14.426579; this version posted January 15, 2021. The copyright holder for this preprint (which was not certified by peer review) is the author/funder. All rights reserved. No reuse allowed without permission.

of Opa1, which are key steps in pathological and physiological fission[1]. Similar to Drp1 or Oma1 ablation, Pgs1 depletion can protect from induction of stress-induced fission and fragmentation triggered by chemical agents known to promote Oma1-dependent Opa1 processing and/or Drp1 recruitment, thereby implicating Pgs1 in mitochondrial fission.

The notion that impairing Pgs1 and thus CL biogenesis might rescue mitochondrial morphology defects caused by Opa1 defects seem counterintuitive at first, given existing reports of a requirement of CL on opposing membranes for Opa1-mediated fusion[56]. *Opa1*^{Crispr}*Pgs1*^{Crispr} MEFs exhibit a similar block of inner membrane fusion as *Opa1*^{Crispr} MEFs and it is therefore not possible to assess the contribution of CL for mitochondrial fusion. Nevertheless, several observations exclude CL depletion as a mechanism for restored mitochondrial morphology in hypomorphic Opa1-deficient cells. First, lipidomic analyses of *Opa1*^{Crispr} MEFs revealed a depletion and alteration of CL acyl chain composition, neither of which was restored by additional depletion of either *Pgs1* or *Tamm41* (Figure 5E) even though mitochondrial morphology was restored in these cells. In fact, Tamm41 or Pgs1-depleted *Opa1*^{Crispr} MEFs exhibit even lower steady-state CL levels than *Opa1*^{Crispr} MEFs (Figure 5E) and unaltered CL saturation states (figure EV5C). Second, WT MEFs depleted of either Pgs1 or Tamm41 show reduced CL levels similar to *Opa1*^{Crispr} MEFs but without an induction of mitochondrial fragmentation (Figure 5B, C). Third, inhibition of cardiolipin synthase (Cls1) does not cause mitochondrial fragmentation but rather promotes mitochondrial elongation (Figure 5B)[75]. Fourth, depletion of the CL remodeling enzyme Tafazzin (TAZ1), does not impair mitochondrial fusion nor trigger mitochondrial fragmentation[76]. Finally, the inhibition of fission mediated by Pgs1 depletion can be reversed by additional suppression of Prelid1, which is upstream in the CL biosynthesis pathway (Figure 5A) and is needed to deliver PA to the IMM. Preldi1 inhibition prevents the delivery of PA to the IMM[69], which is normally converted to CDP-DAG and PGP by Tamm41 and Pgs1, respectively[77]. In yeast, the deleterious effect of PA accumulation in the IMM is supported by observations that altered mitochondrial structure in pgs1 mutant cells,

bioRxiv preprint doi: https://doi.org/10.1101/2021.01.14.426579; this version posted January 15, 2021. The copyright holder for this preprint (which was not certified by peer review) is the author/funder. All rights reserved. No reuse allowed without permission.

662 which accumulate PA in the IMM, can be rescued by additional deletion of the Prelid1
663 orthologue Ups1[69]. We therefore propose that the accumulation of PA rather the depletion of
664 CL drives the suppression of mitochondrial morphology defects caused by Opa1 dysfunction.
665 From a functional perspective, restoration of mitochondrial morphology in Opa1-deficient
666 MEFs increased respiration but not cristae dysmorphology, apoptotic sensitivity, CL
667 dysregulation nor mtDNA depletion observed in *Opa1*^{Crispr} MEFs. The programmed cell death
668 response manifested by *Opa1*^{Crispr}*Pgs1*^{Crispr} MEFs was similar to that of *Opa1*^{Crispr} MEFs when
669 treated with apoptotic inducers, indicating the mitochondrial morphology alone does not dictate
670 cell death sensitivity. Disruption of IMM architecture in Opa1 deficiency has recently been
671 linked to the stability of the MICOS complex[52] but whether CL deficiency contributes to cristae
672 dysmorphology in these cells is unclear. Interestingly, the *Mitome* screen in *OPA1*^{S545R}
673 fibroblasts identified *DNAJC4*, *DNACJ11*, and *MTX1*; interactors of the MICOS complex, which
674 is known to facilitate intramitochondrial lipid transport[78]. In yeast, mitochondria lacking pgs1
675 exhibit altered cristae structure, characterised by extremely elongated cristae sheets resembling
676 onion-like structures[69]. However, in MEFs, depletion of *Pgs1*^{Crispr} reduces CL levels without an
677 observable impact on cristae, arguing that CL depletion alone is not sufficient to cause cristae
678 loss in mammalian cells.
679 The notion that balanced mitochondrial dynamics is critical for cellular health arises from
680 the observations that dampening of mitochondrial fission confers physiological benefits in
681 animal models of mitochondrial dysfunction characterized by mitochondrial fragmentation[33,34,79–
682 81] but whether this paradigm is applicable to human disease has never been investigated.
683 However, the relevance of existing genetic targets of mitochondrial fission is limited due to the
684 essential nature of these genes. For Drp1, whole-body ablation of *Dnm1l* in mice causes
685 embryonic lethality and tissue-specific deletion in organs most critically affected in MD is
686 crippling. Moreover, loss of function mutations in *DNM1L* or genes involved in Drp1-dependent
687 fission including *MIEF1*[82], *SLC25A46*[43], *MFF*[44], *GDAP1*[83], and *INF2*[84] all cause severe

bioRxiv preprint doi: https://doi.org/10.1101/2021.01.14.426579; this version posted January 15, 2021. The copyright holder for this preprint (which was not certified by peer review) is the author/funder. All rights reserved. No reuse allowed without permission.

688 neurodegenerative diseases, making them unlikely therapeutic targets. The *Mitome* screen in
689 *OPA1*^{S545R} fibroblasts identified a cluster of cytosolic ribosomal genes, whose individual
690 depletion would be predicted to impair protein synthesis. These findings are consistent with the
691 observation that treatment of *OPA1*^{S545R} patient fibroblasts with the cytosolic protein synthesis
692 inhibitor CHX can suppress mitochondrial fragmentation in both *OPA1*^{S545R} patient-derived
693 fibroblasts (Figure 1F) and hypomorphic *Opa1*^{Crispr} MEFs (figure EV3J), although
694 pharmacological inhibition of global protein synthesis does not represent a viable therapeutic
695 strategy to rescue defects in mitochondrial form and function. PGS1 depletion does not appear
696 to incur cellular dysfunction in vitro, yet future studies are needed to determine the physiological
697 relevance of this gene and whether it will serve as a useful modulator of mitochondrial function
698 in vivo. In the meantime, we believe it worthwhile to consider PGS1 and other genetic modifiers
699 that we have identified using our *Mitome* screening approach when evaluating the genetic and
700 phenotypic landscape of OPA1-related diseases.
701
702

bioRxiv preprint doi: https://doi.org/10.1101/2021.01.14.426579; this version posted January 15, 2021. The copyright holder for this preprint (which was not certified by peer review) is the author/funder. All rights reserved. No reuse allowed without permission.

Materials and Methods

Human Skin Fibroblasts

Primary fibroblast cultures obtained from patients suffering from Dominant Optic Atrophy plus (DOA+) carrying monoallelic mutations in *OPA1* (*OPA1*^{S545R}, *OPA1*^{R445H}, *OPA1*^{Q297X}, *OPA1*^{I432V}, *OPA1*$^{c.2356-1>T}$) and healthy individuals with no signs of optic atrophy (CTL-1, CTL-2, CTL-3), which served as controls, were established as previously described[27,31].

Written, informed consent was obtained from all patients participating in this study. Approval for research was granted by the Ethics Committee of the University Hospital of Angers (Comité de Protection des Personnes CPP Ouest II – Angers, France; Identification number CPP CB 2014/02; Declaration number DC-2011-1467 and Authorization number AC-2012-1507); and the Yorkshire and the Humber - Bradford Leeds Research Ethics Committee (REC reference: 13/YH/0310).

Mouse Embryonic Fibroblasts

Mouse embryonic fibroblasts (MEF) expressing mitochondrially targeted YFP (mitoYFP MEF) were isolated from *Gt(ROSA26)Sor*$^{mitoYFP/+}$ embryos on a C57Bl6/N genetic background at E13.5 and immortalized using a plasmid encoding SV40 large T antigen as previously described[26]. MEFs lacking MiD49/MiD51/Mff generated as previously described[25] were a gift from Dr. Mike Ryan.

Plasmids

Complementary DNA (cDNA) encoding mouse Pgs1 with a C-terminal Myc tag and Opa1 with a C-terminal 9X Myc tag (pclbw-opa1(isoform 1)-myc; a gift from David Chan (Addgene plasmid # 62845)[60] were cloned into pDONR-221 and then pLenti6/Ubc (Invitrogen) using Gateway Technology (Invitrogen). Generation of an Opa1 isoform 1 construct lacking the C-terminal Myc tag was acheived by site directed mutagenesis. MitoTAG constructs pMXs-3XHA-EGFP-

bioRxiv preprint doi: https://doi.org/10.1101/2021.01.14.426579; this version posted January 15, 2021. The copyright holder for this preprint (which was not certified by peer review) is the author/funder. All rights reserved. No reuse allowed without permission.

729 OMP25 (a gift from David Sabatini (Addgene plasmid # 83356) and pMXs-3XMyc-EGFP-
730 OMP25 (a gift from David Sabatini (Addgene plasmid # 83355) were used for mitochondrial
731 immunocapture studies.
732
733 **Cell culture conditions**
734 Human Fibroblasts were cultured in growth media: Dulbecco's modified Eagle's medium
735 (DMEM) containing 4.5g/L D-Glucose, GlutaMAX™ and pyruvate supplemented with 10% Fetal
736 Bovine Serum (FBS) and 50ug/ml penicillin/streptomycin (P/S) in a 5% CO2 atmosphere at
737 37°C. MEFs were cultured in growth media: DMEM containing 4.5g/L D-Glucose, GlutaMAX™
738 and pyruvate supplemented with 5% FBS and 50ug/ml P/S in a 5% CO2 atmosphere at 37°C.
739 Cells were routinely tested for Mycoplasma by PCR.
740
741 **Generation of Opa1-, Pgs1- and Dr1p-deficient MEFs**
742 Genetic disruption of *Opa1*, *Pgs1*, and *Dnm1l* (Drp1) in MEFs was performed via CRISPR-Cas9
743 gene editing. The single-guide RNAs (sgRNAs) were designed using the CRISPR-Cas9 design
744 tool from the Zhang Lab (http://crispr.mit.edu/) and for Exon 4 of *Opa1* (sgRNA: forward: 5'-
745 caccgTGCCAGTTTAGCTCCCGACC-3' and reverse: 5'-aaacGGTCGGGAGCTAAACTGGCAc-
746 3') and ; Exon 2 of *Pgs1* (sgRNA: forward: 5'-caccgTATGTCCCGAGGGTGTACAC-3' and
747 reverse 5'-aaacGTGTACACCCTCGGGACATAc-3'), and Exon 1 of *Dnm1l* (sgRNA: forward: 5'
748 caccgGCAGGACGTCTTCAACACAG-3' and reverse 5'- aaacCTGTGTTGAAGACGTCCTGCc-
749 3'). sgDNA oligonucleotides were annealed and cloned into the BbsI digested pSpCas9(BB)-
750 2A-GFP vector (SpCas9(BB)-2A-GFP (PX458) was a gift from Feng Zhang (Addgene plasmid #
751 48138). MEFs were transfected with 5ug of pSpCas9(BB)-2A-GFP plasmid containing the
752 respective sgRNA using Lipofectamine 3000 (Life Technologies, L3000008). After 24h
753 incubation, GFP positive cells were individually isolated by fluorescence-activated cell sorting.

bioRxiv preprint doi: https://doi.org/10.1101/2021.01.14.426579; this version posted January 15, 2021. The copyright holder for this preprint (which was not certified by peer review) is the author/funder. All rights reserved. No reuse allowed without permission.

754 Clones were expanded and were validated by western blotting, Sanger sequencing, Illumina
755 MiSeq PE300 deep sequencing of PCR amplicons generated using primers in Table S5.
756
757 **Lentiviral and retroviral transductions**
758 Lentiviral particles were generated from the following plasmids: pLenti6/Ubc-Opa1-9xMyc,
759 pLenti6/Ubc-Opa1, pLenti6/Ubc-Pgs1, pMXs-3XHA-EGFP-OMP25, and pMXs-3XMyc-EGFP-
760 OMP25. VSV-G-pseudotyped vectors were produced by transient transfection of 293T cells
761 with a packaging construct, a plasmid producing the VSV-G envelope (pMD.G) and pBA-rev
762 and pHDMH-gpM2 plamids. Culture medium was collected at 24, 48 and 72 h, pooled,
763 concentrated approximately 1000-fold by ultracentrifugation, aliquoted and stored at -80°C until
764 used. Vector titers were determined by FACS cell Sorting on infected HCT116 cells infected
765 with serial dilutions of vector stock. Transduction of MEFs were performed as previously
766 described[17].
767
768 **Mitochondrial morphology imaging**
769 Human Fibroblasts Cells were seeded on CellCarrier-384 or 96well Ultra microplate (Perkin
770 Elmer) and incubated for at least 24 h in growth media. Fibroblasts were fixed with 4% PFA-
771 PBS (w/v) for 15min, permeabilized in 0.1% (v/v) Triton X-100-PBS for 10min and blocked in
772 10% FBS-PBS overnight at 4°C. The following day, permeabilized cells were first stained with
773 the primary antibody anti-TOM40 (diluted 1:1000 in 5% FBS-PBS), washed 3 times with PBS
774 and then incubated with fluorescently coupled secondary antibody Alexa Fluor 488. Nuclei were
775 finally marked with DAPI (1:10,000 in PBS). Images were acquired using the Operetta CLS
776 High-Content Analysis system (Perkin Elmer), with 40x Air/0.6 NA or 63x Water/1.15 NA. Alexa
777 Fluor 488 and DAPI were excited with the 460-490 nm and 355-385 nm LEDs respectively.
778 MEFs Cells were seeded on 96well CellCarrier Ultra imaging plates (Perkin Elmer) 24h before
779 imaging. Nuclei were labeled with NucBlue™ Live ReadyProbes™ Reagent (ThermoFisher

bioRxiv preprint doi: https://doi.org/10.1101/2021.01.14.426579; this version posted January 15, 2021. The copyright holder for this preprint (which was not certified by peer review) is the author/funder. All rights reserved. No reuse allowed without permission.

Scientific). Fluorescent labeling of mitochondria was achieved using Tetramethylrhodamine Ethyl Ester Perchlorate (TMRE) and/or MitoTracker DeepRed at 100nM for 30min at 37°C, 5% CO2 and/or with genetically encoded mitochondrially-targeted YFP (mitoYFP). Spinning disc confocal images were acquired using the Operetta CLS or Opera Phenix High-Content Analysis systems (Perkin Elmer), with 20x Water/1.0 NA, 40x Air/0.6 NA, 40x Water/1.1 NA or 63x Water/1.15 NA. YFP (460-490 nm), TMRE (530-560 nm), MitoTracker DeepRed (615-645nm), mTurquoise2 (435-460 nm) and DAPI (355-385 nm) were excited the appropriate LEDs (Operetta CLS) or lasers (Operetta Phenix). FRAP experiments were performed with a Nikon Ti2E spinning disc microscope 60x Oil objective/NA1.4 equipped with a Photometrics Prime 95b cMOS camera (pixel 11um). Photobleaching was performed with a 405 laser at (35% power, 400 ms dwell time) and image collection proceeded immediately thereafter at 200 ms intervals. Quantification FRAP studies was performed using Fiji (Image J).

SDS-PAGE immunoblot analysis

Cells were lysed in ice-cold RIPA buffer (50 mM Tris–HCl, pH 7.4, 150 mM NaCl, 1%(v/v) Triton X-100, 0.1% SDS, 0.05% sodium deoxycholate, 1 mM EDTA, and complete protease inhibitor cocktail mix (Roche)). After 30 min of incubation on ice, lysates were centrifuged at 16,000 g for 10min at 4°C. Protein quantification of the cleared lysates was performed by Bradford colorimetric assay (Sigma) using a BSA standard curve. Absorption was measurement at 595nm by the microplate reader Infinite M2000 (TECAN). 15 ug of each sample was reduced and negatively charged with 4X Laemmli Buffer (355 mM 2-mercaptoethanol, 62.5 mM Tris-HCl pH 6.8, 10% (v/v) glycerol, 1% (w/v) SDS, 0.005% (v/v) Bromophenol Blue). Samples were heated 5 min at 95°C and separated on 4-20% Mini-PROTEAN® TGX Stain-Free™ Precast gels (Bio-Rad) or on home-made 7% polyacrylamide gel for OPA1 immunodetection. Gels were then transferred to nitrocellulose membranes with Trans-Blot® Turbo™ Transfer system (Bio-Rad). Equal protein amount across membrane lanes were checked by Ponceau S staining or

bioRxiv preprint doi: https://doi.org/10.1101/2021.01.14.426579; this version posted January 15, 2021. The copyright holder for this preprint (which was not certified by peer review) is the author/funder. All rights reserved. No reuse allowed without permission.

Stain-free detection. Membranes were blocked for 1h with 5% (w/v) semi-skimmed dry milk dissolved in Tris-buffered saline Tween 0.1% (TBST), incubated overnight at 4°C with primary antibodies dissolved 1:1,000 in 2% (w/v) Bovine Serum Albumin (BSA), 0.1% TBST. The next day membranes were incubated at least 1h in secondary antibodies conjugated to horseradish peroxidase (HRP) at room temperature (diluted 1:10,000 in 5% milk). Finally, membranes were incubated in Clarity™ Western ECL Substrate (Bio-Rad) for 2min and luminescence was detected using the ChemiDoc® Gel Imaging System. Densitometric analysis of the immunoblots was performed using Image Lab Software (Bio-Rad).

siRNA transfection

Silencing of the indicated genes was performed using forward transfection: 20nM of the specific siRNA was mixed with Lipofectamine RNAiMax (Invitrogen), added on top of seeded cells and left at 37°C in a CO_2 incubator for 72h. Specific and non-targeting siRNAs were obtained from Dharmacon. For mouse siRNA: Negative control NT: D-001210-04-05; *Opa1* siRNA: L-054815-01-0005, *Drp1* siRNA: L-054815-01-0005, *Pgs1* siRNA: L-064480-01-0005, *Tamm41* siRNA: M-056928-01-0005, Ptpmt1 siRNA: M-047887-01-0005, Cls1 siRNA: M-055736-01-0005, Prelid1 siRNA: M-065330-01-0005. For human siRNA: Negative control NT: D-001210-04-05, *PGS1* siRNA: D-009483-02-0002+D-009483-13-0002+ D-009483-01-0002+ D-009483-04-0002; *TAMM41* siRNA: L-016534-02-0005; *DNM1L* siRNA: M-012092-01- 0005: *OPA1* siRNA: M-005273-00- 0005.

RT-qPCR

Total RNA was extracted using TRIzol™ Reagent and chloroform, purified and subjected to DNA digestion using the NucleoSpin RNA kit (MACHEREY-NAGEL). RNA concentration was measured using NanoQuant Plate™ (Infinite M200, TECAN) and 1 ug of total RNA was converted into cDNA using the iScript Reverse Transcription Supermix (Bio-Rad). RT-qPCR

bioRxiv preprint doi: https://doi.org/10.1101/2021.01.14.426579; this version posted January 15, 2021. The copyright holder for this preprint (which was not certified by peer review) is the author/funder. All rights reserved. No reuse allowed without permission.

was performed using the CFX384 Touch Real-Time PCR Detection System (Bio-Rad) and SYBR® Green Master Mix (Bio-Rad) using the primers listed in Table 3. Actin or APP were amplified as internal standards. Data were analyzed according to the 2−ΔΔCT method[85].

Analysis of oxygen consumption rates

Oxygen consumption was measured with the XFe96 Analyzer (Seahorse Biosciences) and High Resolution Respirometry (O2k-Fluorespirometer, Oroboros, AT). For Seahorse experiments, cells (30,000 MEFs or 20,000 human fibroblasts experimentally optimized) were seeded onto 96-well XFe96 cell culture plates. On the following day, cells were washed and incubated with Seahorse XF Base Medium completed on the day of the experiment with 1 mM Pyruvate, 2 mM Glutamine and 10 mM Glucose. Cells were washed with the Seahorse XF Base Medium and incubated for 45min in a 37°C non-CO_2 incubator before starting the assay. Following basal respiration, cells were treated sequentially with: oligomycin 1 µM, CCCP 2 µM and Antimycin A 1 µM + 1 µM Rotenone (Sigma). Measurements were taken over 2-min intervals, proceeded by a 1-min mixing and a 30s incubation. Three measurements were taken for the resting OCR, three for the non-phosphorylating OCR, three for the maximal OCR and three for the extramitochondrial OCR. After measurement, the XFe96 plate was washed with Phosphate-Buffered Saline (PBS) and protein was extracted with RIPA for 10min at room temperature. Protein quantity in each well was then quantified by Bicinchoninic acid assay (BCA). Absorption was measurement at 562 nm by the microplate reader (Infinite M200, TECAN) and used to normalize OCR data.

For O2k respirometry, 2 million intact MEFs were transferred to the 37°C-heated oxygraph chambers containing MiRO5 buffer. Basal respiration was measured first. Then 10 nM oligomycin, 2µM CCCP and 25 µM AntimycinA + 5µM Rotenone was sequentially injected and non-phosphorylating OCR, maximal OCR and extramitochondrial OCR was measured, respectively. Finally, cells were recovered and washed once with PBS. Protein was extracted

bioRxiv preprint doi: https://doi.org/10.1101/2021.01.14.426579; this version posted January 15, 2021. The copyright holder for this preprint (which was not certified by peer review) is the author/funder. All rights reserved. No reuse allowed without permission.

858 with RIPA Buffer for 30min at 4°C and quantified using Bradford assay. Absorption was
859 measurement at 595 nm by the microplate reader (Infinite M200, TECAN) and used to
860 normalize O_2 flux .
861
862 **mtDNA content quantification**
863 Genomic DNA was extracted using the NucleoSpin Tissue (MACHEREY-NAGEL) and
864 quantified with NanoQuant Plate™ (Infinite M200, TECAN). RT-qPCR was performed using the
865 CFX384 Touch Real-Time PCR Detection System (Bio-Rad), 25ng of total DNA and the SYBR®
866 Green Master Mix (Bio-Rad). Actin or APP was amplified as internal standards. Primers
867 sequence are listed in Table 3. Data were analyzed according to the 2−ΔΔCT method[85].
868
869 **Mitochondrial morphology quantification**
870 Harmony Analysis Software (PerkinElmer) was used for automated image analysis as described
871 in detail in Table 3 PhenoLOGIC sequence. Z-projected images first undergo brightfield
872 correction. Nuclei and cellular segmentation were defined using the “Find Nuclei” building block
873 with the HOECHST 33342 channel and the “Find Cytoplasm” building block with the Alexa 488
874 or TMRE (mitochondria) channel. Mitochondrial network was analyzed using SER Texture
875 properties (Ridge, Bright, Edge, Dark, Valley, Spot) and the PhenoLOGIC supervised machine
876 learning algorithm was used to identify the best properties able to segregate the three
877 populations: “Normal”, “Fragmented” and “Hypertubular” network. ~200-400 cells of each
878 control (Normal: WT + DMSO or WT + NT siRNA, Fragmented: WT + CCCP or WT + *OPA1* or
879 *Opa1* siRNA, Hypertubular: WT + CHX or WT + *DNM1L* or *Dnm1l* siRNA) were selected to feed
880 the algorithm for training. Automatic single-cell classification of non-training samples (i.e.
881 unknowns) was carried out by the supervised machine-learning module.
882

bioRxiv preprint doi: https://doi.org/10.1101/2021.01.14.426579; this version posted January 15, 2021. The copyright holder for this preprint (which was not certified by peer review) is the author/funder. All rights reserved. No reuse allowed without permission.

883 **High Content Screening**

884 The siRNA library (*Mitome*; 1531 siRNAs) consists of a Cherrypick SmartPool siRNA library
885 targeting all known and predicted mitochondrial genes based on Mitominer V4 and Mitocarta.
886 500nl of 2 µM siRNAs (20nM final concentration) were distributed on 6 different 384-well
887 imaging plates (CellCarrier Ultra, Perkin Elmer), as described in Table 3, using Echo 550
888 (Labcyte Inc.) and were left to dry under a sterile hood at least for 24 h. For each well, 10 µl of
889 PBS containing 0.1 µl of Lipofectamine RNAiMax was automatically added using the pipetting
890 robot VIAFLO 384 (Integra). After 1h incubation at room temperature (RT), 2000 *OPA1*^{S545R}
891 patient fibroblasts (in 40 µl) were added to each well for reverse transfection using the VIAFLO
892 384 (Integra). Cells were incubated at 37°C, 5% CO2 for 72h and finally immunostained using
893 the automatic pipette VIAFLO 384 (Integra) as described below.
894

Step	Solution	Incubation time and temperature
1-Wash 1x	PBS	No incubation/37°C
2-Fixation	PFA 4%	15min/37°C
3-Wash 3x	PBS	No incubation/RT
4-Permeabilization	0.2% Triton	10min/RT
5-Wash 3x	PBS	No incubation/RT
6-Saturation	10% FBS	Overnight/4°C
7-Primary antibody	anti-TOMM40 (rabbit) 1:1000 in 5%FBS-PBS	Overnight/4°C
8-Wash 3x	PBS	No incubation/RT
9-Secondary antibody	anti-rabbit-Alexa488 1:1000 in 5%FBS-PBS	2h/RT

bioRxiv preprint doi: https://doi.org/10.1101/2021.01.14.426579; this version posted January 15, 2021. The copyright holder for this preprint (which was not certified by peer review) is the author/funder. All rights reserved. No reuse allowed without permission.

10-Wash 3x	PBS	No incubation/RT
11-Nuclei staining	DAPI 1:10,000 in PBS	30min/RT
12-Wash 3x	PBS	No incubation/RT

Images were acquired using the Operetta CLS High-Content Analysis system (Perkin Elmer), with 40x Air/0.6 NA. 9 fields of view with 2 slices (z=-6.5 and -7.5) were captured per well. Alexa 488 and DAPI were excited with the 460-490 nm and 355-385 nm LED respectively. Mitochondrial morphology was automatically quantified using the Harmony Analysis Software (PerkinElmer) as described in details in Table 3 PhenoLOGIC sequence. A brightfield correction (fixed, string) was applied to all Z-projected images. Nuclei and cells were first segmented using the “Find Nuclei” building block on the DAPI channel and the “Find Cytoplasm” building block on the Alexa 488 channel. SER Texture analysis (Ridge, Bright, Edge, Dark, Valley, Spot) of the mitochondrial network was then calculated. The PhenoLOGIC supervised machine learning module of Harmony (available through the “Select Population-Linear Classifier” building block) was used to identify the most relevant SER textures able to segregate the three populations (*fragmented*: *OPA1*^{S545R} + NT siRNA, *hyperfragmented*: *OPA1*^{S545R} + *OPA1* siRNA and rescued: *OPA1*^{S545R} + *DNM1L* siRNA mitochondrial morphologies). For training, ~800 cells per training class (ground truth) of mitochondrial morphologies were manually selected in each control well of each plate. The supervised machine-learning algorithm is then able to classify mitochondrial morphology of each well into those three categories. To evaluate the quality of the screening, we calculated the Z-score of each plate using the following formula: $\mathrm{Z-score} = 1 - \frac{3(\sigma_p + \sigma_n)}{|\mu_p - \mu_n|}$ where μ_p and σ_p are the mean and standard deviation values of the positive control p (rescued morphology: *OPA1*^{S545R} patient fibroblasts + *DNM1L* siRNA) and μ_n and σ_n those of the negative control n (fragmented morphology: *OPA1*^{S545R} patient fibroblasts + NT siRNA). The

bioRxiv preprint doi: https://doi.org/10.1101/2021.01.14.426579; this version posted January 15, 2021. The copyright holder for this preprint (which was not certified by peer review) is the author/funder. All rights reserved. No reuse allowed without permission.

Z-score of all plates were above 0.5 reflecting the robustness of the screening (Plate1=0.82, Plate2=0.55, Plate3=0.80, Plate4=0.79, Plate5=0.80, Plate6=0.70).

In order to define a threshold of phenotypic rescue of mitochondrial morphology, we designed and deployed a univariate 3-components statistical model using R (https://www.R-project.org) to define the siRNAs able to re-establish mitochondrial morphology to same extent as with DRP1 siRNA. We used two models, one designed to identify *hypertubular* hits data and another to identify *hyperfragmented* hits among the *Mitome* library siRNA pools. Each model has 3 components. For the rescued threshold in *OPA1*^{S545R} siRNA Mitome screen, these are the *OPA1*^{S545R} NT siRNA (negative control), the *OPA1*^{S545R} *DNM1L* siRNA (positive control for rescued morphology) and the *OPA1*^{S545R} cells transfected with the 1531 siRNAs of the *Mitome* library. For the hyperfragmented threshold in *OPA1*^{S545R} siRNA Mitome screen, these are the *OPA1*^{S545R} NT siRNA (negative control), the *OPA1*^{S545R} *OPA1* siRNA (positive control for hyperfragmented morphology) and the *OPA1*^{S545R} cells transfected with the 1531 siRNAs of the Mitome library.

Membrane potential measurement

Membrane potential was determined by FACS and live confocal microscopy. For FACS analyses, 1x10^6 MEFs or human fibroblasts were plated in 10 cm^2 dishes and incubated 24h with growth media. The next day, cells were treated with 100nM TMRE for 20 min at 37°C, 5% CO_2 or with 20 µM Carbonyl Cyanide m-chlorophenyl hydrazine (CCCP) for 30min followed by 30min incubation with 100 nM TMRE + 20 µM CCCP for 20 min at 37°C, 5% CO_2. Cells were washed with PBS, dissociated from the dish with 0.05% Trypsin (ThermoFisher Scientific) and centrifuged 5 min at 2000 g. The cell pellet was then suspended in PBS containing SYTOX™ Blue Dead Cell Stain (diluted 1:5000). The single cell fluorescence was measured using the CytoFLEX flow cytometer (Beckman Coulter). Dead cells (SYTOX™ Blue positive cells) were detected with the channel PB450 (450/45 BP) and discarded from analysis. TMRE positive cells

bioRxiv preprint doi: https://doi.org/10.1101/2021.01.14.426579; this version posted January 15, 2021. The copyright holder for this preprint (which was not certified by peer review) is the author/funder. All rights reserved. No reuse allowed without permission.

were detected with the PE channel (585/42 BP) and the median of TMRE intensity was used for analysis. For MEFs expressing mitoYFP, YFP signal was detected using the channel FITC (525/40 BP) and compensation between FITC and PE channels was manually calculated.
For confocal microscopy, the genetically encoded mitochondrially-targeted YFP MEFs were seeded in 96well CellCarrier Ultra imaging plates (Perkin Elmer) one day before the measurement. The next day, Nuclei were labeled with NucBlue™ Live ReadyProbes™ Reagent (ThermoFisher Scientific) and cells were treated with 100 nM TMRE for 20 min at 37°C, 5% CO_2 or with 20 µM Carbonyl Cyanide m-chlorophenyl hydrazine (CCCP) for 30 min followed by 30 min incubation with 100 nM TMRE + 20 µM CCCP for 20 min at 37°C, 5% CO_2. Spinning disc confocal images were acquired using the Operetta CLS High-Content microscope (Perkin Elmer) with 40x Air/0.6 NA. YFP, TMRE and NucBlue were excited with the 460-490 nm, 530-560 nm and 355-385 nm LEDs respectively. TMRE and YFP signal per cell was quantified using the Harmony Analysis Software (PerkinElmer).

Cell death assay

MEFs were plated in 96- or 384-well imaging plates (CellCarrier Ultra, Perkin Elmer) and incubated at least one day at 37°C, 5% CO_2. The day of experiment, cells were incubated with NucBlue™ Live ReadyProbes™ Reagent (ThermoFisher Scientific) and Propidium Iodide (PI, Sigma) and treated either with 4µM Actinomycin D + 10 µM ABT-737 ± 20µM qVD or 0.5 µM Staurosporine ± 20 µM or 16 µM etoposide ± 20 µM qVD for the indicated time. Total cells (stained by NucBlue) and dead cells (stained by PI+) were imaged every hour for the indicated time with the Operetta CLS High-Content microscope (Perkin Elmer) at 40x Air/0.6 NA. PI and NucBlue were excited with the 530-560 nm and 355-385 nm LEDs respectively. PI+/total cells over time were quantified with using the Harmony Analysis Software (PerkinElmer).

Stress-induced mitochondrial fission and fusion imaging

bioRxiv preprint doi: https://doi.org/10.1101/2021.01.14.426579; this version posted January 15, 2021. The copyright holder for this preprint (which was not certified by peer review) is the author/funder. All rights reserved. No reuse allowed without permission.

2000 MEFs expressing mitoYFP were plated in 384-well and incubated 24h at 37°C, 5% CO_2. The day of experiment, nuclei were labeled with NucBlue™ Live ReadyProbes™ Reagent (ThermoFisher Scientific) for 30 min at 37°C, 5% CO2. For stress-induced fission imaging, cells were treated with 5 µM CCCP or 16 µM 4Br-A23187 for the indicated time. For stress-induced hyperfusion imaging, cells were treated with 10 µM CHX or 0.5 µM ActD. Nuclei (NucBlue) and Mitochondria (YFP) were imaged every hour for the indicated time using the Operetta CLS High-Content microscope (Perkin Elmer) at 40x Air/0.6 NA. YFP and NucBlue were excited with the 460-490 nm and 355-385 nm LEDs respectively. Finally, mitochondrial morphology was quantified as described in the "Mitochondrial morphology quantification" section.

DRP1 mitochondrial recruitment assay

2000 MEFs expressing mito-YFP were plated in 384 well and incubated 24h at 37°C, 5% CO2. Cells were then fixed for 10min with 37°C -prewarmed 4% paraformaldehyde in PHEM Buffer (60mM PIPES, 25mM HEPES, 10mM EGTA, 2mM MgCl2, pH 7.3), permeabilized for 10min with 0.1% Triton X-100 in PBS and blocked overnight at 4°C with 10% FBS in PBS. Mitochondria were stained overnight at 4°C with α-TOMM40 (diluted 1:1000; Proteintech #18409-1-AP) primary antibody and Drp1 with α-DLP1 primary antibody (diluted 1:1000, BD # 611112). Cells were incubated with anti-rabbit Alexa 568 (1:1000; goat anti-rabbit IgG Alexa Fluor 568; Invitrogen #A11011) and anti-mouse Alexa A647 (1:1000; goat anti-mouse IgG Alexa Fluor 647; Invitrogen #A21236) for 2h at RT. Finally, Nuclei were stained for 30min at RT with Hoechst 33342 diluted 1:10.000 in PBS. Images were acquired using the Operetta CLS High-Content Analysis system (Perkin Elmer), with 63x Water/1.15 NA. 5 fields of view with 3 slices (z=0, 0.5 and 1) were captured per well. Alexa 647, Alexa 568 and Hoechst were excited with the 615-645 nm, 530-560 nm and 355-385 nm LED respectively. Colocalization of Drp1 and Tom40 was evaluated using the Harmony Analysis Software (PerkinElmer) as described in detail in Table S1.

bioRxiv preprint doi: https://doi.org/10.1101/2021.01.14.426579; this version posted January 15, 2021. The copyright holder for this preprint (which was not certified by peer review) is the author/funder. All rights reserved. No reuse allowed without permission.

994

995 **Mitochondrial isolation**

996 Mitochondria were isolated as previously published[86]. In brief, MEFs were infected with retroviral
997 particles containing pMXs-3XHA-EGFP-OMP25, selected with 10ug/ml Blasticidin and the
998 expression of HA-tag was verified by SDS-PAGE. The day of experiment, ~ 30 million MEFs
999 were collected, washed with KPBS buffer (136 mM KCl and 10 mM KH_2PO_4, pH 7.25), and
1000 homogenized with 25 stokes of the plunger at 1000 rpm at 4°C. Nuclei and debris were discard
1001 by centrifugation at 1000g for 2min at 4°C. The supernatant was collected and subjected to
1002 immunocapture with prewashed anti-HA magnetic beads for 30min on end-over-end rotator 4°C.
1003 The beads were then washed 3 times and resuspended in 500ul KPBS. 30% of the suspension
1004 beads was set aside and used for immunoblotting. The remaining beads were store at -150°C
1005 for the indicated analysis.

1006

1007 **Transmission electron microscopy**

1008 Cells were grown on sapphire discs of 3 mm diameter (Engineering Office M. Wohlwend GmbH,
1009 Switzerland) previously coated with a carbon film[87] and frozen with a Leica ICE high pressure
1010 freezer machine (Leica microsystems, Austria) with foetal calf serum as cryoprotectant. The
1011 freeze substitution was done in a Leica AFS2 machine in dry acetone containing 1%
1012 osmiumtetroxide, 0.1% uranylacetate, and 5% water as previously published[88]. Samples were
1013 gradually infiltrated at RT with epoxy resin and after heat polymerization the sapphire discs were
1014 removed from the plastic block. Sections with a thickness of 70 nm were cut with a Leica UCT
1015 microtome and collected on carbon, formvar coated copper grids. Sections were contrasted with
1016 4% aqueous uranylacetate and Reynold's lead citrate. Generation of ultra-large high-resolution
1017 electron microscopy maps were acquired using a TECNAI F20 transmission electron
1018 microscope (FEI) with a field emission gun (FEG) as an electron source, operated at 200kV,

bioRxiv preprint doi: https://doi.org/10.1101/2021.01.14.426579; this version posted January 15, 2021. The copyright holder for this preprint (which was not certified by peer review) is the author/funder. All rights reserved. No reuse allowed without permission.

and equipped with a GATAN Ultrascan US4000 CCD camera. The SerialEM software [89,90] was used for multi-scale mapping as follows: Initially a full grid map was acquired at 190x magnification (pixel size = 551.75 nm). Middle magnification maps at 2500x (pixel size = 35.98 nm) were acquired in areas with cells. Finally, high magnification maps (14500x, pixel size = 6.194 nm) were collected at areas of interest, usually covering large part of the cellular cytoplasm (maps consisted of 100 - 300 micrographs/pieces) were many mitochondria were observed. Stacks of montages were displayed using the *3dmod* interface of IMOD[91]. The initial piece coordinates for each micrograph are either saved at the header of the mrc stack file by SerialEM, or in case of very large montages, at the additional metadata file mdoc. The 'Align Serial Sections/Blend Montages' interface of IMOD[92] was used for blending the stack of micrographs to a single large image by calling the blendmont function of IMOD. Quantification of cristae number and OMM/IMM perimeter was performed using ImageJ[93].

Quantitative mass spectrometry of lipids

Mass spectrometric analysis was performed essentially as described[94,95]. All internal standards were purchased from Avanti Polar lipid. Lipids were extracted from isolated pure mitochondria or whole cell pellet in the presence of internal standards of major phospholipids (PC 17:0-20:4, PE 17:0-20:4, PI 17:0-20:4, PS 17:0-20:4, PG 17:0-20:4, PA 15:0-18:1-d7 and CL mix I), cholesterol (cholesterol-d7), cholesterylesters (19:0 cholesterol ester) and TAG (D5 TAG mix I). Extraction was performed using automated liquid handling robot (CyBio FeliX, Analytik Jena) according to Bligh and Dyer with modifications. Briefly, 7.5 µg mitochondria or 1 x 10^5 cells in 80 µL water and internal standards (22, 17, 8.8, 6.5, 2.5, 3.0, 8, 10, 8.5 and 4 pmole of PC 17:0-20:4, PE 17:0-20:4, PI 17:0-20:4, PS 17:0-20:4, PG 17:0-20:4, PA 15:0-18:1-d7, CLs, cholesterol-d7, 19:0 cholesterol ester and TAGs, respectively) mixed with 0.3 mL of chloroform/methanol [1:2 (v/v)] for 10 min. After addition of 0.1 mL chloroform and of 0.1 mL H_2O, the sample was mixed again for 10 min, and phase separation was induced by

bioRxiv preprint doi: https://doi.org/10.1101/2021.01.14.426579; this version posted January 15, 2021. The copyright holder for this preprint (which was not certified by peer review) is the author/funder. All rights reserved. No reuse allowed without permission.

centrifugation (800 xg, 2 min). The lower chloroform phase was carefully transferred to a clean glass vial. 20 µl of the neutral lipid extract was taken to a glass vial, dried and incubated in acetylchoride/chloroform (1:5) for 2 h at 25 °C under hume hood for chemical derivatization. The upper water phase was mixed with 20 µL 165mM HCl and 100 µL chloroform for 10 min. After phase separation, the lower chloroform phase was carefully transferred to the glass vial with the rest of chloroform phase from the first extraction. The solvent was evaporated by a gentle stream of argon at 37°C. Lipids were dissolved in 10 mM ammonium acetate in methanol, transferred to Twin.tec PCR plate sealed with Thermowell sealing tape and analyzed on a QTRAP 6500 triple quadrupole mass spectrometer (SCIEX) equipped with nano-infusion splay device (TriVersa NanoMate with ESI-Chip type A, Advion).

bioRxiv preprint doi: https://doi.org/10.1101/2021.01.14.426579; this version posted January 15, 2021. The copyright holder for this preprint (which was not certified by peer review) is the author/funder. All rights reserved. No reuse allowed without permission.

Figure Legends

Figure 1: Inhibition of mitochondrial division prevents mitochondrial fragmentation caused by OPA1 deficiency in DOA+ patient-derived fibroblasts

(A) Schematic of supervised machine learning (ML) mitochondrial morphology imaging and quantification pipeline. Fibroblasts plated in 384 well plates are stained for mitochondria (anti-TOM40, green), nuclei (DAPI, blue), and cell body (CellMask, blue). Supervised ML training performed on cells with fragmented (*OPA1* or *YME1L* siRNA), normal (non-targeting NT siRNA), and hypertubular (*DNM1L* siRNA) mitochondria. Automatic single-cell trinary classification of control (CTL1, 2, 3) and $OPA1^{S545R}$ patient fibroblasts by supervised ML.

(B) Representative confocal images of control (CTL1, 2, 3) and DOA+ patient fibroblasts carrying indicated monoallelic mutations imaged as described in A. Scale bar=20μm.

(C) Mitochondrial morphology quantification of B. Data represent mean ± SD of two independent experiments, (195-2496 cells per cell line), One-way ANOVA.

(D) Representative confocal images of control (CTL1) and $OPA1^{S545R}$ patient fibroblasts treated with *OPA1*, *DNM1L*, or non-targeting (NT) siRNAs for 72 hours and imaged as described in A. Scale bar=20μm.

(E) Mitochondrial morphology quantification of D. Data represent mean ± SD of three independent experiments, (3219-5857 cells per cell line), One-way ANOVA.

(F) Representative confocal images of control (CTL1) and $OPA1^{S545R}$ patient fibroblasts treated with 50μM cycloheximide (CHX) where indicated for 6 hours. Imaging as described in A. Scale bar=20μm

(G) Mitochondrial morphology quantification of F. Data represent mean ± SD of two independent experiments, (879-4154 cells per cell line), One-way ANOVA.

Figure 2: High throughput screening identifies known and novel genetic modifiers of mitochondrial morphology in control and DOA+ patient-derived fibroblasts

bioRxiv preprint doi: https://doi.org/10.1101/2021.01.14.426579; this version posted January 15, 2021. The copyright holder for this preprint (which was not certified by peer review) is the author/funder. All rights reserved. No reuse allowed without permission.

(A) Schematic of *Mitome* siRNA imaging screen for mitochondrial morphology in control human fibroblasts. Fibroblasts were reverse-transfected with siRNAs directed against 1531 nuclear-encoded mitochondrial genes in 384 well plates and stained for mitochondria (anti-TOM40, green), nuclei (DAPI, blue), and cytoplasm (CellMask, blue). Supervised ML training performed on control fibroblasts treated with siRNAs for *OPA1* or *YME1L* (fragmented) NT control (normal), and *DNM1L* (hypertubular) were applied to single-cell trinary classification of *Mitome* siRNA treated fibroblasts.

(B) Candidate siRNAs (purple) causing mitochondrial fragmentation relative to grounds truths for fragmentation (*OPA1* siRNA). Violin plot representing % fragmented morphology of *Mitome* siRNAs (purple). Hits were selected with a univariate 3-components statistical model programmed in R using ground truths for morphology show in (A). The defined threshold for positive hits was 68.9% and identified 22 candidate genes, including *OPA1*, *YME1L*, and *AMBRA1*.

(C) Candidate siRNAs (purple) causing mitochondrial hypertubulation relative to grounds truths for hypertubulation (*DNM1L* siRNA). Violin plot representing % hypertubular morphology of *Mitome* siRNAs (purple). Hits were selected with a univariate 3-components statistical model programmed in R using ground truths for morphology show in (A). The defined threshold for positive hits was 69.2% and identified 145 candidate genes, including *DNM1L*, *MIEF1,* and *PGS1.*

(D) Schematic of *Mitome* siRNA imaging screen in $OPA1^{S545R}$ patient fibroblasts. Fibroblasts transfection and imaging as described in A. Supervised ML training performed on $OPA1^{S545R}$ fibroblasts treated with siRNA for *OPA1* (hyperfragmented) NT control (normal), and *DNM1L* (rescued) were applied to single-cell trinary classification of $OPA1^{S545R}$ patient fibroblasts.

(E) Violin plot representing % rescued morphology of *Mitome* siRNAs. The siRNA able to rescue mitochondrial fragmentation were selected with a univariate 3-components statistical model programmed in R using the following ground truths for morphology: fragmented (NT siRNA),

bioRxiv preprint doi: https://doi.org/10.1101/2021.01.14.426579; this version posted January 15, 2021. The copyright holder for this preprint (which was not certified by peer review) is the author/funder. All rights reserved. No reuse allowed without permission.

rescued (*DNM1L* siRNA), and hyperfragmented (*OPA1* siRNA). The defined threshold for positive rescued hits was 49.81% and identified 91 candidate genes. **(E)** Overlap between 91 candidates identified in (E) and (C) identify 38 overlapping genes leading to mitochondrial elongation (*hypertubulation* in CTL-1, CTL-2 and *rescued* in $OPA1^{S545R}$ fibroblasts) and 53 genes that specifically rescue mitochondrial fragmentation in $OPA1^{S545R}$ fibroblasts.

Figure 3: PGS1 depletion rescues mitochondrial fragmentation in OPA1-deficient human and mouse fibroblasts

(A) Representative confocal images of control (CTL-1) and $OPA1^{S545R}$ patient fibroblasts treated with *OPA1*, *DNM1L*, *PGS1*, and non-targeting (NT) siRNAs or indicated combinations for 72 hours. Mitochondria (anti-TOM40, green) and nuclei (DAPI, blue). Scale bar=20μm.

(B) Mitochondrial morphology quantification of (A) using control fibroblasts with fragmented (*OPA1* siRNA), normal (non-targeting NT siRNA), and hypertubular (*DNM1L* siRNA) mitochondria. Data represent mean ± SD of three independent experiments, One-way ANOVA (905-3695 cells per cell line), (% fragmented).

(C) Representative confocal images of wild type (WT) and $OPA1^{Crispr}$ MEFs treated with NT or *Pgs1* siRNA for 72 hours. Live imaging of mitochondria (mitoYFP, green) and nuclei (NucBlue, blue). Scale bar=10μm.

(D) Mitochondrial morphology quantification of (C) using WT MEFs treated with *Opa1* siRNA (fragmented), NT siRNA (normal), or *Dnm1l* siRNA (hypertubular) ground truth training sets. Data represent mean ± SD of three independent experiments, One-way ANOVA (6613-8758 cells per cell line), (% fragmented).

(E) Representative confocal images of WT, $Opa1^{Crispr}$ MEFs complemented with pLenti-Opa1, $Opa1^{Crispr}Pgs1^{Crispr}$ MEFs and $Pgs1^{Crispr}$ MEFs complemented with pLenti-Pgs1 by lentiviral delivery. Live imaging of mitochondria (mitoYFP, green) and nuclei (NucBlue, blue). Scale bar=10μm.

bioRxiv preprint doi: https://doi.org/10.1101/2021.01.14.426579; this version posted January 15, 2021. The copyright holder for this preprint (which was not certified by peer review) is the author/funder. All rights reserved. No reuse allowed without permission.

(F) Supervised ML mitochondrial morphology quantification of (E) using WT MEFs treated with *Opa1* siRNA (fragmented), NT siRNA (normal), or *Dnm1l* siRNA (hypertubular) training sets. Data represent mean ± SD of three independent experiments, One-way ANOVA (691-3990 cells per cell line), (% fragmented).

(H) Equal amounts of protein extracted from MEFs were separated by SDS-PAGE, immunoblotted with anti-OPA1 antibody, and quantified **(I)** by densitometry relative to Stain-Free. Data represent mean ± SD of three independent experiments, One-way ANOVA.

Figure 4: Pgs1 depletion rescues mitochondrial fragmentation by inhibiting mitochondrial fission.

(A) Equal amounts of protein extracted from total (T), cytosolic flow-through (C) and mitochondrial eluate (M) from MEFs of the indicated genotypes stably expressing MitoTag (pMX-OMP25-GFP-HA) obtained following mitochondrial immunocapture were separated by SDS-PAGE, immunoblotted with indicated antibody and quantified by densitometry. Data represent mean ± SD of three independent experiments, One-way ANOVA.

(B) Representative confocal images of MEFs of the indicated genotypes showing subcellular Drp1 distribution. Mitochondria (mitoYFP, green), Drp1 labelled with anti-Drp1 antibody (red) and nuclei (NucBlue, blue). Scale bar=10μm. *MiD49/51/Mff* KO MEFs lack all 3 Drp1 receptors (MiD49, MiD51, and Mff). Bar graph representation of Drp1 localized to mitochondria (green) vs cytosol (blue). Data represent mean ± SD of three independent experiments, (884-3116 cells per cell line), unpaired t-test.

(C) Representative confocal images of live cell imaging of MEFs of the indicated genotypes subjected fragmentation with 5μM CCCP for the indicated time points. Images were captured every hour for 18 hours. Scale bar=10μm.

(D) Supervised ML mitochondrial morphology quantification using WT MEFs treated with 5μM CCCP for 18h (fragmented), untreated (normal), or treated with 10μM CHX for 9h (hypertubular)

bioRxiv preprint doi: https://doi.org/10.1101/2021.01.14.426579; this version posted January 15, 2021. The copyright holder for this preprint (which was not certified by peer review) is the author/funder. All rights reserved. No reuse allowed without permission.

training sets. Data represent mean ± SD of three independent experiments, (131-426 cells per cell line), One-way ANOVA.

(E) FRAP fusion assay in MEFs of the indicated genotype (see Supplemental Movies 1-3). Quantification of mitoYFP signal intensity measured at 200 ms intervals in the photobleached area (green box) for the indicated time (seconds). Data represent mean ± SEM of two independent experiments (n=18-52 cells per genotype), One-way ANOVA.

(F) Representative confocal images of live cell imaging of MEFs of the indicated genotypes subjected hyperfusion (SiMH) with 10μM CHX for the indicated time points. Images were captured every hour for 9 hours.

(G) Mitochondrial morphology quantification of using WT MEFs treated with 5μM CCCP for 18h (fragmented), untreated (normal), or treated with 10μM CHX for 9h (hypertubular) training sets. Data represent mean ± SD of four independent experiments, (155-745 cells per cell line), One-way ANOVA.

Figure 5: Interfering with the cardiolipin synthesis pathway can prevent mitochondrial fragmentation in Opa1 deficient fibroblasts

(A) Schematic of cardiolipin (CL) biosynthesis pathway in mitochondria. Phosphatidic acid (PA) is transported to the inner membrane by PRELID1 where it is converted to CDP-diacylglycerol (CDP-DAG) and glycerol 3-phosphate (G3P) by TAMM41. Phosphatidylglycerol phosphate (PGP) is dephosphorylated to phosphatidylglycerol (PG) by PTPMT1. PG is either degraded to DAG or reacts with CDP-DAG to form CL in a reaction catalyzed by cardiolipin synthase (CLS1). Tafazzin (TAZ) catalyzes the remodeling of monolysocardiolipin (MLCL) to mature CL. CL is transported to the outer membrane and converted to PA by mitoPLD. PA is converted to DAG by Lipin1. PA can be supplied to the inner membrane from DAG conversion by Acylglycerol Kinase (AGK).

bioRxiv preprint doi: https://doi.org/10.1101/2021.01.14.426579; this version posted January 15, 2021. The copyright holder for this preprint (which was not certified by peer review) is the author/funder. All rights reserved. No reuse allowed without permission.

(B) Representative confocal micrographs of MEFs WT and *Opa1*^{Crispr} MEFs treated with indicated siRNAs for 72 hours. Mitochondria (anti-TOM40, green) and nuclei (DAPI, blue). Scale bar=10µm.

(C) Supervised ML mitochondrial morphology quantification of (B) using WT MEFs with fragmented (*Opa1* siRNA), normal (non-targetting NT siRNA), and hypertubular (*Dnm1l* siRNA) mitochondria. Data represent mean ± SD of three independent experiments, One-way ANOVA (726-4236 cells per cell line), (% fragmented).

(D) quantitative RT-PCR (qRT-PCR) measurement of *Prelid1*, *Tamm41*, *Pgs1*, *Ptpmt1*, and *Cls1* expression in *Opa1*^{Crispr} and WT MEFs. Fold change is indicated relative to WT control. Data represent mean ± SD of three independent experiments, One-way ANOVA.

(E) Whole cell phospholipidome of WT and *Opa1*^{Crispr} MEFs treated with NT (non-targeting), Tamm41 or Pgs1 siRNAs. Data represent mean ± SD of four independent experiments.

(F) Representative confocal micrographs of MEFs WT, *Pgs1*^{Crispr} and *Dnm1l*^{Crispr} MEFs treated with indicated siRNAs for 72 hours. Mitochondria (anti-TOM40, green) and nuclei (DAPI, blue). Scale bar=10µm.

(G) Supervised ML mitochondrial morphology quantification of (G) using WT MEFs with fragmented (*Opa1* siRNA), normal (non-targetting NT siRNA), and hypertubular (*Dnm1l* siRNA) mitochondria. Data represent mean ± SD of >3 independent experiments, (3096-7238 cells per cell line), One-way ANOVA (% fragmented).

Figure 6: Pgs1 depletion does not rescue apoptotic sensitivity nor cristae structure in Opa1-deficient MEFs.

(A, B) (Top) MEFs of the indicated genotypes were subjected to 4µM Actinomycin D and 10µM ABT-737 in the presence or absence of the pan-caspase inhibitor qVD. Dead cells (PI+ nuclei, orange) and total cells (NucBlue, blue) were imaged every hour for 25 hours. PI+ nuclei number divided by the total nuclei number was then quantified over time. (Bottom) Representative

bioRxiv preprint doi: https://doi.org/10.1101/2021.01.14.426579; this version posted January 15, 2021. The copyright holder for this preprint (which was not certified by peer review) is the author/funder. All rights reserved. No reuse allowed without permission.

confocal images of (Top). Scale bar=100µm. Data represent mean ± SD of four independent experiments, (1380-2157 cells per cell line), One-way ANOVA.

(C) Representative transmission electron micrographs of MEFs of the indicated genotypes showing loss of lamellar cristae in *Opa1*^{Crispr} and *Opa1*^{Crispr}*Pgs1*^{Crispr} MEFs.

(D) Quantification of (C) of mitochondrial ultrastructure; outer membrane/inner membrane ration (OMM/IMM) and cristae number per mitochondrion. Violin plot of >50 mitochondria per cell line, One-way ANOVA.

Figure 7: Pgs1 depletion enhances respiration in wild type and Opa1-deficient MEFs.

(A) Mitochondrial respiration measured in adherent MEFs of the indicated genotypes using Seahorse FluxAnalyzer. Oxygen consumption rate (OCR) normalized to protein concentration. Following basal respiration, cells were treated sequentially with 1µM Oligomycin (Omy), 2µM CCCP, Antimycin A 1µM + 1µM Rotenone. Bar graphs of (A) representing basal **(B)** and maximum **(C)** respiration. Data represent mean ± SEM of 6-12 independent OCR measurements, One-way ANOVA.

(D) Mitochondrial membrane potential measured by fluorescence microscopy in WT, *Opa1*^{Crispr}, *Opa1*^{Crispr} + pLenti-Opa1, *Opa1*^{Crispr}*Pgs1*^{Crispr}, *Opa1*^{Crispr}*Pgs1*^{Crispr} + pLenti-Pgs1, and *Pgs1*^{Crispr} MEFs + pLenti-Pgs1. Membrane potential is represented as the ratio between TMRE/mitoYFP. WT MEFs treated with 20µM CCCP serve as a negative control for TMRE. Number of analyzed cells indicated in inset.

(E) mtDNA content in MEFs from (F) was quantified by amplification of *MTTL2*, *16S* and *ND1* genes relative to the *GAPDH* nuclear gene in MEFs. Data represent mean ± SD of three independent experiments, One-way ANOVA.

(F) mtDNA content in WT and mutant MEFs treated with indicated siRNAs for 72 hours was quantified by amplification of *MTTL2*, *16S* and *ND1* genes relative to the *GAPDH* nuclear gene in MEFs. Data represent mean ± SD of three independent experiments, One-way ANOVA.

bioRxiv preprint doi: https://doi.org/10.1101/2021.01.14.426579; this version posted January 15, 2021. The copyright holder for this preprint (which was not certified by peer review) is the author/funder. All rights reserved. No reuse allowed without permission.

(G) Equal amounts of protein extracted from WT and mutant MEFs were separated by SDS-PAGE, immunoblotted with indicated antibodies and quantified by densitometry **(H)**. Data represent mean ± SD of three independent experiments, One-way ANOVA.

Table 1: Clinical features of DOA+ patients

Description of clinical features of Dominant Optic Atrophy plus (DOA+) patients from which fibroblasts were derived.

References

1. Giacomello, M., Pyakurel, A., Glytsou, C. & Scorrano, L. The cell biology of mitochondrial membrane dynamics. *Nat. Rev. Mol. Cell Biol.* (2020) doi:10.1038/s41580-020-0210-7.
2. Friedman, J. R. *et al.* ER Tubules Mark Sites of Mitochondrial Division. *Science* **334**, 358–362 (2011).
3. Khacho, M. *et al.* Acidosis overrides oxygen deprivation to maintain mitochondrial function and cell survival. *Nat. Commun.* **5**, 3550 (2014).
4. Choi, S.-Y. *et al.* A common lipid links Mfn-mediated mitochondrial fusion and SNARE-regulated exocytosis. *Nat. Cell Biol.* **8**, 1255–1262 (2006).
5. Chen, H. *et al.* Mitofusins Mfn1 and Mfn2 coordinately regulate mitochondrial fusion and are essential for embryonic development. *J. Cell Biol.* **160**, 189–200 (2003).
6. Olichon, A. *et al.* Loss of OPA1 perturbates the mitochondrial inner membrane structure and integrity, leading to cytochrome c release and apoptosis. *J. Biol. Chem.* **278**, 7743–7746 (2003).
7. Cipolat, S., Martins de Brito, O., Dal Zilio, B. & Scorrano, L. OPA1 requires mitofusin 1 to promote mitochondrial fusion. *Proc. Natl. Acad. Sci. U. S. A.* **101**, 15927–15932 (2004).

bioRxiv preprint doi: https://doi.org/10.1101/2021.01.14.426579; this version posted January 15, 2021. The copyright holder for this preprint (which was not certified by peer review) is the author/funder. All rights reserved. No reuse allowed without permission.

8. MacVicar, T. & Langer, T. OPA1 processing in cell death and disease - the long and short of it. *J. Cell Sci.* **129**, 2297–2306 (2016).
9. Twig, G. *et al.* Fission and selective fusion govern mitochondrial segregation and elimination by autophagy. *EMBO J.* **27**, 433–446 (2008).
10. Jacobi, D. *et al.* Hepatic Bmal1 Regulates Rhythmic Mitochondrial Dynamics and Promotes Metabolic Fitness. *Cell Metab* (2015).
11. Arruda, A. P. *et al.* Chronic enrichment of hepatic endoplasmic reticulum–mitochondria contact leads to mitochondrial dysfunction in obesity. *Nat. Med.* **20**, 1427–1435 (2014).
12. Gomes, L. C., Di Benedetto, G. & Scorrano, L. During autophagy mitochondria elongate, are spared from degradation and sustain cell viability. *Nat. Cell Biol.* **13**, 589–598 (2011).
13. Chen, H. *et al.* Mitochondrial Fusion Is Required for mtDNA Stability in Skeletal Muscle and Tolerance of mtDNA Mutations. *Cell* **141**, 280–289 (2010).
14. Elachouri, G. *et al.* OPA1 links human mitochondrial genome maintenance to mtDNA replication and distribution. *Genome Res.* **21**, 12–20 (2011).
15. Tondera, D. *et al.* SLP-2 is required for stress-induced mitochondrial hyperfusion. *EMBO J.* **28**, 1589–1600 (2009).
16. Rambold, A. S., Kostelecky, B. & Elia, N. Tubular network formation protects mitochondria from autophagosomal degradation during nutrient starvation. in *Proceedings of the \ldots* (2011).
17. Wai, T. *et al.* The membrane scaffold SLP2 anchors a proteolytic hub in mitochondria containing PARL and the i-AAA protease YME1L. *EMBO Rep.* e201642698–13 (2016).
18. Claypool, S. M. Cardiolipin, a critical determinant of mitochondrial carrier protein assembly and function. *Biochim. Biophys. Acta BBA - Biomembr.* **1788**, 2059–2068 (2009).
19. Spiegel, R. *et al.* Fatal infantile mitochondrial encephalomyopathy, hypertrophic cardiomyopathy and optic atrophy associated with a homozygous OPA1 mutation. *J. Med. Genet.* **53**, 127–131 (2016).

bioRxiv preprint doi: https://doi.org/10.1101/2021.01.14.426579; this version posted January 15, 2021. The copyright holder for this preprint (which was not certified by peer review) is the author/funder. All rights reserved. No reuse allowed without permission.

20. Carelli, V. *et al.* 'Behr syndrome' with OPA1 compound heterozygote mutations. *Brain J. Neurol.* **138**, e321 (2015).
21. Varanita, T. *et al.* The OPA1-dependent mitochondrial cristae remodeling pathway controls atrophic, apoptotic, and ischemic tissue damage. *Cell Metab* **21**, 834–844 (2015).
22. Frezza, C. *et al.* OPA1 controls apoptotic cristae remodeling independently from mitochondrial fusion. *Cell* **126**, 177–189 (2006).
23. Patten, D. A. *et al.* OPA1-dependent cristae modulation is essential for cellular adaptation to metabolic demand. *EMBO J* **33**, 2676–2691 (2014).
24. Ishihara, N., Fujita, Y., Oka, T. & Mihara, K. Regulation of mitochondrial morphology through proteolytic cleavage of OPA1. *EMBO J* **25**, 2966–2977 (2006).
25. Osellame, L. D. *et al.* Cooperative and independent roles of the Drp1 adaptors Mff, MiD49 and MiD51 in mitochondrial fission. *J Cell Sci* **129**, 2170–2181 (2016).
26. Anand, R. *et al.* The i-AAA protease YME1L and OMA1 cleave OPA1 to balance mitochondrial fusion and fission. *J Cell Biol* **204**, 919–929 (2014).
27. Kane, M. S. *et al.* Autophagy controls the pathogenicity of OPA1mutations in dominant optic atrophy. *J Cell Mol Med* **278**, 7743–14 (2017).
28. Iannetti, E. F., Smeitink, J. A. M., Beyrath, J., Willems, P. H. G. M. & Koopman, W. J. H. Multiplexed high-content analysis of mitochondrial morphofunction using live-cell microscopy. **11**, 1693–1710 (2016).
29. Jakobs, S., Stephan, T., Ilgen, P. & Brüser, C. Light Microscopy of Mitochondria at the Nanoscale. *Annu. Rev. Biophys.* **49**, 289–308 (2020).
30. Yu-Wai-Man, P. *et al.* Multi-system neurological disease is common in patients with OPA1 mutations. *Brain* **133**, 771–786 (2010).
31. Amati-Bonneau, P. *et al.* OPA1 R445H mutation in optic atrophy associated with sensorineural deafness. *Ann. Neurol.* **58**, 958–963 (2005).

bioRxiv preprint doi: https://doi.org/10.1101/2021.01.14.426579; this version posted January 15, 2021. The copyright holder for this preprint (which was not certified by peer review) is the author/funder. All rights reserved. No reuse allowed without permission.

32. Chen, H. *et al.* Titration of mitochondrial fusion rescues Mff-deficient cardiomyopathy. *J. Cell Biol.* **211**, 795–805 (2015).

33. Wai, T. *et al.* Imbalanced OPA1 processing and mitochondrial fragmentation cause heart failure in mice. *Science* **350**, aad0116–aad0116 (2015).

34. Yamada, T. *et al.* Mitochondrial Stasis Reveals p62-Mediated Ubiquitination in Parkin-Independent Mitophagy and Mitigates Nonalcoholic Fatty Liver Disease. *Cell Metab.* **28**, 588-604.e5 (2018).

35. Pesch, U. E. *et al.* OPA1 mutations in patients with autosomal dominant optic atrophy and evidence for semi-dominant inheritance. *Hum. Mol. Genet.* **10**, 1359–1368 (2001).

36. Rath, S. *et al.* MitoCarta3.0: an updated mitochondrial proteome now with sub-organelle localization and pathway annotations. *Nucleic Acids Res.* doi:10.1093/nar/gkaa1011.

37. Smith, A. C. & Robinson, A. J. MitoMiner v4.0: an updated database of mitochondrial localization evidence, phenotypes and diseases. *Nucleic Acids Res.* **47**, D1225–D1228 (2019).

38. Sechi, S., Frappaolo, A., Belloni, G., Colotti, G. & Giansanti, M. G. The multiple cellular functions of the oncoprotein Golgi phosphoprotein 3. *Oncotarget* **6**, 3493–3506 (2015).

39. Niemi, N. M. *et al.* Pptc7 is an essential phosphatase for promoting mammalian mitochondrial metabolism and biogenesis. *Nat. Commun.* **10**, 3197 (2019).

40. Bingol, B. *et al.* The mitochondrial deubiquitinase USP30 opposes parkin-mediated mitophagy. *Nature* **510**, 370–375 (2014).

41. N, N. & S, H. Regulation of mitochondrial morphology by USP30, a deubiquitinating enzyme present in the mitochondrial outer membrane. *Molecular biology of the cell* vol. 19 https://pubmed.ncbi.nlm.nih.gov/18287522/ (2008).

42. Janer, A. *et al.* SLC25A46is required for mitochondrial lipid homeostasis and cristae maintenance and is responsible for Leigh syndrome. *EMBO Mol Med* **8**, 1019–1038 (2016).

bioRxiv preprint doi: https://doi.org/10.1101/2021.01.14.426579; this version posted January 15, 2021. The copyright holder for this preprint (which was not certified by peer review) is the author/funder. All rights reserved. No reuse allowed without permission.

43. Abrams, A. J. *et al.* Mutations in SLC25A46 , encoding a UGO1-like protein, cause an optic atrophy spectrum disorder. *Nat. Genet.* **47**, 926–932 (2015).
44. Koch, J. *et al.* Disturbed mitochondrial and peroxisomal dynamics due to loss of MFF causes Leigh-like encephalopathy, optic atrophy and peripheral neuropathy. *J. Med. Genet.* **53**, jmedgenet–2015–103500–10 (2016).
45. Wang, K. *et al.* NFAT4-dependent miR-324-5p regulates mitochondrial morphology and cardiomyocyte cell death by targeting Mtfr1. *Cell Death Dis.* **6**, e2007–e2007 (2015).
46. Soreze, Y. *et al.* Mutations in human lipoyltransferase gene LIPT1 cause a Leigh disease with secondary deficiency for pyruvate and alpha-ketoglutarate dehydrogenase. *Orphanet J. Rare Dis.* **8**, 192 (2013).
47. Habarou, F. *et al.* Biallelic Mutations in LIPT2 Cause a Mitochondrial Lipoylation Defect Associated with Severe Neonatal Encephalopathy. *Am. J. Hum. Genet.* **101**, 283–290 (2017).
48. Flaschker, N. *et al.* Description of the mutations in 15 subjects with variant forms of maple syrup urine disease. *J. Inherit. Metab. Dis.* **30**, 903–909 (2007).
49. Tondera, D. The mitochondrial protein MTP18 contributes to mitochondrial fission in mammalian cells. *J Cell Sci* **118**, 3049–3059 (2005).
50. Gandre-Babbe, S. & van der Bliek, A. M. The novel tail-anchored membrane protein Mff controls mitochondrial and peroxisomal fission in mammalian cells. *Mol. Biol. Cell* **19**, 2402–2412 (2008).
51. Smirnova, E., Griparic, L., Shurland, D. L. & van der Bliek, A. M. Dynamin-related protein Drp1 is required for mitochondrial division in mammalian cells. *Mol. Biol. Cell* **12**, 2245–2256 (2001).
52. Stephan, T. *et al.* MICOS assembly controls mitochondrial inner membrane remodeling and crista junction redistribution to mediate cristae formation. *EMBO J.* **39**, e104105 (2020).

bioRxiv preprint doi: https://doi.org/10.1101/2021.01.14.426579; this version posted January 15, 2021. The copyright holder for this preprint (which was not certified by peer review) is the author/funder. All rights reserved. No reuse allowed without permission.

53. Chang, S. C., Heacock, P. N., Clancey, C. J. & Dowhan, W. The PEL1 gene (renamed PGS1) encodes the phosphatidylglycero-phosphate synthase of Saccharomyces cerevisiae. *J. Biol. Chem.* **273**, 9829–9836 (1998).

54. Tamura, Y., Kawano, S. & Endo, T. Lipid homeostasis in mitochondria. *Biol. Chem.* **401**, 821–833 (2020).

55. Dudek, J. Role of Cardiolipin in Mitochondrial Signaling Pathways. *Front. Cell Dev. Biol.* **5**, 90 (2017).

56. Ban, T. *et al.* Molecular basis of selective mitochondrial fusion by heterotypic action between OPA1 and cardiolipin. *Nat. Cell Biol.* **19**, 856–863 (2017).

57. Del Dotto, V. *et al.* Deciphering OPA1 mutations pathogenicity by combined analysis of human, mouse and yeast cell models. *Biochim. Biophys. Acta Mol. Basis Dis.* **1864**, 3496–3514 (2018).

58. Akepati, V. R. *et al.* Characterization of OPA1 isoforms isolated from mouse tissues. *J. Neurochem.* **106**, 372–383 (2008).

59. Song, Z., Chen, H., Fiket, M., Alexander, C. & Chan, D. C. OPA1 processing controls mitochondrial fusion and is regulated by mRNA splicing, membrane potential, and Yme1L. *J. Cell Biol.* **178**, 749–755 (2007).

60. Mishra, P., Carelli, V., Manfredi, G. & Chan, D. C. Proteolytic cleavage of Opa1 stimulates mitochondrial inner membrane fusion and couples fusion to oxidative phosphorylation. *Cell Metab.* **19**, 630–641 (2014).

61. Chen, W. W., Freinkman, E., Wang, T., Birsoy, K. & Sabatini, D. M. Absolute Quantification of Matrix Metabolites Reveals the Dynamics of Mitochondrial Metabolism. *Cell* **166**, 1324-1337.e11 (2016).

62. Adachi, Y. *et al.* Coincident Phosphatidic Acid Interaction Restrains Drp1 in Mitochondrial Division. *Mol. Cell* **63**, 1034–1043 (2016).

bioRxiv preprint doi: https://doi.org/10.1101/2021.01.14.426579; this version posted January 15, 2021. The copyright holder for this preprint (which was not certified by peer review) is the author/funder. All rights reserved. No reuse allowed without permission.

63. Mitra, K. & Lippincott-Schwartz, J. Analysis of Mitochondrial Dynamics and Functions Using Imaging Approaches. *Curr. Protoc. Cell Biol.* **46**, 4.25.1-4.25.21 (2010).

64. Zhang, J. *et al.* Mitochondrial phosphatase PTPMT1 is essential for cardiolipin biosynthesis. *Cell Metab.* **13**, 690–700 (2011).

65. Chen, D., Zhang, X.-Y. & Shi, Y. Identification and functional characterization of hCLS1, a human cardiolipin synthase localized in mitochondria. *Biochem. J.* **398**, 169–176 (2006).

66. Watanabe, T. *et al.* MITOPLD Is a Mitochondrial Protein Essential for Nuage Formation and piRNA Biogenesis in the Mouse Germline. *Dev. Cell* **20**, 364–375 (2011).

67. Huang, H. *et al.* piRNA-Associated Germline Nuage Formation and Spermatogenesis Require MitoPLD Profusogenic Mitochondrial-Surface Lipid Signaling. *Dev. Cell* **20**, 376–387 (2011).

68. Potting, C. *et al.* TRIAP1/PRELI Complexes Prevent Apoptosis by Mediating Intramitochondrial Transport of Phosphatidic Acid. *Cell Metab.* **18**, 287–295 (2013).

69. Connerth, M. *et al.* Intramitochondrial Transport of Phosphatidic Acid in Yeast by a Lipid Transfer Protein. *Science* **338**, 815–818 (2012).

70. Kushnareva, Y. *et al.* Mitochondrial dysfunction in an Opa1 Q285STOP mouse model of dominant optic atrophy results from Opa1 haploinsufficiency. *Cell Death Dis.* **7**, e2309–e2309 (2016).

71. Bonifert, T. *et al.* Pure and syndromic optic atrophy explained by deep intronic OPA1 mutations and an intralocus modifier. *Brain* **137**, 2164–2177 (2014).

72. To, T.-L. *et al.* A Compendium of Genetic Modifiers of Mitochondrial Dysfunction Reveals Intra-organelle Buffering. *Cell* **179**, 1222-1238.e17 (2019).

73. Lebeau, J. *et al.* The PERK Arm of the Unfolded Protein Response Regulates Mitochondrial Morphology during Acute Endoplasmic Reticulum Stress. *Cell Rep.* **22**, 2827–2836 (2018).

74. Morita, M. *et al.* mTOR Controls Mitochondrial Dynamics and Cell Survival via MTFP1. *Mol. Cell* **67**, 922-935.e5 (2017).

bioRxiv preprint doi: https://doi.org/10.1101/2021.01.14.426579; this version posted January 15, 2021. The copyright holder for this preprint (which was not certified by peer review) is the author/funder. All rights reserved. No reuse allowed without permission.

75. Matsumura, A. *et al.* Inactivation of cardiolipin synthase triggers changes in mitochondrial morphology. *FEBS Lett.* **592**, 209–218 (2018).

76. Ban, T., Kohno, H., Ishihara, T. & Ishihara, N. Relationship between OPA1 and cardiolipin in mitochondrial inner-membrane fusion. *Biochim. Biophys. Acta BBA - Bioenerg.* **1859**, 951–957 (2018).

77. Tamura, Y., Kawano, S. & Endo, T. Lipid homeostasis in mitochondria. *Biol. Chem.* **401**, 821–833 (2020).

78. Aaltonen, M. J. *et al.* MICOS and phospholipid transfer by Ups2–Mdm35 organize membrane lipid synthesis in mitochondria. *J. Cell Biol.* **213**, 525–534 (2016).

79. Xie, Q. *et al.* Mitochondrial control by DRP1 in brain tumor initiating cells. *Nat. Publ. Group* **18**, 501–510 (2015).

80. Acin-Perez, R. *et al.* Ablation of the stress protease OMA1 protects against heart failure in mice. *Sci. Transl. Med.* **10**, (2018).

81. Xiao, X. *et al.* OMA1 mediates OPA1 proteolysis and mitochondrial fragmentation in experimental models of ischemic kidney injury. *Am. J. Physiol.-Ren. Physiol.* **306**, F1318–F1326 (2014).

82. Bartsakoulia, M. *et al.* A novel mechanism causing imbalance of mitochondrial fusion and fission in human myopathies. *Hum. Mol. Genet.* **27**, 1186–1195 (2018).

83. Rv, B. *et al.* Ganglioside-induced differentiation-associated protein-1 is mutant in Charcot-Marie-Tooth disease type 4A/8q21. *Nature genetics* vol. 30 https://pubmed.ncbi.nlm.nih.gov/11743579/ (2002).

84. Boyer, O. *et al.* INF2 Mutations in Charcot–Marie–Tooth Disease with Glomerulopathy. *N. Engl. J. Med.* **365**, 2377–2388 (2011).

85. Livak, K. J. & Schmittgen, T. D. Analysis of Relative Gene Expression Data Using Real-Time Quantitative PCR and the 2−ΔΔCT Method. *Methods* **25**, 402–408 (2001).

bioRxiv preprint doi: https://doi.org/10.1101/2021.01.14.426579; this version posted January 15, 2021. The copyright holder for this preprint (which was not certified by peer review) is the author/funder. All rights reserved. No reuse allowed without permission.

86. Chen, W. W., Freinkman, E. & Sabatini, D. M. Rapid immunopurification of mitochondria for metabolite profiling and absolute quantification of matrix metabolites. *Nat. Protoc.* **12**, 2215–2231 (2017).

87. McDonald, K. *et al.* "Tips and Tricks" for High-Pressure Freezing of Model Systems. in *Methods in Cell Biology* vol. 96 671–693 (Elsevier, 2010).

88. Walther, P. & Ziegler, A. Freeze substitution of high-pressure frozen samples: the visibility of biological membranes is improved when the substitution medium contains water. *J. Microsc.* **208**, 3–10 (2002).

89. Mastronarde, D. N. Automated electron microscope tomography using robust prediction of specimen movements. *J. Struct. Biol.* **152**, 36–51 (2005).

90. Schorb, M., Haberbosch, I., Hagen, W. J. H., Schwab, Y. & Mastronarde, D. N. Software tools for automated transmission electron microscopy. *Nat. Methods* **16**, 471–477 (2019).

91. Kremer, J. R., Mastronarde, D. N. & McIntosh, J. R. Computer Visualization of Three-Dimensional Image Data Using IMOD. *J. Struct. Biol.* **116**, 71–76 (1996).

92. Mastronarde, D. N. & Held, S. R. Automated tilt series alignment and tomographic reconstruction in IMOD. *J. Struct. Biol.* **197**, 102–113 (2017).

93. Rueden, C. T. *et al.* ImageJ2: ImageJ for the next generation of scientific image data. *BMC Bioinformatics* **18**, 529 (2017).

94. Özbalci, C., Sachsenheimer, T. & Brügger, B. Quantitative analysis of cellular lipids by nano-electrospray ionization mass spectrometry. *Methods Mol. Biol. Clifton NJ* **1033**, 3–20 (2013).

95. Tatsuta, T. Quantitative Analysis of Glycerophospholipids in Mitochondria by Mass Spectrometry. *Methods Mol. Biol. Clifton NJ* **1567**, 79–103 (2017).

Acknowledgments

bioRxiv preprint doi: https://doi.org/10.1101/2021.01.14.426579; this version posted January 15, 2021. The copyright holder for this preprint (which was not certified by peer review) is the author/funder. All rights reserved. No reuse allowed without permission.

We thank Kristin Tsuo and Vincent Guillemot for statistical assistance in R, and Martin Sachse and Anastasia Gazi for EM sample preparation and image acquisition. We thank Mike Ryan for MEFs lacking MiD49/MiD51/Mff and Nils-Göran Larsson for providing mitoYFP mice. We thank Arnaud Echard for critical reading of the manuscript and Marie Lemesle for excellent administrative assistance. T.W. is supported by the European Research Council (ERC) Starting Grant No. 714472 (Acronym "*Mitomorphosis*") and ATIP-AVENIR (INSERM/CNRS). E.C. is supported by a PhD scholarship from the French Ministry of Higher Education, Research, and Innovation (Ministère français de l'Enseignement supérieur, de la Recherche et de l'Innovation). PYWM is supported by a Clinician Scientist Fellowship Award (G1002570) from the Medical Research Council (UK), and also receives funding from Fight for Sight (UK), Moorfields Eye Charity, the Isaac Newton Trust (UK), the Addenbrooke's Charitable Trust, the National Eye Research Centre (UK), the UK National Institute of Health Research (NIHR) as part of the Rare Diseases Translational Research Collaboration, and the NIHR Biomedical Research Centre based at Moorfields Eye Hospital NHS Foundation Trust and UCL Institute of Ophthalmology. The views expressed are those of the author(s) and not necessarily those of the NHS, the NIHR or the Department of Health. The authors declare that they have no conflict of interest.

bioRxiv preprint doi: https://doi.org/10.1101/2021.01.14.426575; this version posted January 15, 2021. The copyright holder for this preprint (which was not certified by peer review) is the author/funder. All rights reserved. No reuse allowed without permission.

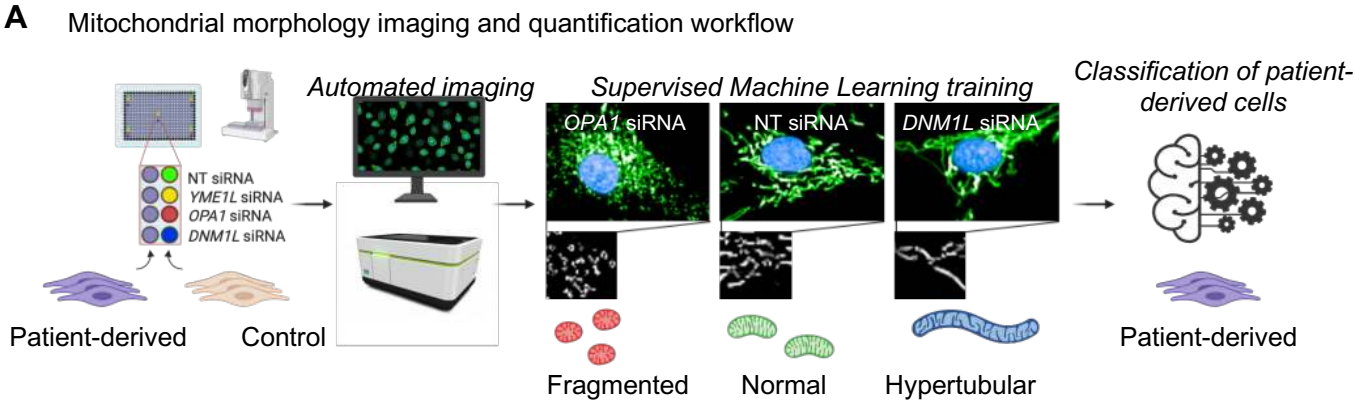

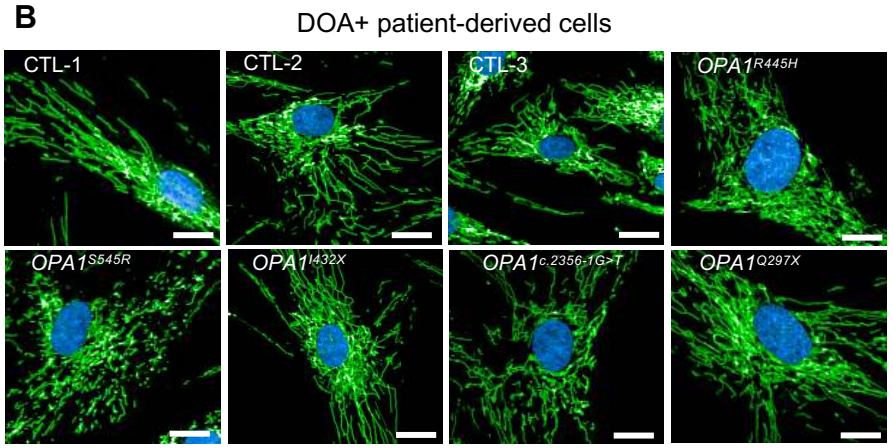

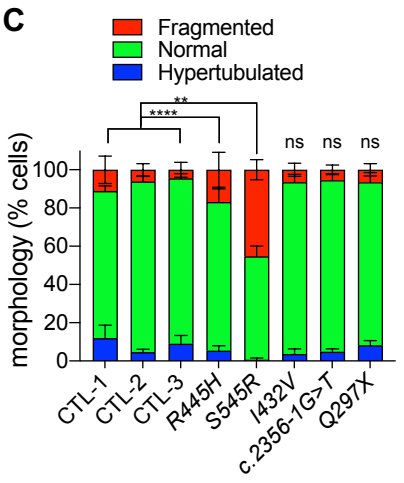

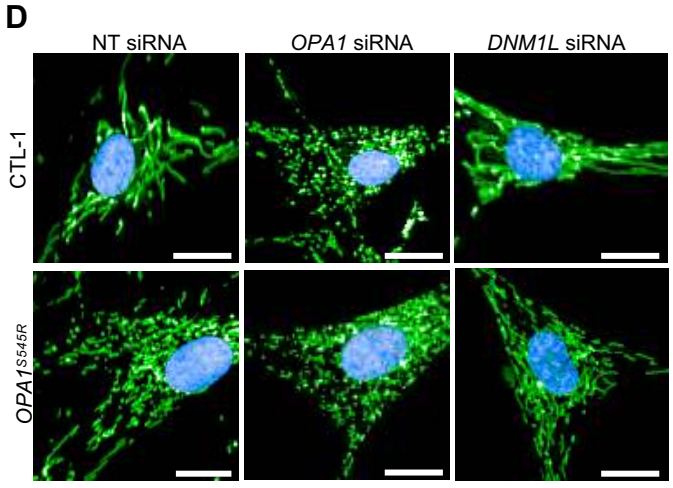

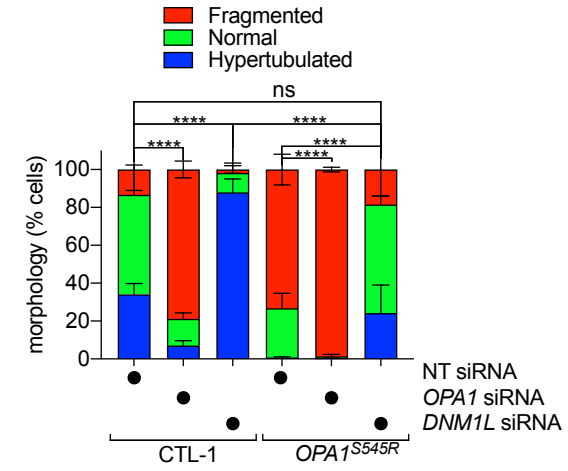

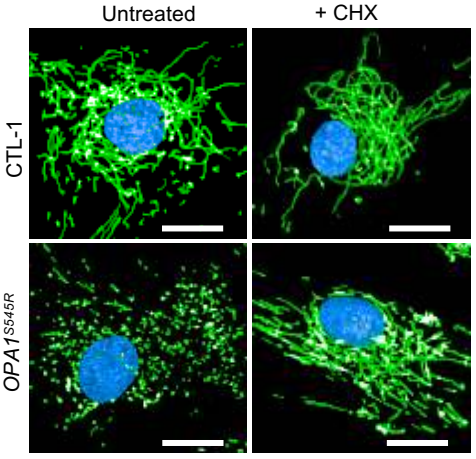

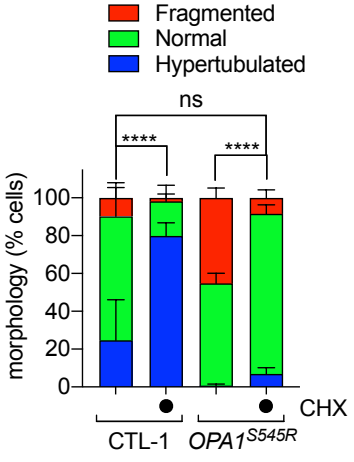

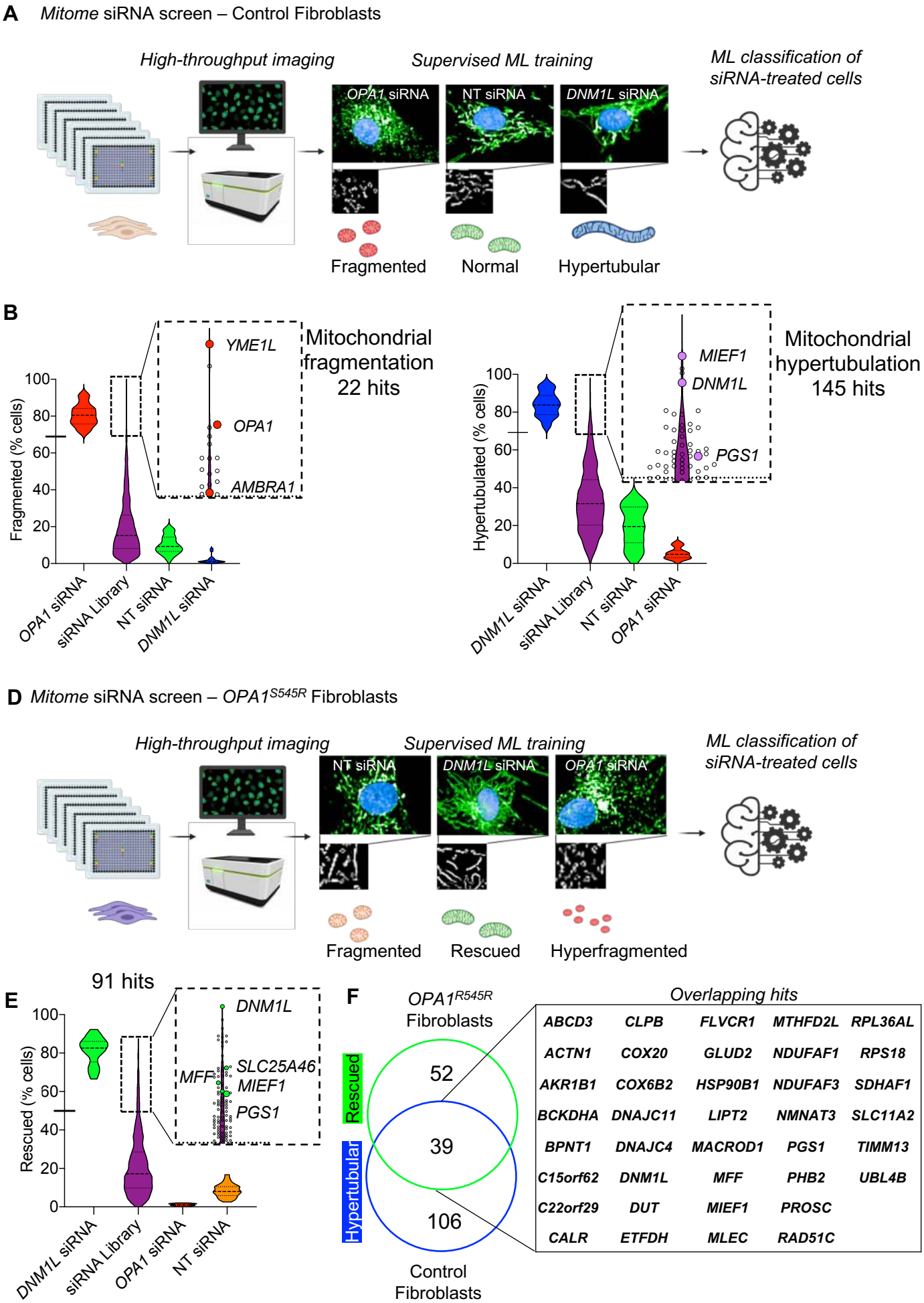
A
Mitome siRNA screen – Control Fibroblasts
High-throughput imaging
Supervised ML training
ML classification of siRNA-treated cells
OPA1 siRNA
NT siRNA
DNM1L siRNA
Fragmented
Normal
Hypertubular
B
Mitochondrial fragmentation 22 hits
Fragmented (% cells)
YME1L
OPA1
AMBRA1
OPA1 siRNA
siRNA Library
NT siRNA
DNM1L siRNA
Mitochondrial hypertubulation 145 hits
Hypertubulated (% cells)
MIEF1
DNM1L
PGS1
DNM1L siRNA
siRNA Library
NT siRNA
OPA1 siRNA
D
Mitome siRNA screen – OPA1S545R Fibroblasts
High-throughput imaging
Supervised ML training
ML classification of siRNA-treated cells
NT siRNA
DNM1L siRNA
OPA1 siRNA
Fragmented
Rescued
Hyperfragmented
E
91 hits
Rescued (% cells)
DNM1L
SLC25A46
MFF
MIEF1
PGS1
DNM1L siRNA
siRNA Library
OPA1 siRNA
NT siRNA
F
OPA1R545R Fibroblasts
Rescued
Hypertubular
52
39
106
Control Fibroblasts
Overlapping hits
ABCD3 CLPB FLVCR1 MTHFD2L RPL36AL
ACTN1 COX20 GLUD2 NDUFAF1 RPS18
AKR1B1 COX6B2 HSP90B1 NDUFAF3 SDHAF1
BCKDHA DNAJC11 LIPT2 NMNAT3 SLC11A2
BPNT1 DNAJC4 MACROD1 PGS1 TIMM13
C15orf62 DNM1L MFF PHB2 UBL4B
C22orf29 DUT MIEF1 PROSC
CALR ETFDH MLEC RAD51C

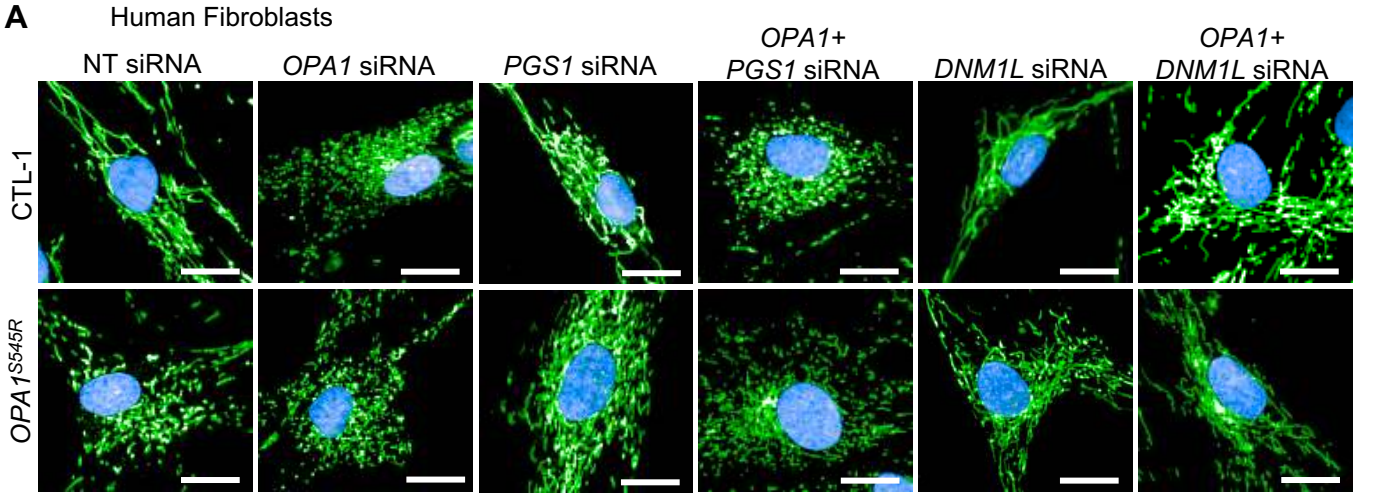
A
Human Fibroblasts
NT siRNA
OPA1 siRNA
PGS1 siRNA
OPA1+ PGS1 siRNA
DNM1L siRNA
OPA1+ DNM1L siRNA
CTL-1
OPA1S545R

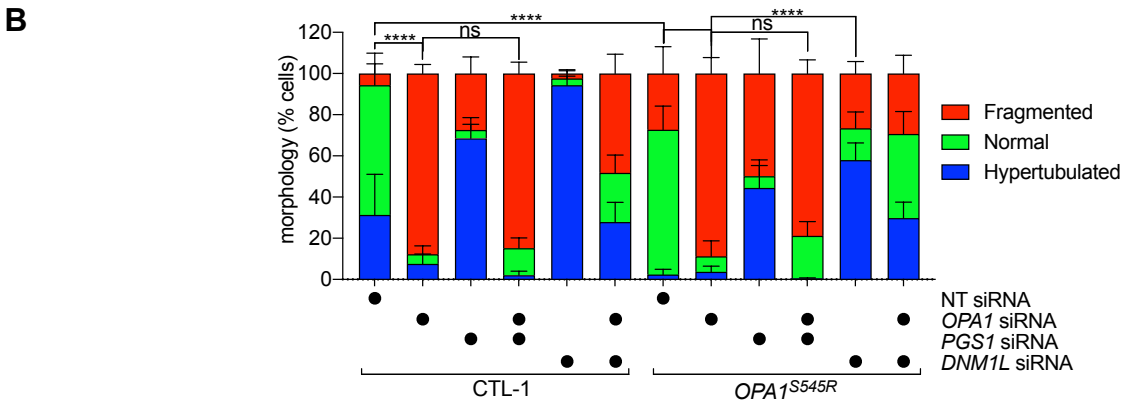
B
morphology (% cells)
Fragmented
Normal
Hypertubulated
NT siRNA
OPA1 siRNA
PGS1 siRNA
DNM1L siRNA
CTL-1
OPA1S545R

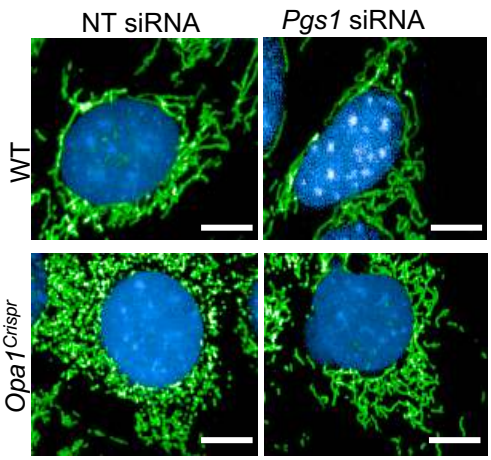
C
Mouse Fibroblasts
NT siRNA
Pgs1 siRNA
WT
Opa1Crispr

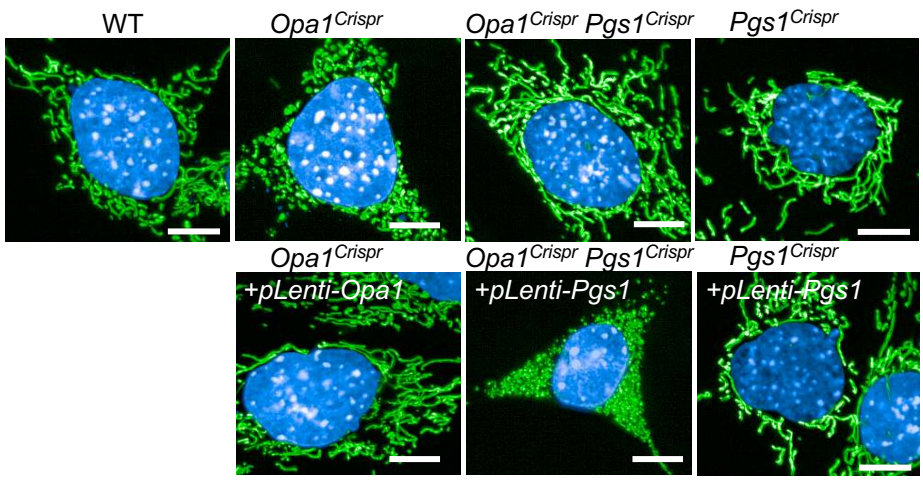
E
Mouse Fibroblasts
WT
Opa1Crispr
Opa1Crispr Pgs1Crispr
Pgs1Crispr
Opa1Crispr +pLenti-Opa1
Opa1Crispr Pgs1Crispr +pLenti-Pgs1
Pgs1Crispr +pLenti-Pgs1

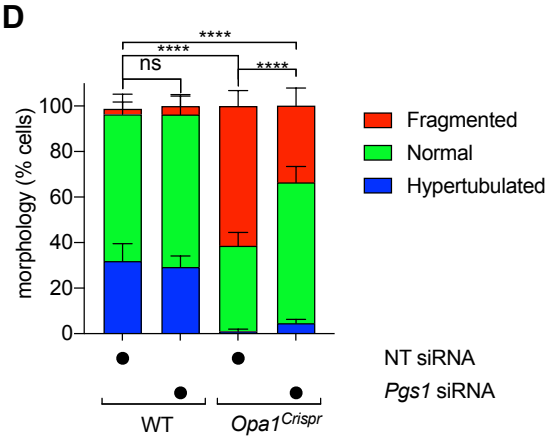
D
morphology (% cells)
Fragmented
Normal
Hypertubulated
NT siRNA
Pgs1 siRNA
WT
Opa1Crispr

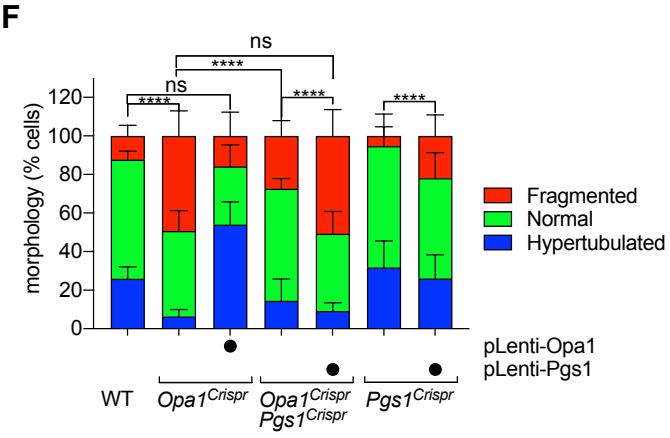
F
morphology (% cells)
Fragmented
Normal
Hypertubulated
pLenti-Opa1
pLenti-Pgs1
WT
Opa1Crispr
Opa1Crispr Pgs1Crispr
Pgs1Crispr

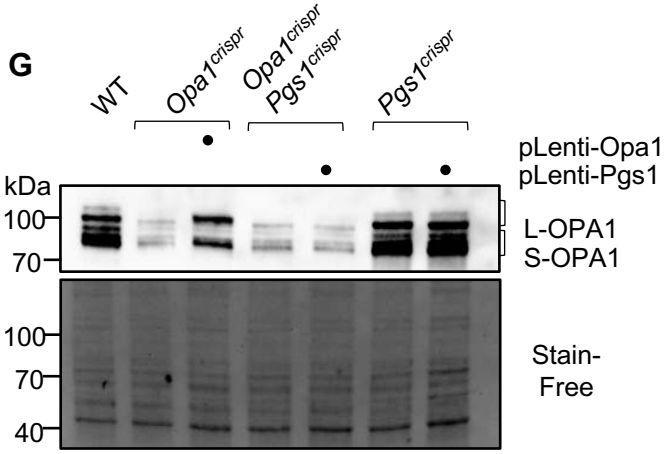
G
WT
Opa1crispr
Opa1crispr Pgs1crispr
Pgs1crispr
pLenti-Opa1
pLenti-Pgs1
kDa
100
70
L-OPA1
S-OPA1
100
70
40
Stain-Free

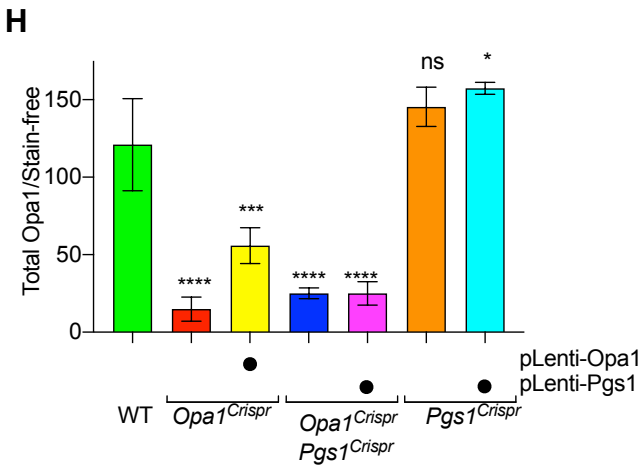
H
Total Opa1/Stain-free
150
100
50
0
ns
*
***
****
****
****
pLenti-Opa1
pLenti-Pgs1
WT
Opa1Crispr
Opa1Crispr Pgs1Crispr
Pgs1Crispr

A

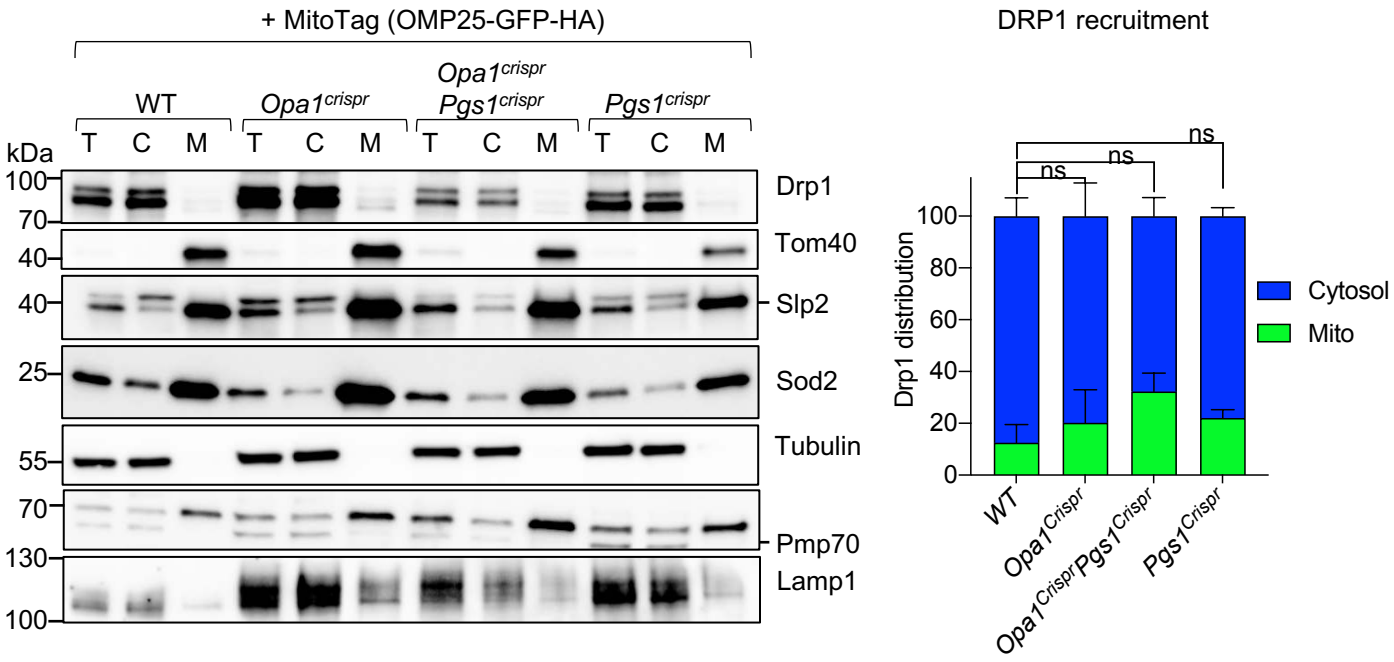
+ MitoTag (OMP25-GFP-HA)
WT
Opa1crispr
Opa1crispr Pgs1crispr
Pgs1crispr
T C M T C M T C M T C M
kDa
100
70
40
40
25
55
70
130
100
Drp1
Tom40
Slp2
Sod2
Tubulin
Pmp70
Lamp1
DRP1 recruitment
Drp1 distribution
ns
ns
ns
Cytosol
Mito
WT
Opa1Crispr
Opa1CrisprPgs1Crispr
Pgs1Crispr

B

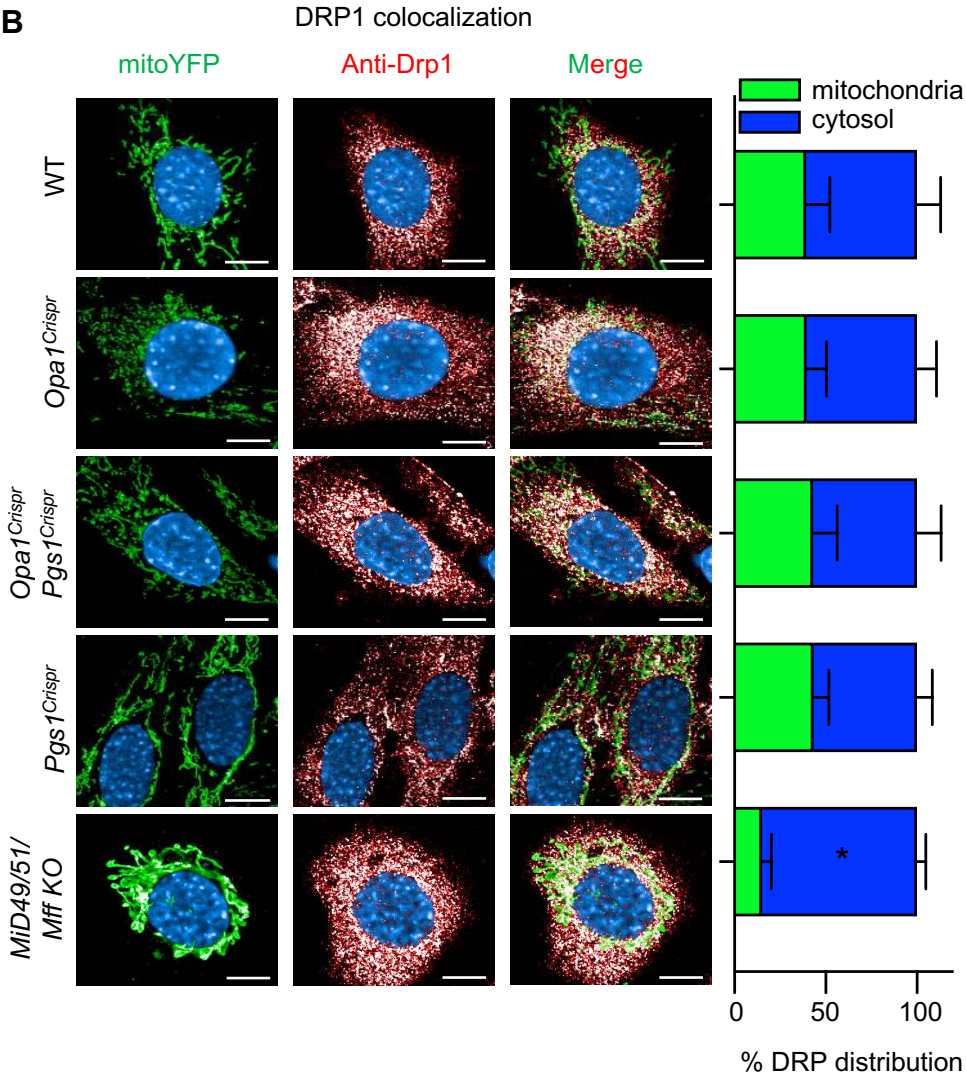
DRP1 colocalization
mitoYFP
Anti-Drp1
Merge
mitochondria
cytosol
WT
Opa1Crispr
Opa1CrisprPgs1Crispr
Pgs1Crispr
MiD49/51/ Mff KO
*
0
50
100
% DRP distribution

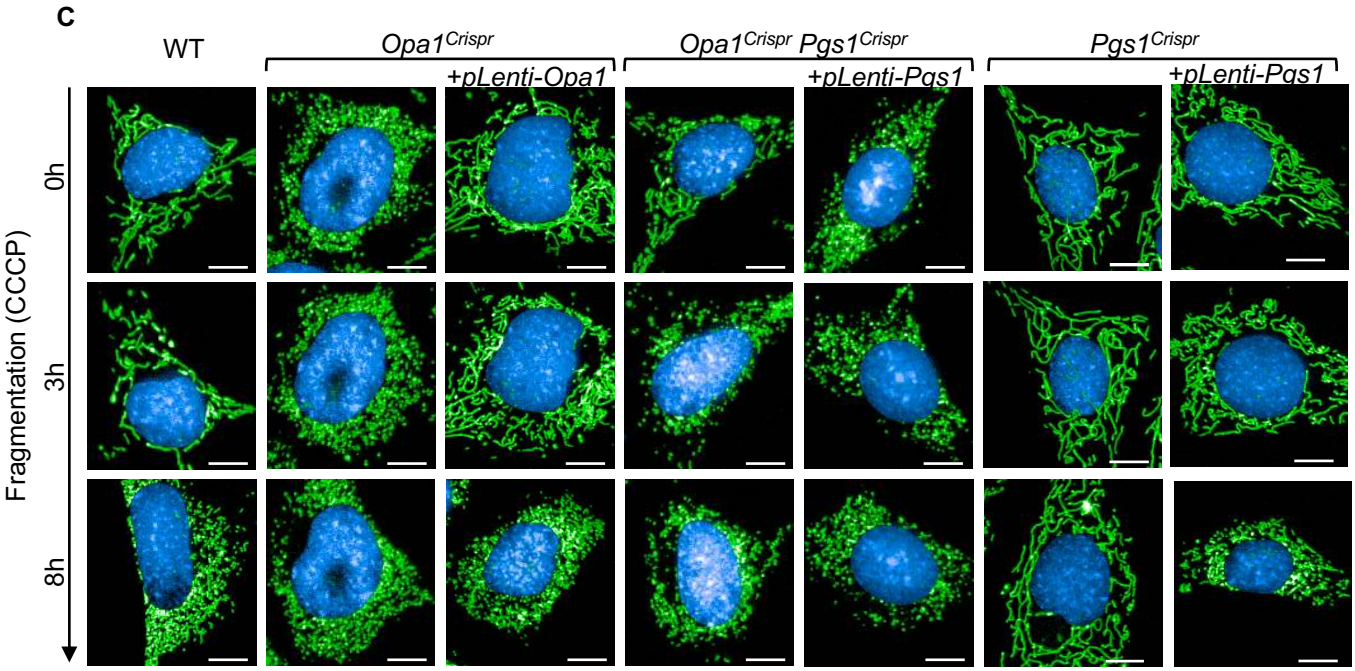
C
WT
Opa1Crispr
+pLenti-Opa1
Opa1Crispr Pgs1Crispr
+pLenti-Pgs1
Pgs1Crispr
+pLenti-Pgs1
0h
3h
8h
Fragmentation (CCCP)

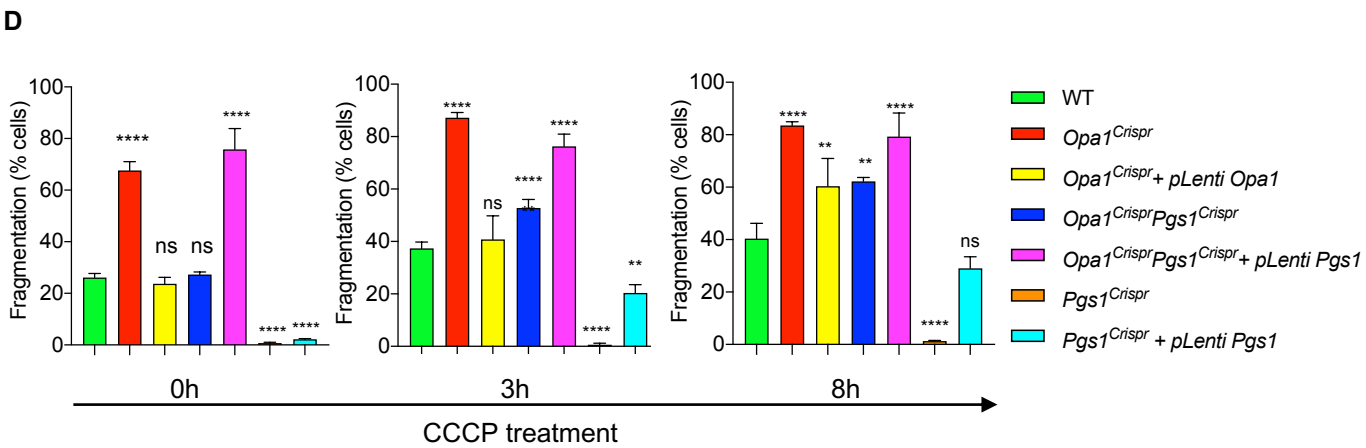
D
Fragmentation (% cells)
0h
3h
8h
CCCP treatment
WT
Opa1Crispr
Opa1Crispr+ pLenti Opa1
Opa1CrisprPgs1Crispr
Opa1CrisprPgs1Crispr+ pLenti Pgs1
Pgs1Crispr
Pgs1Crispr + pLenti Pgs1

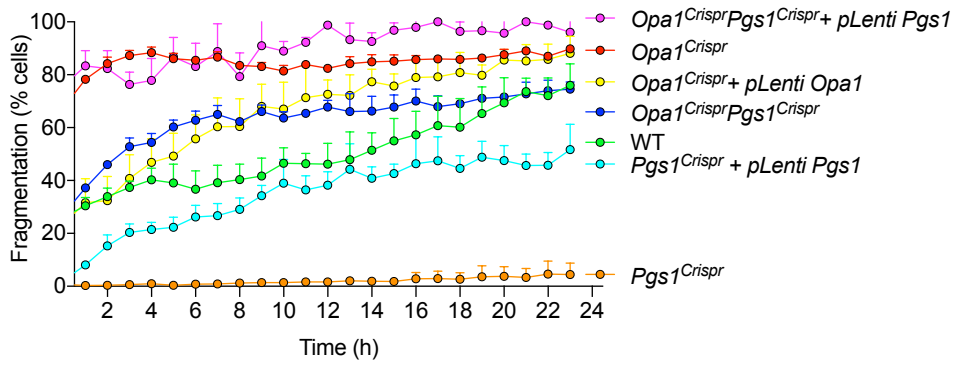
Fragmentation (% cells)
Time (h)
Opa1CrisprPgs1Crispr+ pLenti Pgs1
Opa1Crispr
Opa1Crispr+ pLenti Opa1
Opa1CrisprPgs1Crispr
WT
Pgs1Crispr + pLenti Pgs1
Pgs1Crispr

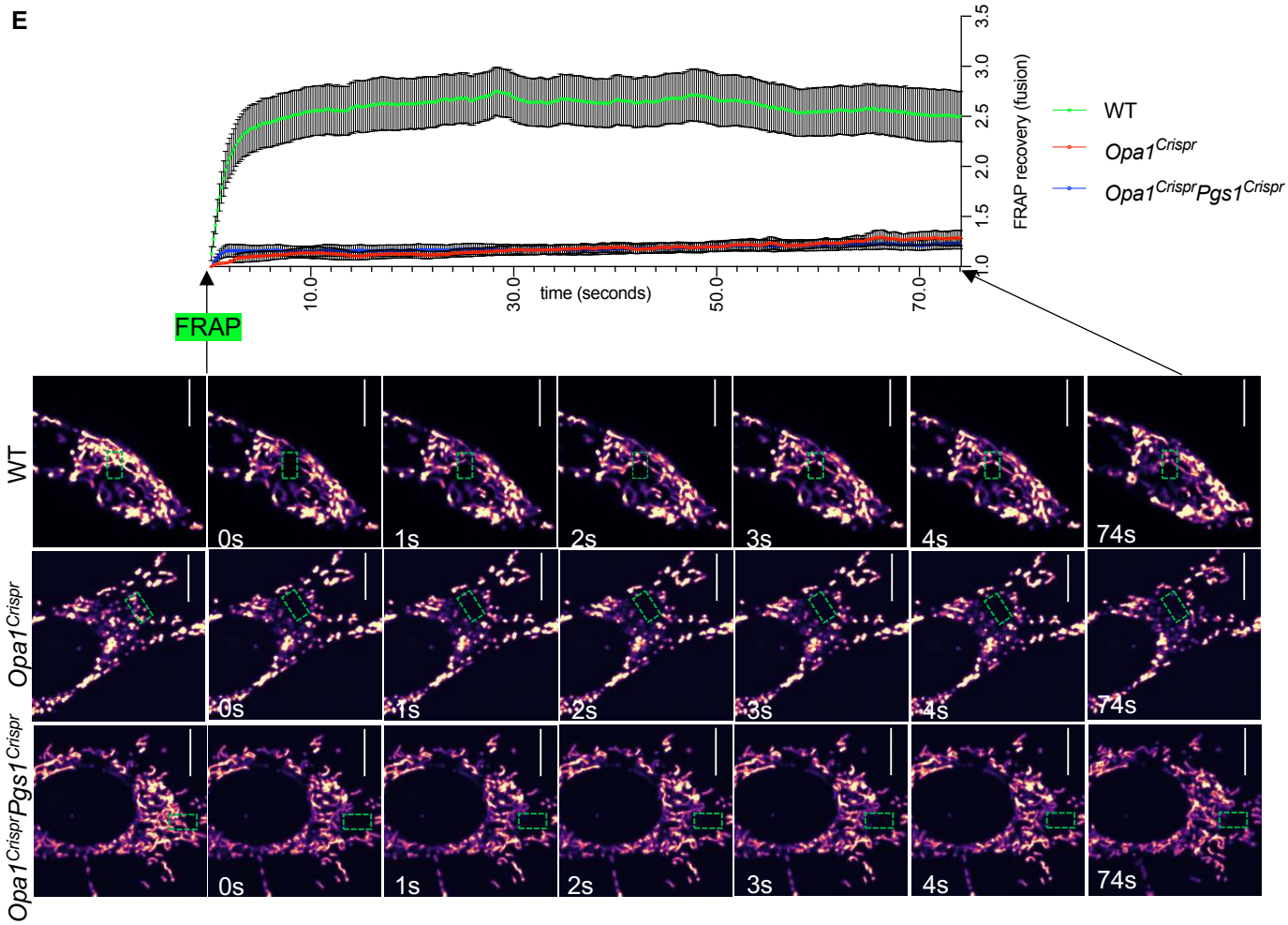
E
FRAP recovery (fusion)
WT
Opa1Crispr
Opa1CrisprPgs1Crispr
time (seconds)
FRAP
WT
Opa1Crispr
Opa1CrisprPgs1Crispr
0s
1s
2s
3s
4s
74s

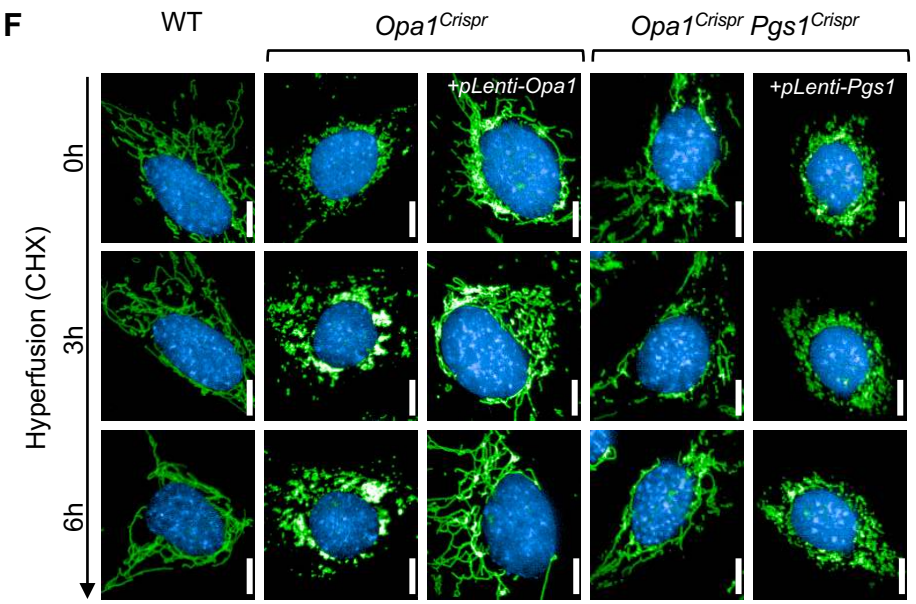
F
WT
Opa1Crispr
Opa1Crispr Pgs1Crispr
+pLenti-Opa1
+pLenti-Pgs1
Hyperfusion (CHX)
0h
3h
6h

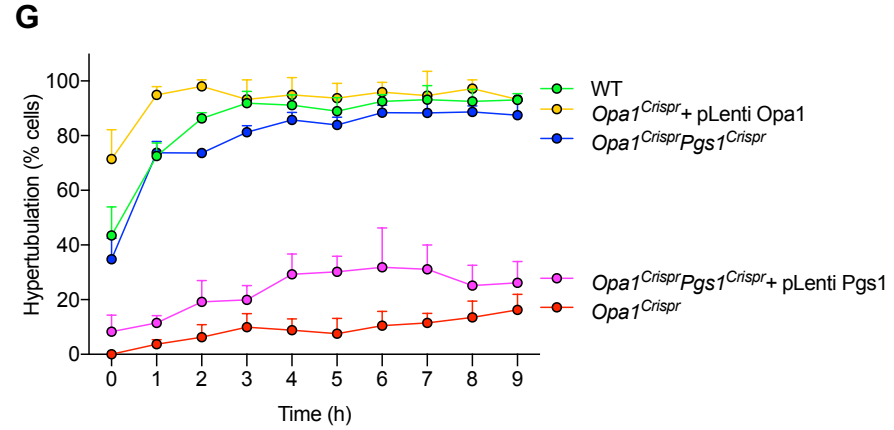
G
Hypertubulation (% cells)
Time (h)
WT
Opa1Crispr+ pLenti Opa1
Opa1CrisprPgs1Crispr
Opa1CrisprPgs1Crispr+ pLenti Pgs1
Opa1Crispr

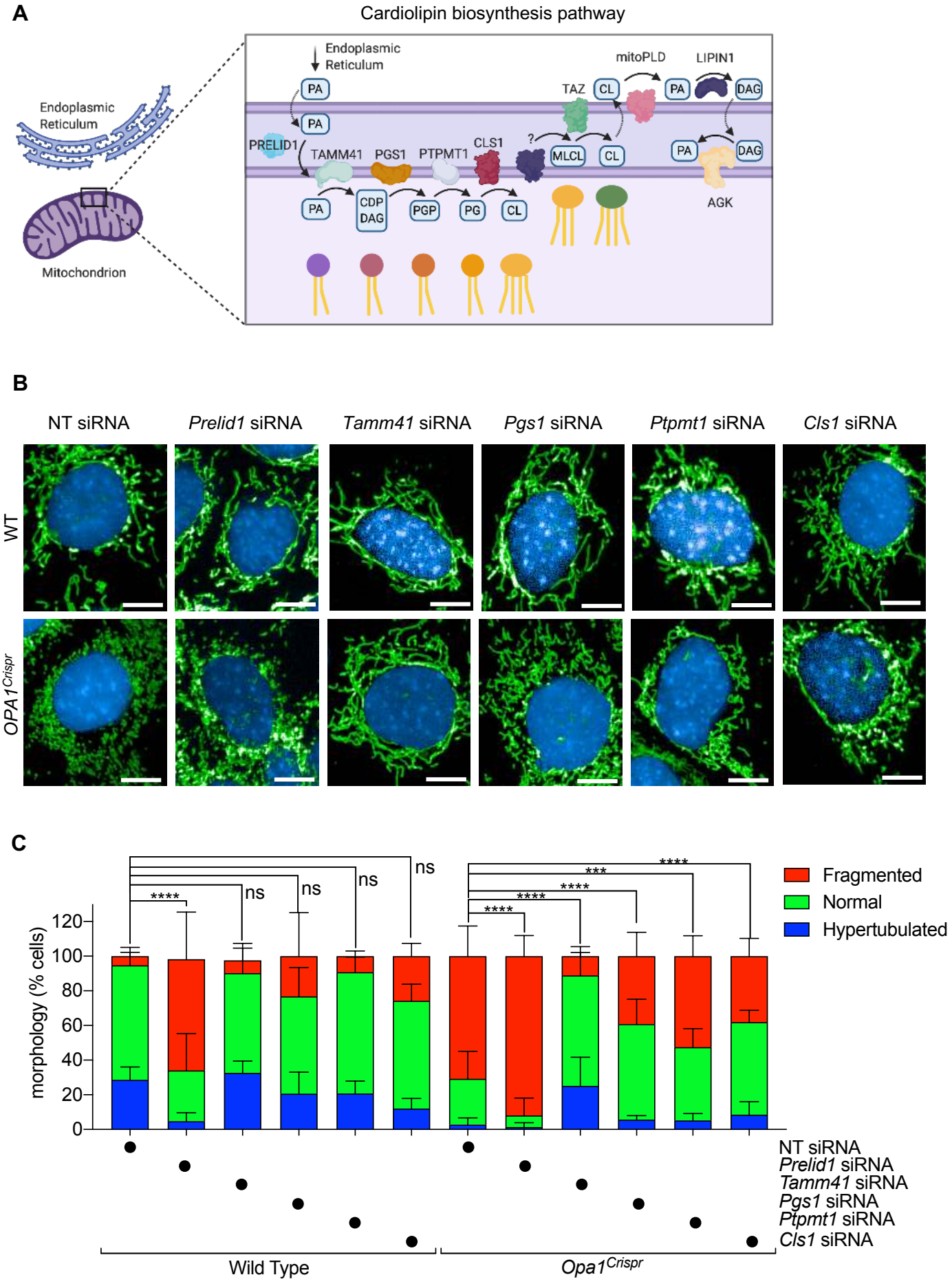
A
Cardiolipin biosynthesis pathway
Endoplasmic Reticulum
Mitochondrion
Endoplasmic Reticulum
PA
PA
PRELID1
TAMM41
PGS1
PTPMT1
CLS1
PA
CDP DAG
PGP
PG
CL
?
MLCL
CL
TAZ
CL
mitoPLD
PA
LIPIN1
DAG
PA
DAG
AGK
B
NT siRNA
Prelid1 siRNA
Tamm41 siRNA
Pgs1 siRNA
Ptpmt1 siRNA
Cls1 siRNA
WT
OPA1Crispr
C
morphology (% cells)
120
100
80
60
40
20
0
****
ns
ns
ns
ns
***
****
****
****
****
Fragmented
Normal
Hypertubulated
NT siRNA
Prelid1 siRNA
Tamm41 siRNA
Pgs1 siRNA
Ptpmt1 siRNA
Cls1 siRNA
Wild Type
Opa1Crispr

Figure 5 cont'd

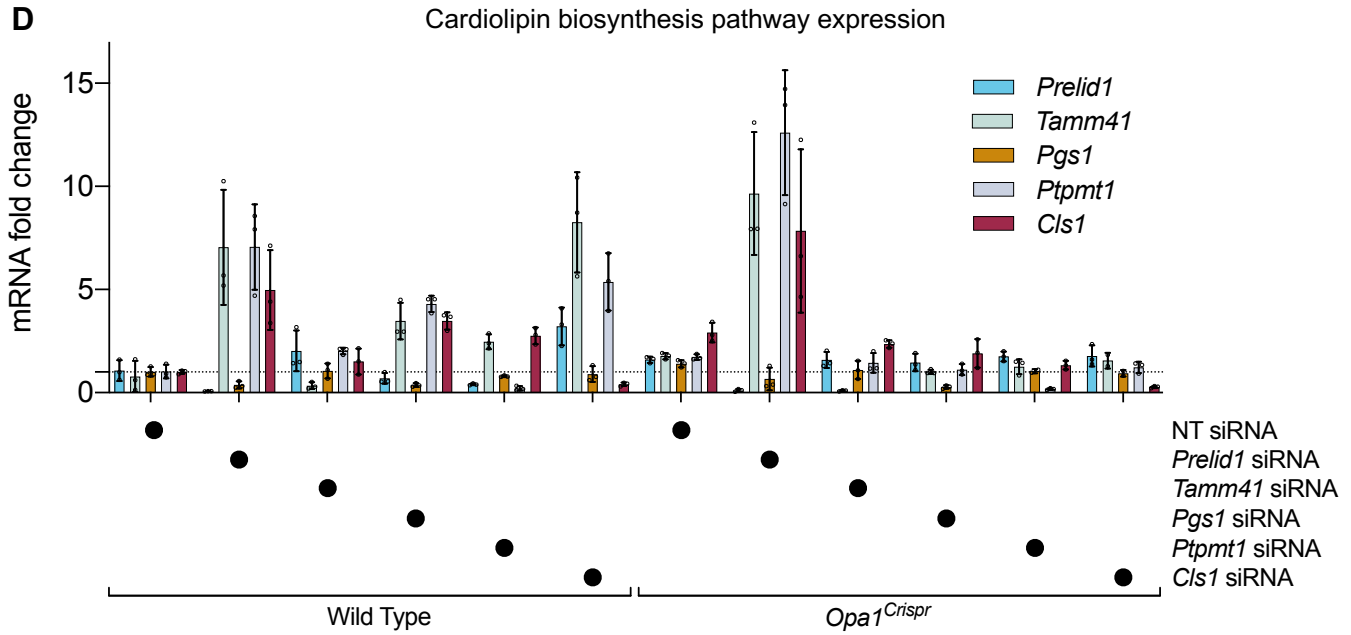

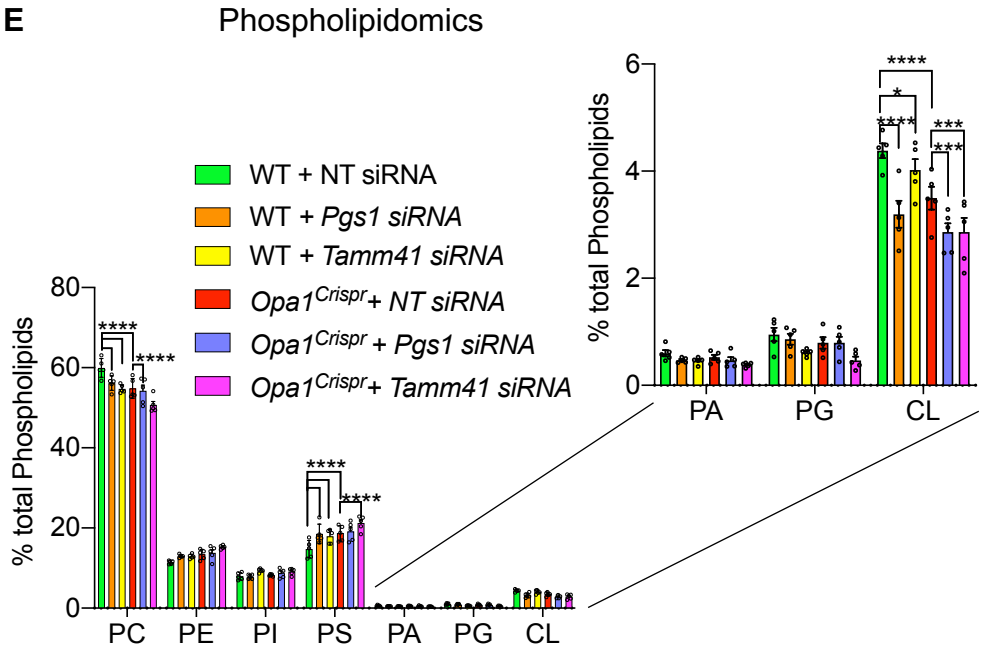

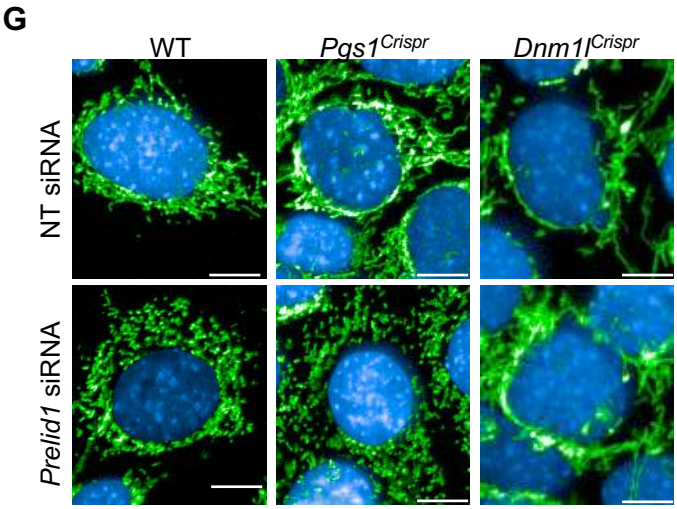

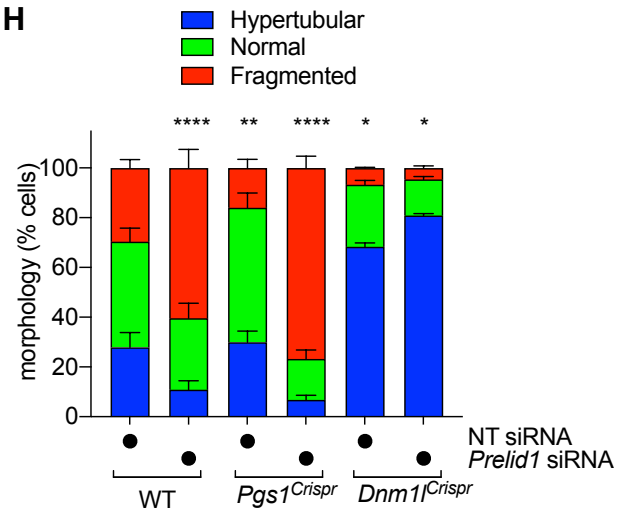

Figure 5 cont

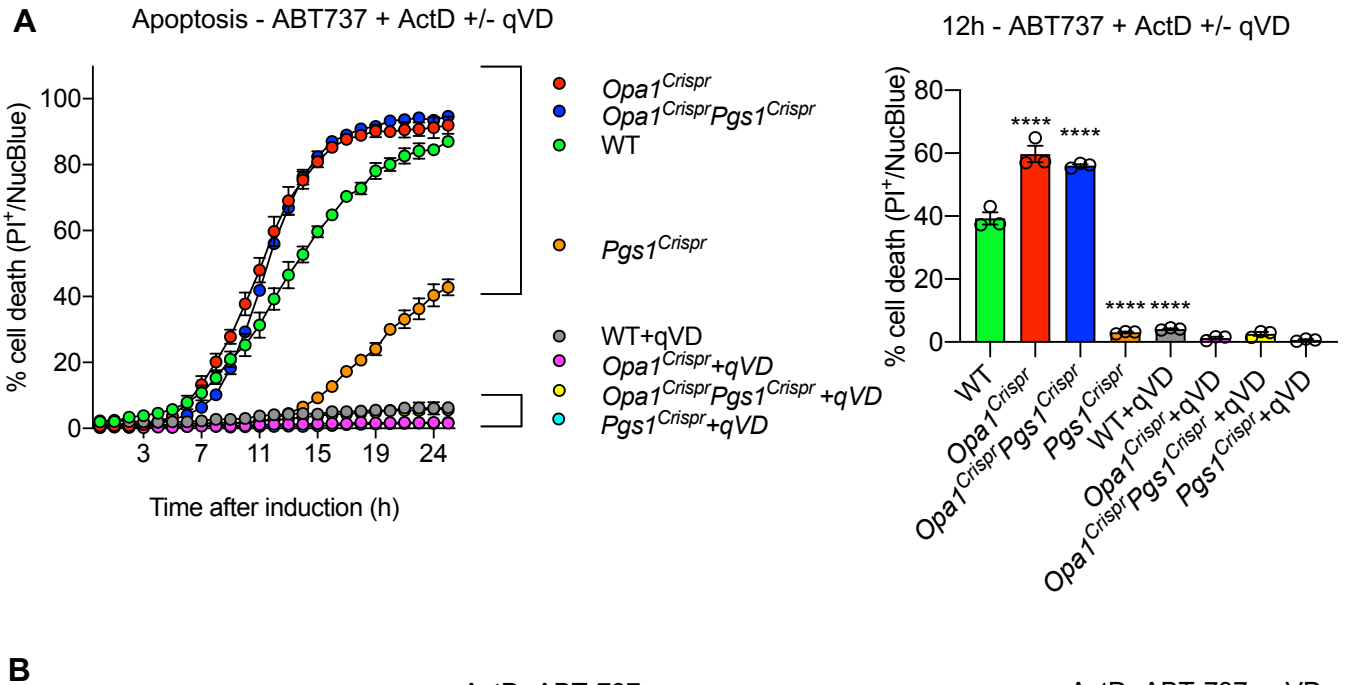
A
Apoptosis - ABT737 + ActD +/- qVD
% cell death (PI+/NucBlue)
Time after induction (h)
Opa1Crispr
Opa1CrispPgs1Crispr
WT
Pgs1Crispr
WT+qVD
Opa1Crispr+qVD
Opa1CrispPgs1Crispr +qVD
Pgs1Crispr+qVD
12h - ABT737 + ActD +/- qVD
% cell death (PI+/NucBlue)
****
WT
Opa1Crispr
Opa1CrispPgs1Crispr
Pgs1Crispr
WT+qVD
Opa1Crispr+qVD
Opa1CrispPgs1Crispr +qVD
Pgs1Crispr+qVD

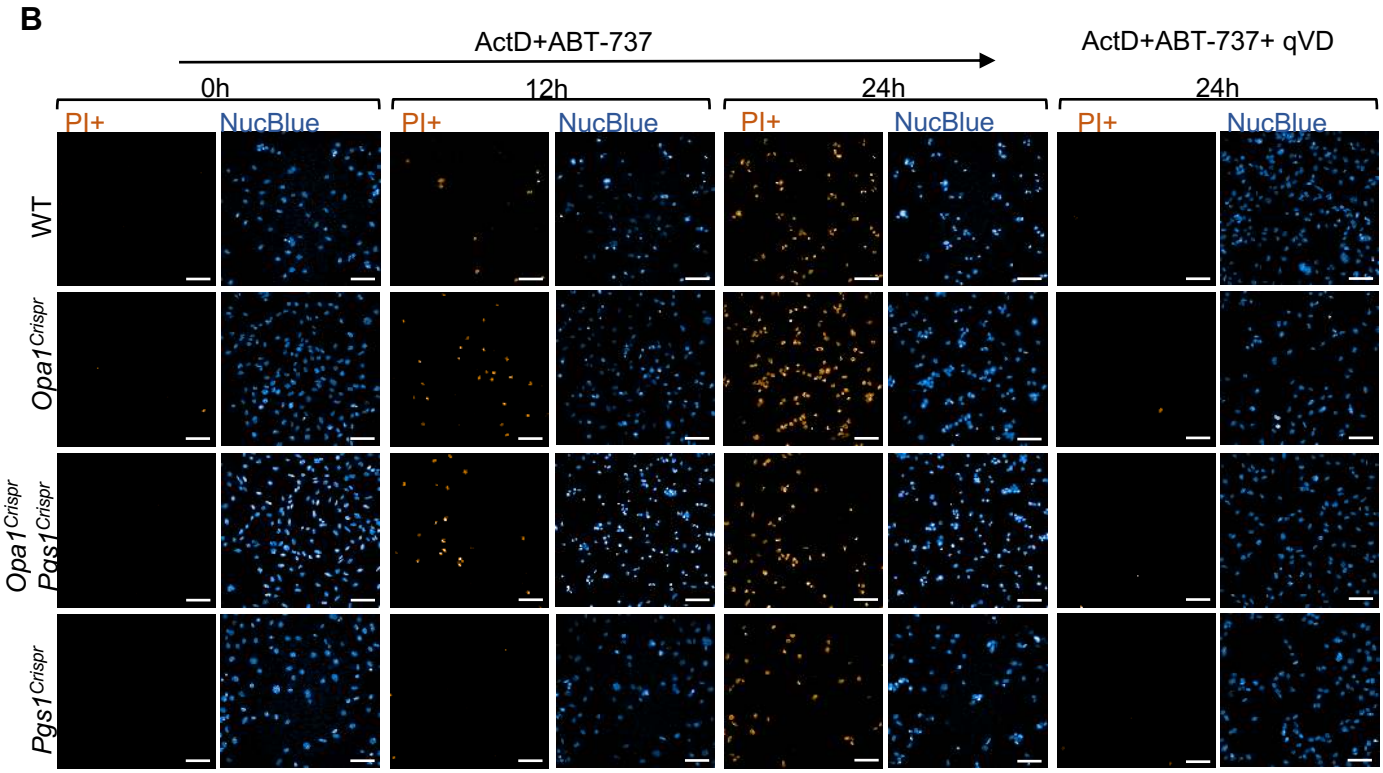
B
ActD+ABT-737
ActD+ABT-737+ qVD
0h
12h
24h
24h
PI+
NucBlue
WT
Opa1Crispr
Opa1CrispPgs1Crispr
Pgs1Crispr

C

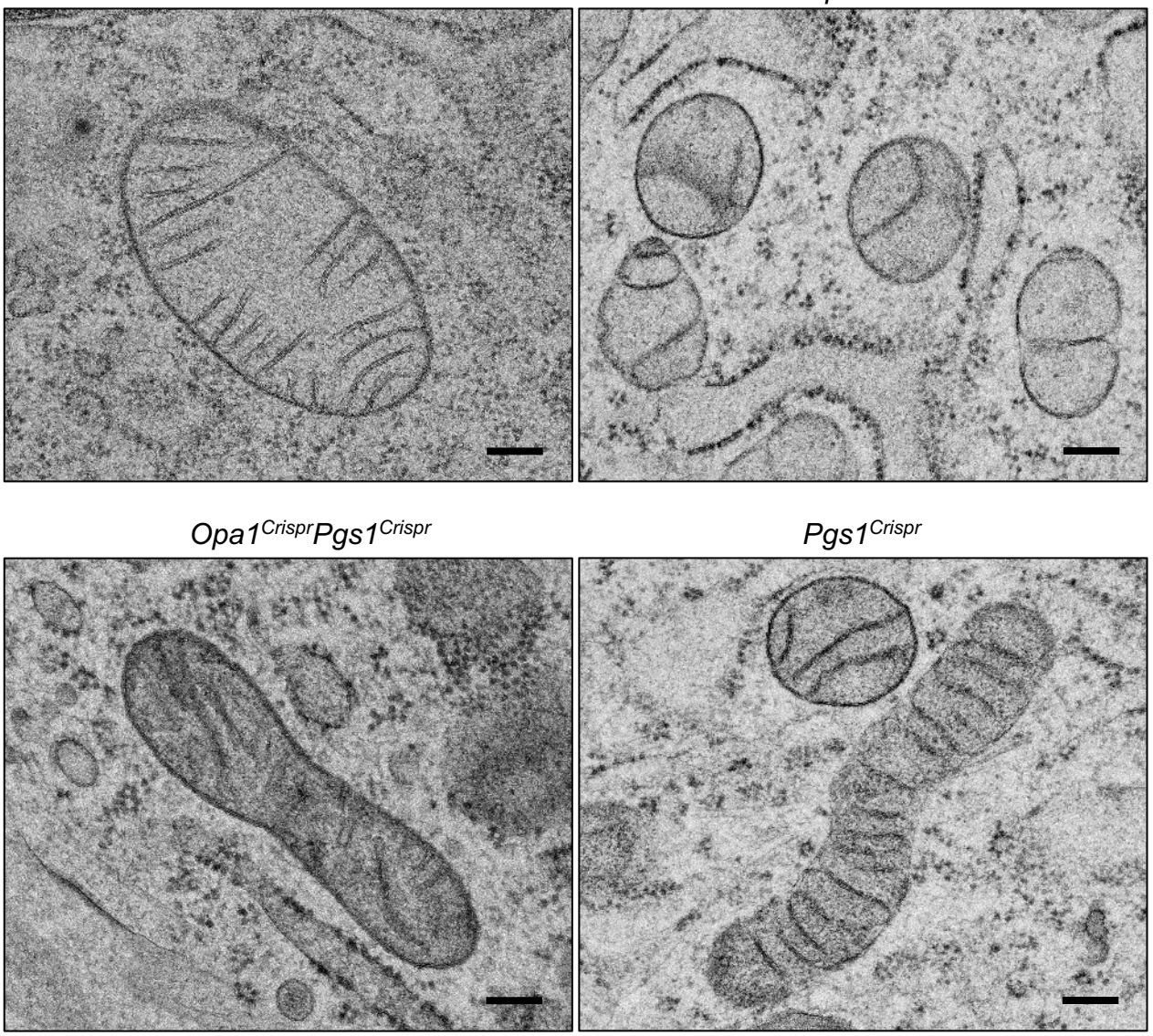
WT
Opa1Crispr
Opa1CrisprPgs1Crispr
Pgs1Crispr

D

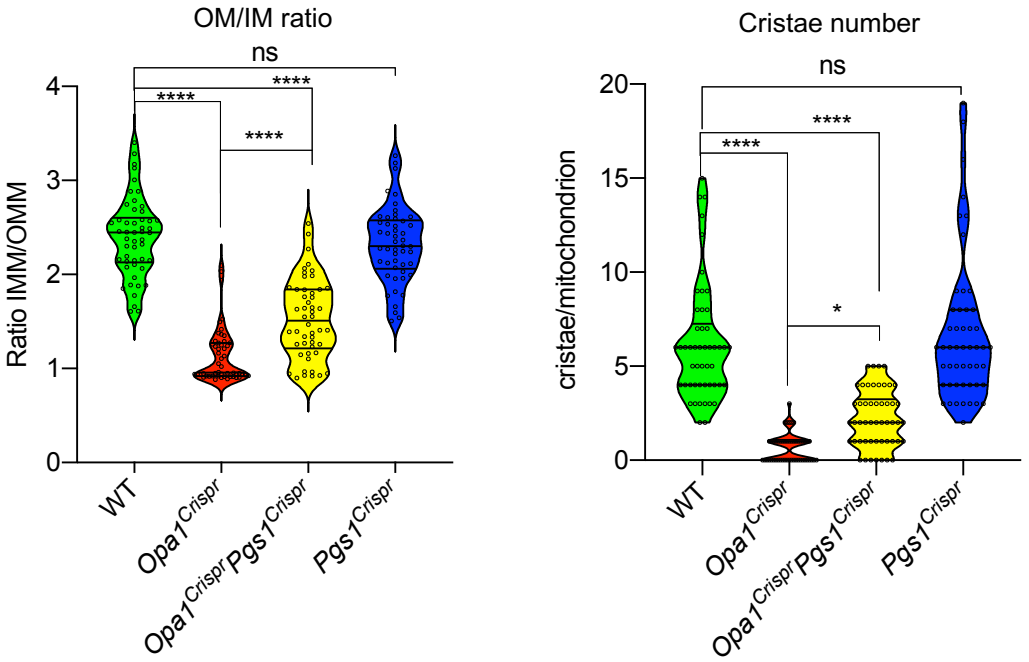
OM/IM ratio
ns
****
****
****
Ratio IMM/OMM
0
1
2
3
4
WT
Opa1Crispr
Opa1CrisprPgs1Crispr
Pgs1Crispr
Cristae number
ns
****
****
*
cristae/mitochondrion
0
5
10
15
20
WT
Opa1Crispr
Opa1CrisprPgs1Crispr
Pgs1Crispr

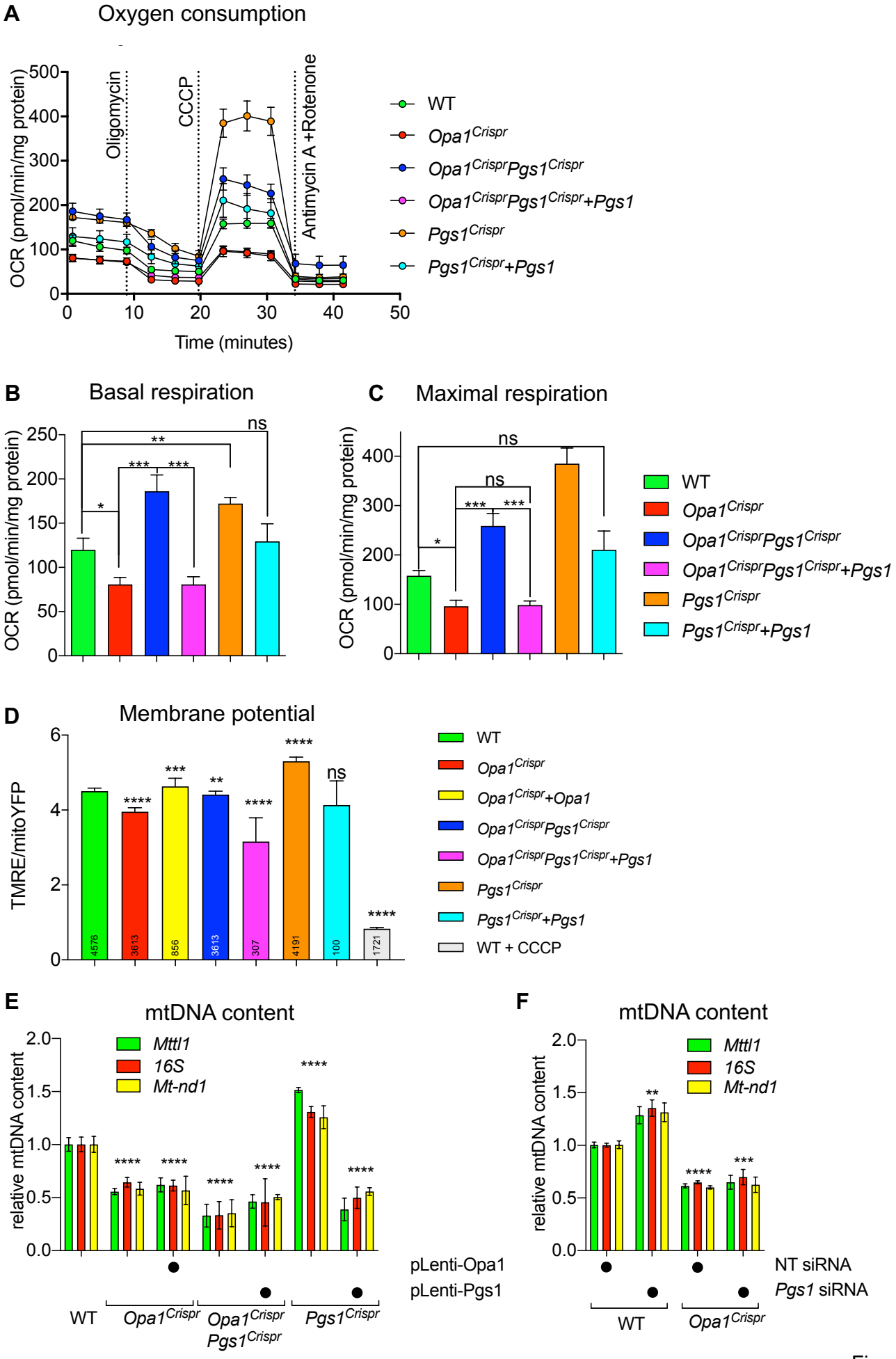
A
Oxygen consumption
OCR (pmol/min/mg protein)
Oligomycin
CCCP
Antimycin A +Rotenone
Time (minutes)
WT
Opa1Crispr
Opa1CrisprPgs1Crispr
Opa1CrisprPgs1Crispr+Pgs1
Pgs1Crispr
Pgs1Crispr+Pgs1
B
Basal respiration
C
Maximal respiration
D
Membrane potential
TMRE/mitoYFP
Opa1Crispr+Opa1
WT + CCCP
E
mtDNA content
relative mtDNA content
Mttl1
16S
Mt-nd1
pLenti-Opa1
pLenti-Pgs1
F
NT siRNA
Pgs1 siRNA

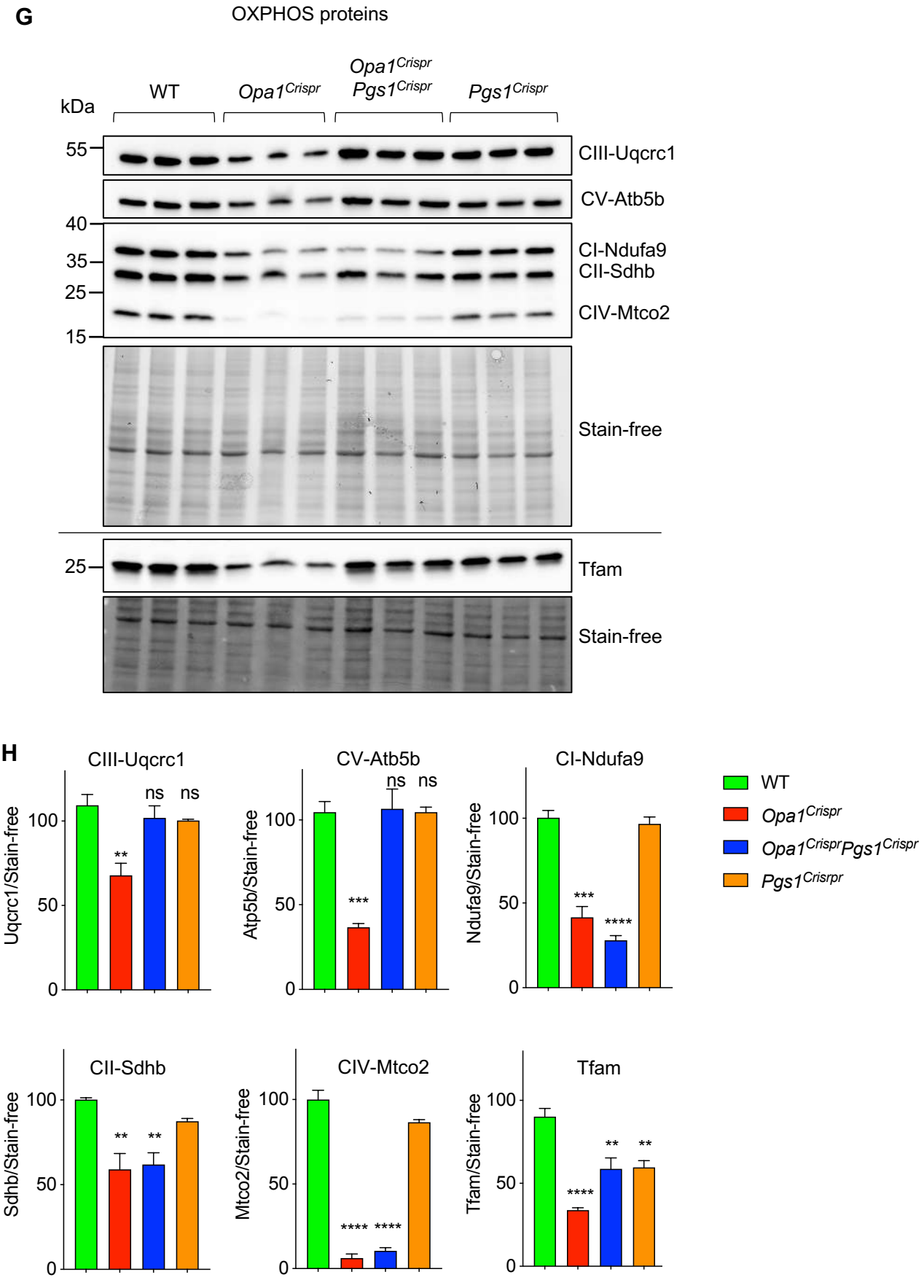
G
OXPHOS proteins
WT
Opa1Crispr
Opa1Crispr Pgs1Crispr
Pgs1Crispr
kDa
55
40
35
25
15
CIII-Uqcrc1
CV-Atb5b
CI-Ndufa9
CII-Sdhb
CIV-Mtco2
Stain-free
25
Tfam
Stain-free
H
CIII-Uqcrc1
Uqcrc1/Stain-free
CV-Atb5b
Atp5b/Stain-free
CI-Ndufa9
Ndufa9/Stain-free
CII-Sdhb
Sdhb/Stain-free
CIV-Mtco2
Mtco2/Stain-free
Tfam
Tfam/Stain-free
ns
**
***
****
WT
Opa1Crispr
Opa1CrisprPgs1Crispr
Pgs1Crisrpr